Scholars' Mine

Summer 2017

Optimal design and freeform extrusion fabrication of functionally gradient smart parts

Amir Ghazanfari

OPTIMAL DESIGN AND FREEFORM EXTRUSION FABRICATION OF

FUNCTIONALLY GRADIENT SMART PARTS

by

AMIR GHAZANFARI

A DISSERTATION

Presented to the Faculty of the Graduate School of the

MISSOURI UNIVERSITY OF SCIENCE AND TECHNOLOGY

In Partial Fulfillment of the Requirements for the Degree

DOCTOR OF PHILOSOPHY

in

MECHANICAL ENGINEERING

2017

Approved by

Ming C. Leu, Advisor
Gregory E. Hilmas
Robert G. Landers
K. Chandrashekhara
Frank Liou

PUBLICATION DISSERTATION OPTION

This dissertation has been prepared using the Publication Option.

Paper I, "A Novel Freeform Extrusion Fabrication Process for Producing Solid Ceramic Components with Uniform Layered Radiation Drying," was published in *Additive Manufacturing* journal and can be found on pages 11-38.

Paper II, "Mechanical Characterization of Parts Produced by Ceramic On-Demand Extrusion Process," was published in *International Journal of Applied Ceramic Technology* and can be found on pages 39-56.

Paper III, "Additive Manufacturing and Mechanical Characterization of High Density Fully Stabilized Zirconia," was published in *Ceramics International* journal and can be found on pages 57-74.

Paper IV, "Adaptive Rastering Algorithm for Freeform Extrusion Fabrication Processes," was published in *Virtual and Physical Prototyping* journal and can be found on pages 75-92.

Paper V, "Optimal Rastering Orientation in Freeform Extrusion Fabrication Processes," was published in proceedings of *Solid Freeform Fabrication Symposium* and can be found on pages 93-107.

Paper VI, "Composition Optimization for Functionally Gradient Parts Considering Manufacturing Constraints," was published in proceedings of *ASME 2014 Manufacturing Science and Engineering Conference* and can be found on pages 108-121.

Paper VII, "A generic methodology for optimal design of three-dimensional functionally graded materials considering additive manufacturing constraints," is intended for submission to *Materials and Design* journal and can be found on pages 122-142.

Paper VIII, "Advanced Ceramic Components with Embedded Sapphire Optical Fiber Sensors for High Temperature Applications," was published in *Materials and Design* journal and can be found on pages 143-163.

ABSTRACT

An extrusion-based additive manufacturing process, called the Ceramic On-Demand Extrusion (CODE) process, for producing three-dimensional ceramic components with near theoretical density was developed. In this process, an aqueous paste of ceramic particles with a very low binder content (<1 vol%) is extruded through a moving nozzle at room temperature. After a layer is deposited, it is surrounded by oil (to a level just below the top surface of most recent layer) to preclude non-uniform evaporation from the sides. Infrared radiation is then used to partially, and uniformly, dry the just-deposited layer so that the yield stress of the paste increases and the part maintains its shape. The same procedure is repeated for every layer until part fabrication is completed. Sample parts made of alumina and fully stabilized zirconia were produced using this process and their mechanical properties including density, strength, Young's modulus, Weibull modulus, toughness, and hardness were examined. Microstructural evaluation was also performed to measure the grain size, and critical flaw sizes were obtained. The results indicate that the proposed method enables fabrication of geometrically complex parts with superior mechanical properties. Furthermore, several methods were developed to increase the productivity of the CODE process and enable manufacturing of functionally graded materials with an optimum distribution of material composition. As an application of the CODE process, advanced ceramic components with embedded sapphire optical fiber sensors were fabricated and properties of parts and sensors were evaluated using standard test methods.

ACKNOWLEDGMENTS

I would like to thank my advisor, Dr. Ming Leu, for providing me with the opportunity to work on this project. I admire his hard work and enthusiasm towards research which inspired me to pursue a career as a researcher. Further, I thank the Department of Energy's Office of Fossil Fuels, Honeywell Inc., Lockheed Martin, and Intelligent Systems Center (ISC) at Missouri S&T for providing financial support at various stages of my Ph.D. study.

I would like to thank Drs. Greg Hilmas and Jeremy Watts for their helpful discussions and constructive suggestions during my graduate study. Thanks to Dr. Robert Landers, Dr. K. Chandrashekhara, and Dr. Frank Liou for helpful suggestions and serving on my committee.

I would like to acknowledge all current and past members of CODE/FEF Research Group, and especially, Wenbin Li, Devin McMillen, Aaron Thornton, and Jie Li for our productive discussions and all the help over the years. I also thank graduate students from UHTC laboratory, and especially, Ryan Grohsmeyer for his help during mechanical characterization experiments.

Finally, I would like to dedicate this work to my parents, Parviz Ghazanfari and Fatemeh Sharifi, and my brother, Mohammad, for their emotional support and unconditional love and sacrifices.

TABLE OF CONTENTS

LIST OF ILLUSTRATIONS

LIST OF TABLES

PAPER VIII

SECTION

1. INTRODUCTION

1.1. FREEFORM EXTRUSION FABRICATION OF ADVANCED CERAMICS

Additive Manufacturing (AM) of advanced ceramics has several advantages over traditional processing techniques including ease of fabricating geometrically complex parts and reduction of manufacturing costs for one-of-a-kind parts or small batches. Several AM techniques have been developed or modified to fabricate three-dimensional ceramic components, including 3D Printing [1], Ink-jet Printing [2], Selective Laser Sintering (SLS) [3], Stereolithography (SLA) [4], Laminated Object Manufacturing (LOM) [5], and extrusion-based techniques. All of these techniques involve adding ceramic materials layer by layer. A comprehensive review on additive manufacturing of ceramic-based materials was recently published by Travitzky et al. [6].

Many efforts to additively manufacture ceramic components resulted in parts with defects (i.e., flaws or large porosity as a result of the AM process). It is well-known that the properties of ceramics are sensitive to porosity, and they would be expected to exhibit poor mechanical properties even at 80% relative density (e.g., [7]). Although these parts may have remarkable geometrical complexity and be suitable for some applications, they are not apt to be used as structural ceramics. In many cases, the mechanical properties of these parts are so poor that they are not even reported in papers and technical reports. According to Zocca et al. [8], AM of monolithic ceramics, enabling the components to match the physical and chemical properties of their conventionally manufactured counterparts, is still a challenge and remains the most important task that needs to be solved to promote AM of ceramics to more than a niche technology.

Extrusion-based methods are among the most popular approaches for freeform fabrication of ceramic components due to the simplicity and low cost of their fabrication system, high density of their fabricated parts, their capability of producing parts with multiple materials [7] and/or as functionally graded materials [8,9], and the low amount of material wasted during processing. Major extrusion-based processes include Extrusion

Freeform Fabrication (EFF), Fused Deposition of Ceramics (FDC), Robocasting (RC), and Freeze-form Extrusion Fabrication (FEF).

EFF [10] was the first technique to utilize extrusion of ceramic slurries (organic-based) to produce three-dimensional components. Slurries of alumina in liquid acrylic monomers were prepared and deposited onto a heated platen to retain their shape. The process was further improved and more complex geometries with other materials such as silicon nitride were fabricated [11]. EFF is also the first extrusion-based process to produce ceramic-based functionally graded materials such as ceramic oxides graded to Inconel or stainless steel [8].

Danforth introduced the concept of FDC [12]. They used a commercial Fused Deposition Modeling (FDM) system from Stratasys Inc. (Eden Prairie, MN, USA) to extrude ceramic-loaded thermoplastic filaments. The filament was liquefied, extruded, and re-solidified to retain its shape. Since then, they have significantly improved their process and have been able to produce high quality parts made of different materials for various applications, especially sensors and actuators [13–17].

RC [18,19] is a renowned freeform extrusion fabrication process of ceramics. The main advantage of RC over EFF and FDC is the use of a lower amount of binder in the feedstock (<10 wt% vs. >30 wt%) which makes pre-processing and post-processing less time-consuming. In this process, typically an aqueous suspension from ceramic materials (e.g. alumina, silica, lead zirconate titanate, hydroxyapatite, silicon carbide, and silicon nitride) is prepared and extruded on to a hot plate to dry and maintain its shape. RC can produce grid or thin-wall structures for various applications, especially bio-fabrication [20–24].

In the FEF process [25], a high solids loading (> 50 vol%) aqueous paste containing 1-4 vol% organic additives is extruded in a freezing environment to solidify the paste after its deposition. Freeze drying is then used to remove the water content before sintering. This process is also capable of producing complex and functionally graded parts made of different materials such as alumina, zirconium diboride, boron carbide, zirconium carbide, and bio-active glasses [26–29]. Several advanced control algorithms were also implemented to enhance the performance of extrusion-on-demand and consistency in paste flowrate [30–33].

While the latter additive manufacturing processes have their respective advantages, they also have limitations. The binder removal procedures for EFF and FDC is difficult and time-consuming, and sometimes causes severe warpage or other defects. It might require multiple cycles with different atmospheres. For FDC, the feedstock preparation is also burdensome and requires several steps. The filament must also maintain a high dimensional tolerance (<2% variations in diameter) to ensure consistent flowrates [17]. Although parts of multiple materials could be produced, FDC is not capable of mixing them and fabricating functionally graded parts. It is difficult for RC to build large solid parts due to non-uniform drying which causes warpage and cracks in the parts. Furthermore, due to inconsistency in extrudate flowrate and the presence of air bubbles in the suspension, the products are not fully dense and their mechanical strength does not match that of parts produced by EFF and FDC. For FEF, there is also the added challenge of ice crystal formation during the freezing process, and weak layer-to-layer bonding, which further reduce the relative density and mechanical properties after binder removal and sintering. Finally, all these extrusion-based processes suffer from nozzle clogging due to ceramic powder agglomerates and binder agglomerates in the feedstock, and freezing or drying of paste inside the nozzle.

1.2. PRODUCTIVITY OF FREEFORM EXTRUSION FABRICATION PROCESSES

One of the main challenges facing additive manufacturing processes is the geometrical errors. There are several sources for these errors including representation of CAD files in STL format and approximating complex shapes by lines of deposited material. The latter source is commonly referred to as the staircase effect in the AM literature. If this effect is in the Z direction, between layers, it is called 'vertical' staircase effect, and if it is in the XY plane, between lines, it is called 'horizontal' staircase effect. An obvious method to decrease this type of error in both directions is using finer lines. However, this will result in prolonged fabrication time. Approaches to reduce the horizontal staircase effect include printing outer contours, which follow the boundary of every layer, and machining the part after fabrication. These methods might be suitable for polymeric and metallic materials. However, for ceramics the former method may result in

lower mechanical strength and the latter method is difficult and expensive. The reason that printing outer contours may considerably reduce the strength of the part is that it may introduce gaps between the outer contours and deposited lines of material in the inner regions and, since ceramics are sensitive to voids and flaws, the part loses its strength.

In many freeform extrusion fabrication machines, the bottleneck in achieving higher productivity is the maximum attainable travel speed [34,35]. When the travel speed is set to its maximum value, productivity could be further increased by increasing the feed rate. However, at a constant travel speed, higher material feed rates result in larger lines and, thus, larger staircase errors, creating a compromise between productivity and accuracy. Another approach is setting the travel speed at its maximum value and adaptively changing the feed rate depending on changes in geometry of the part. In other words, when there is no abrupt change in the geometry, higher feed rates are used to decrease the fabrication time; however, lower feed rates are used to build steep slopes and delicate features with fine lines. This concept has been employed in 'adaptive slicing' methods to reduce the 'vertical' staircase effect. A brief review of adaptive slicing methods is provided in the following paragraphs.

Dolenc and Makela [36] introduced the concept of adaptive slicing. They used cusp height to calculate the part's dimensional error for each layer thickness. The user specifies a maximum allowable value for the cusp height, and the surface normal of the preceding intersection plane in the CAD file is compared with that value to determine the optimal layer thickness. Although many researchers still use the cusp height criterion (e.g. [37]), other methods have been proposed to calculate the error. Zhao & Laperriere [38] proposed an area deviation error criterion to obtain the appropriate layer thickness. Kumar & Choudhury [39] extended the error criterion to three-dimensional space and introduced a volume deviation criterion for direct adaptive slicing. Singhal et al. [40] used surface roughness to determine the optimal value for layer thickness between user-defined minimum and maximum values. Hayasi & Asiabanpour [41] projected all pairs of corresponding slices at the top and bottom of a layer onto the XY, XZ and YZ horizontal surfaces to detect any possible part geometry distortion. They also employed a bottom-up slicing approach where they start cutting at the minimum available thickness

to avoid any large geometry deviation errors caused by sharply concave or convex corners.

Chen & Feng [42] considered the deviation between the final polished part and the CAD file boundary, and optimized the thickness as well as the position of each layer to minimize the number of layers for a given tolerance. Recently, the concept of adaptive slicing has been applied to additive manufacturing of Functionally Gradient Materials (FGM). For example, Wang et al. [43] proposed a data format for modeling FGM objects and presented an adaptive slicing algorithm based on the finite element concept for FGM, which slices an FGM object into layers and then stores the data according to the proposed data format.

1.3. OPTIMAL DESIGN OF FUNCTIONALLY GRADED MATERIALS

Functionally Gradient Materials (FGMs) are a type of composite materials made of two or more constituent phases with a continuously variable composition. These materials are gaining more applications in the automotive and other industries because of their enhanced properties which include higher toughness, resistance to thermal loads, improved residual stress distribution and most importantly a combination of these favorable properties. Their main application is in situations where the designer needs different material properties at different spots in a single part; especially if continuous variations are desirable. For example, consider a lathe cutting tool at the tip of which high resistivity to elevated temperatures is required whereas at the shank high mechanical strength is desirable. A viable solution is to gradually change the material composition from ceramic at the tip to metal at the shank. Numerous papers deal with various aspects of FGM and the reader is referred to a review paper by Birman and Byrd [44] for a rather recent and comprehensive review. Because of diverse applications of these materials, being able to design and fabricate parts made of FGMs with desirable and optimum properties is of prime importance. There are numerous papers in the literature about approaches to homogenization of FGMs, their response to mechanical and thermal loads, testing methods and manufacturing aspects; however, insufficient research has been carried out regarding the optimization of composition of different constituent phases

throughout the part. In what follows, a thorough review of the literature regarding optimization of material composition is provided.

Wang and Wang [45] applied a complex variational method to minimize strain energy in two-dimensional rectangular beams by assigning various materials to different locations. Although several materials have been used, they are not mixed together but rather form separate regions. Goupee and Vel [46] employed a real-coded genetic algorithm to find the two-dimensional optimum material composition for functionally graded plates under thermal loads. Two example problems were solved: In the first problem (a simply supported three-layered Ni-Al_2O_3 plate), they minimized the peak residual stress when the functionally graded component was cooled from a high fabrication temperature. In the second problem (with Al-ZrO_2 composition), the goal was to minimize the mass of the beam with constraints on the peak effective stress and maximum temperature experienced by the metal. Lin et al. [47] considered teeth made of hydroxyapatite/collagen and titanium under applied chewing forces and maximized the densities of cortical and cancellous bones while minimizing the vertical displacement. The material gradient was only in the vertical direction and governed by a power law. Na and Kim [48] assumed a simple power law for material distribution which varied only in the z direction. The problem was about a three-dimensional panel composed of ZrO_2 and Ti–6Al–4V, which underwent a sinusoidal mechanical load distributed over the top surface of the model and a temperature variation was also applied on the same side. The objectives were to minimize the maximum stress while maximizing the critical temperature which would result in thermo-mechanical buckling. Xu et al. [49] modeled a cylinder with two materials and used the evolutionary structural optimization algorithm to optimize the material distribution (in the radial direction only) in order to reach a uniform stress distribution. Chiba and Sugano [50] optimized the material composition of an infinite functionally graded plate made of Ti and ZrO_2 in only one direction using a genetic algorithm. The plate was exposed to different temperatures at top and bottom and the goal was to minimize the stress. Kou et al. [51] optimized one- and two-dimensional material distribution of parts exposed to temperature variations. The objective of optimization was to simultaneously minimize the Von Mises stress and the mass of a plate made of zirconia (ZrO_2) and a titanium alloy (Ti-6Al-4V). Ghazanfari and Leu [52]

used a sequential approximate optimization method to maximize the stiffness of beams with two-dimensional material distribution. Zhang et al. [53] proposed a framework to achieve an optimal material composition for different objective functions using a Monte Carlo-based and a gradient descend-based optimizer. They were also able to convert the continuous material distribution to discrete distribution for viable manufacturing.

Most previous researchers only considered thermal stresses resulting from variations in temperature, and there is a paucity of work considering mechanical loads and resultant strains. They were also typically not able to handle realistic material models and used a simple rule of mixture to estimate the properties of FGM. Furthermore, no paper was found in the literature addressing optimization of material composition distribution in three dimensions. Furthermore, most previous methods either assumed a one-dimensional material gradient or used an analytical equation with a few constants to represent the distribution of material composition. Additionally, manufacturing constraints were not taken into account in previous research efforts.

1.4. SMART LINING BLOCKS IN ADVANCED ENERGY SYSTEMS

Embedded sensors have been widely used in structural health monitoring and proven effective in civil and structural engineering [54,55]. However, there are currently no viable techniques for in-situ monitoring of the health status of the critical components in energy production systems. In addition, the existing techniques for process monitoring are inadequate to operate reliably in the extremely harsh environments over a long time [56]. The sensing capabilities can be incorporated in the design phase of various energy systems by embedding sensors into the critical components, enabling a new paradigm in harsh-environment sensing. The embedded sensors not only provide real-time information on the health status of the component, but also reduce the complexity in sensor installation and increase the robustness of the sensors for reliable measurements of various parameters that are important for system control and optimization.

Embedded sensors are conventionally attached to or mounted on the component after the structure is fabricated. Several embedment techniques for strain sensors have been proposed in the literature [57–63]. However, these techniques could result in an unsecured sensor attachment, offsets between the sensor readings and the actual status of

the structure, potential performance degradation of the host materials or structures, and relative slip at the interface of the matrix and sensor encapsulation [64–68]. For strain measurements, in most cases, the strain sensitivity of an embedded sensor is significantly different from that of the bare sensor [55]. In harsh environments, the sensors are either surface mounted far from critical locations to avoid interference with the operation of the structures, or destructively inserted into the critical locations through appropriate channels in the structures, making it difficult to provide measurements with a high spatial and temporal resolution [69]. Additive manufacturing (AM) is potentially a promising method that could be employed to embed the sensors into the host structure during component fabrication. This allows secured sensor placement, enhances the survivability, improves the measurement accuracy and reliability, and preserves the structural integrity of the parts.

AM has been recently exploited to embed fibers, sensors or other components in parts to enhance the properties of parts (e.g., strengthen them) or produce smart components. Most of the research in this area is based on ultrasonic consolidation (UC) or ultrasonic additive manufacturing (UAM) process. Janaki et al. [70] used this process to embed SiC fibers and stainless wire meshes in an Al 3003 matrix and produced fiber-reinforced metal matrix composites. Li et al. [71] embedded fiber Bragg gratings (FBG) in metal foil using UC processes and investigated the embedding process, cross-sections of welded samples, the form change and wavelength shift of the Bragg peak during the processes, and the sensing characteristics of the embedded FBGs. Maier et al. [72] embedded optical fiber sensors incorporating FBGs in a polymeric component made by the selective laser sintering process. Dapino [73] also used UC to fabricate Galfenol beams for adaptive vibration absorbers, NiTi/Al composites for zero coefficient of thermal expansion applications, and structures with embedded cooling channels. Monaghan et al. [74] exploited UC to integrate optical fibers equipped with metallic coatings into solid aluminum matrices. They also characterized the inter-laminar and fiber/matrix interfaces and examined their bonding strength. In another paper [75], they embedded three dielectric materials into aluminum metal-matrices produced by the UC process and investigated the effect of the dielectric material hardness on the final metal matrix mechanical strength. Kousiatza and Karalekas [76] embedded FGBs in

thermoplastic parts during their fabrication process in a fused deposition modeling system for in-situ and real-time monitoring of strain fields and temperature profiles as the parts were being built.

Because of their high melting point and excellent resistance to oxidation, chemical attack and erosion, advanced ceramics are the best candidates for host materials in harsh and corrosive environments of energy production systems. Several AM techniques have been developed or modified to fabricate three-dimensional ceramic components, including 3D printing, ink-jet printing, selective laser sintering, stereolithography, laminated object manufacturing, and extrusion-based techniques (mainly fused deposition of ceramics, robocasting, and freeze-form extrusion fabrication). However, these processes are either incapable of producing a mechanically strong part, or embedding a sensor in the part during fabrication is infeasible. Thus, development of a process for manufacturing high-strength advanced ceramics with embedded sensors could be very beneficial to this field.

Due to their small size, light weight, immunity to electromagnetic interference, multiplexing and distributed sensing capability, resistance to chemical corrosion, and remote operation capability, optical fiber sensors are by far the best candidates to be embedded in parts. FBG is the most successful fiber optic sensor and has shown great advantages for integrating with AM techniques. FBGs consist of periodic refractive index variations written by an intense ultraviolet (UV) laser. These periodic variations, also called Bragg grating, have a certain period that can be encoded by an optical resonant wavelength, and by tracking the resonant wavelength shift, one can detect the strain applied on the FBG, making it a good candidate for strain measurement. However, it has been found that the UV laser induced material variations could be easily erased if the ambient temperature is higher than 450 °C, making it inapplicable for strain sensing under high temperature (up to 1000 °C) [78]. In some particular applications, such as high temperature material characterization, coal gasifier health monitoring, turbine crack detection, or structural health monitoring of the leading edge of a wing, strain sensors that can survive in extreme temperatures are needed. Most of the optical fiber sensors are made of silica glass and their long-term reliability above 1000 °C has been a concern due to the degradation of optical properties and mechanical strength. To further increase the

operating temperatures, researchers have turned to sapphire fibers which have a melting point of 2050 °C, low optical loss in a large spectrum window, superior mechanical strength, and excellent resistance to chemical corrosion [79]. Recently, constructing a sensor on an optical sapphire fiber for use in temperatures up to 1400 °C has been successfully demonstrated by Huang et al. [80]. As a result, technologies for the embedment of sapphire fiber sensors for high temperature applications are highly needed.

1.5. ORGANIZATION OF DISSERTATION

The first paper introduces a novel freeform extrusion fabrication process, called Ceramic On-Demand Extrusion (CODE), for producing dense ceramic components. All the pre-processing, processing, and post-processing steps are explained and sample parts are provided. The second and third papers focus on properties of parts produced by CODE. In the second paper, alumina parts were produced and examined, and in the third paper, fully stabilized zirconia paste was studied.

The fourth paper focuses on increasing the productivity without sacrificing the geometrical accuracy. A technique applicable to all freeform extrusion fabrication processes is proposed in this paper to adaptively change the line width while printing a part. In the fifth paper, the rastering orientation for each layer of a part was optimized using the Particle Swarm Optimization method in order to minimize the geometrical errors.

The sixth and seventh papers propose two different strategies for optimal design of Functionally Graded Materials. The objective of both strategies is to optimize the distribution of material composition in a functionally graded part.

The eighth paper focuses on an application of the CODE process in advanced energy systems. Sapphire optical fiber sensors were embedded in components made of advanced ceramics during their fabrication process in an attempt to produce smart lining blocks for gasification chambers.

The last section of this dissertation contains conclusions of these studies and provides suggestions for future work in this area.

PAPER

I. A NOVEL FREEFORM EXTRUSION FABRICATION PROCESS FOR PRODUCING SOLID CERAMIC COMPONENTS WITH UNIFORM LAYERED RADIATION DRYING[1]

ABSTRACT

An extrusion-based additive manufacturing process, called the Ceramic On-Demand Extrusion (CODE) process, for producing three-dimensional ceramic components with near theoretical density is introduced in this paper. In this process, an aqueous paste of ceramic particles with a very low binder content (<1 vol%) is extruded through a moving nozzle at room temperature. After a layer is deposited, it is surrounded by oil (to a level just below the top surface of most recent layer) to preclude non-uniform evaporation from the sides. Infrared radiation is then used to partially, and uniformly, dry the just-deposited layer so that the yield stress of the paste increases and the part maintains its shape. The same procedure is repeated for every layer until part fabrication is completed. Several sample parts for various applications were produced using this process and their properties were obtained. The results indicate that the proposed method enables fabrication of large, dense ceramic parts with complex geometries.

1. INTRODUCTION

Several additive manufacturing techniques have been developed or modified to fabricate three-dimensional ceramic components, including 3D Printing [1], Ink-jet Printing [2], Selective Laser Sintering (SLS) [3], Stereolithography (SLA) [4], Laminated Object Manufacturing (LOM) [5], and extrusion-based techniques. All of these techniques involve adding ceramic materials layer by layer. A comprehensive review on additive manufacturing of ceramic-based materials was recently published by Travitzky et al. [6].

---

[1] This paper was published in *Additive Manufacturing* journal, vol. 15, pp. 102-112, 2017.

Extrusion-based methods are among the most popular approaches for freeform fabrication of ceramic components due to the simplicity and low cost of their fabrication system, high density of their fabricated parts, their capability of producing parts with multiple materials [7] and/or as functionally graded materials [8,9], and the low amount of material wasted during processing. Major extrusion-based processes include Extrusion Freeform Fabrication (EFF), Fused Deposition of Ceramics (FDC), Robocasting (RC), and Freeze-form Extrusion Fabrication (FEF).

EFF [10] was the first technique to utilize extrusion of ceramic slurries (organic-based) to produce three-dimensional components. Slurries of alumina in liquid acrylic monomers were prepared and deposited onto a heated platen to retain their shape. The process was further improved and more complex geometries with other materials such as silicon nitride were fabricated [11]. EFF is also the first extrusion-based process to produce ceramic-based functionally graded materials such as ceramic oxides graded to Inconel or stainless steel [8].

Danforth introduced the concept of FDC [12]. They used a commercial Fused Deposition Modeling (FDM) system from Stratasys Inc. (Eden Prairie, MN, USA) to extrude ceramic-loaded thermoplastic filaments. The filament was liquefied, extruded, and re-solidified to retain its shape. Since then, they have significantly improved their process and have been able to produce high quality parts made of different materials for various applications, especially sensors and actuators [13–17].

RC [18,19] is a renowned freeform extrusion fabrication process of ceramics. The main advantage of RC over EFF and FDC is the use of a lower amount of binder in the feedstock (<10 wt% vs. >30 wt%) which facilitates pre-processing and post-processing. In this process, typically an aqueous suspension from ceramic materials (e.g. alumina, silica, lead zirconate titanate, hydroxyapatite, silicon carbide, and silicon nitride) is prepared and extruded on to a hot plate to dry and maintain its shape. RC can produce grid or thin-wall structures for various applications, especially bio-fabrication [20–24].

In the FEF process [25], a high solids loading (> 50 vol%) aqueous paste containing 1-4 vol% organic additives is extruded in a freezing environment to solidify the paste after its deposition. Freeze drying is then used to remove the water content before sintering. This process is also capable of producing complex and functionally

graded parts made of different materials such as alumina, zirconium diboride, boron carbide, zirconium carbide, and bio-active glasses [26–29]. Several advanced control algorithms were also implemented to enhance the performance of extrusion-on-demand and consistency in paste flowrate [30–33].

While the latter additive manufacturing processes have their respective advantages, they also have limitations. The binder removal procedures for EFF and FDC is difficult and time-consuming, and sometimes causes severe warpage or other defects. It might require multiple cycles with different atmospheres. For FDC, the feedstock preparation is also burdensome and requires several steps. The filament must also maintain a very high dimensional tolerance (<2% variations in diameter) to ensure consistent flowrates [17]. Although parts of multiple materials could be produced, FDC is not capable of mixing them and fabricating functionally graded parts. It is difficult for RC to build large solid parts due to non-uniform drying which causes warpage and cracks in the parts. Furthermore, due to inconsistency in extrudate flowrate and presence of air bubbles in the suspension, the products are not fully dense and their mechanical strength does not match that of parts produced by EFF and FDC. The latter challenges add to ice crystal formation during the freezing process, and weak layer-to-layer bonding in FEF to further reduce the relative density and mechanical properties after binder removal and sintering. Finally, all these extrusion-based processes suffer from nozzle clogging due to ceramic powder agglomerates and binder agglomerates in the feedstock, and freezing or drying of paste inside the nozzle.

In an attempt to overcome the above limitations, the Ceramic On-Demand Extrusion (CODE) process is proposed in this paper. The feedstock of this process is an aqueous paste prepared in a similar fashion as in FEF. The paste is then extruded at room temperature through a progressive cavity pump based extruder to guarantee a consistent flowrate. The solidification of each layer is achieved via partial drying using an infrared lamp, with a liquid oil surrounding the part. This precludes non-uniform evaporation from the sides of the part during the radiation drying and enables fabrication of large solid parts with complex geometries. Moreover, the proposed method reduces the risk of part warpage and crack formation during the binder removal step. Another advantage of this process is that it produces three-dimensional green bodies that can be machined to

increase the surface smoothness and dimensional accuracy of the printed parts prior to sintering. Several sample parts are fabricated and their properties are studied.

2. CERAMIC ON-DEMAND EXTRUSION (CODE) PROCESS

2.1. PROCESS OVERVIEW

In the CODE process proposed in this paper, viscous suspensions (pastes) of ceramic particles are extruded at controlled flowrates through a circular nozzle. The nozzle is attached to a motion system which is capable of moving in X, Y and Z directions through G & M code commands provided by an indigenously developed tool-path planning software. The extrudate is deposited on a substrate located in a tank designed to hold a fluid medium. Once the deposition of each layer is completed, a liquid feeding subsystem pumps oil into the tank surrounding the layer to preclude undesirable water evaporation from the sides of the deposited layers. The level of the liquid is controlled so that it is maintained at a level that is just below the top surface of the part being fabricated. Infrared radiation is then used to uniformly dry the deposited layer so that the part being fabricated can maintain its shape when the next layers are being deposited on top of it. The part is fabricated in a layer-by-layer fashion by repeating the layered deposition followed by radiation drying with a liquid surrounding the already deposited layers during the part fabrication process. A schematic of the process is shown in Figure 1. Once the fabrication process is completed, the remaining water content in the fabricated part is removed further by bulk drying to obtain green parts. The post-processing includes removing the binder content and sintering the part at elevated temperatures.
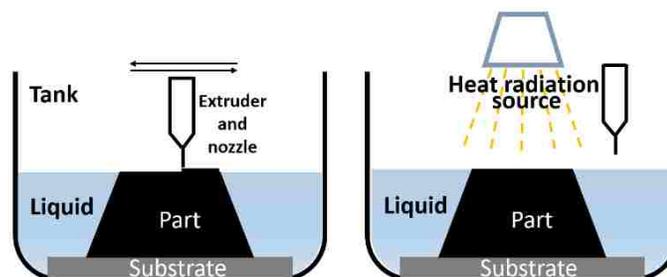
Figure 1. Schematic of the Ceramic On-Demand Extrusion process.

For fabricating components that have external/internal features such as overhangs, conformal cooling channels, etc. and cannot be fabricated without the use of support, an inorganic sacrificial material ($CaCO_3$) is used to build a support structure. The sacrificial material decomposes during sintering and then dissolves in water or acid afterwards [34].

2.2. TOOL-PATH PLANNING SOFTWARE

Because of limitations of commercial tool-path planning software, a program was developed using Matlab programming language. It is capable of reading the geometry of the part in Stereolithography format (STL), preparing and illustrating the tool-path for each layer, and generating a G & M code for the fabrication machine. The program takes the user inputs (layer thickness, raster spacing, dwell time for the gantry system before each starting point, dwell time for the gantry system after printing each layer, early stop distance, extrusion speed, table speed, distance traveled by the gantry system in Z-direction after each stop, etc.) along with the STL file, slices it by calculating its intersections with constant-Z planes, designs tool-path for each layer and generates the required G & M code for the machine to fabricate the part. The program consists of the following subroutines:

Reading and slicing subroutine: a subroutine was developed in Matlab capable of reading an STL file and cutting it into a desired number of slices (layers) with adjustable accuracy. To obtain the slices for each value of Z-coordinate, the subroutine first checks whether there is an intersection between the Z-plane and each triangle in the STL file. If there is an intersection, it finds the two sides that intersect with the plane. Then, it employs analytical geometry equations to find the intersection point of each side with the plane. Next, it connects the two points to form a segment and continues this procedure to find all segments and determine layer boundaries.

Rastering subroutine: to print each layer, the gantry system should be able to follow a suitable path and fill in boundaries of each layer. A subroutine was developed in Matlab that is capable of identifying boundaries of each slice (produced by the previous subroutine) and generating a tool-path for the gantry system to follow. The rasters could be either in X or Y direction. Assuming rasters in X direction are requested by the user, the subroutine first checks whether there is an intersection between a constant-Y line and

each segment in the current layer. If there is an intersection, it employs analytical geometry equations to find the intersection and stores the values in the so-called "t-matrix". Next, it orders "t" so that printing starts at the bottom left of the layer and the first line of material is printed from left to right; then, for the case of the presence of several lines in the next Y-level, the left-most one is chosen and printed from right to left. This procedure is continued until the top-most line of the layer is printed (see Figure 2 (a)). Then, the same procedure is repeated for the remaining rasters until all rasters are printed (Figure 2 (b) and (c)). This subroutine is also capable of adaptively changing the line width to increase the dimensional accuracy and/or the productivity as proposed in [35].
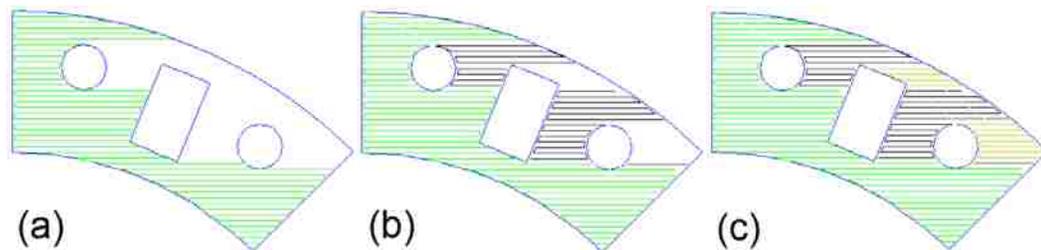
Figure 2. Sequence of printing rasters.

G & M code generating subroutine: the output of the previous subroutine is the path that the gantry system needs to follow and command signals to other subsystems of the fabrication machine. Another subroutine was developed in Matlab capable of producing a text file that contains G & M codes (i.e. tool-path, starts and stops, dwell times, table speed, etc.).

2.3. PASTE PREPARATION

A nominally 60 vol% solids loading alumina paste was prepared using a commercially available alumina powder (A-16SG, Almatis Inc., Leetsdale, PA, USA) in all of the experiments in this study. Other materials including zirconia, silica, boron carbide, 13-93 bioactive glass, zirconium carbide, zirconium diboride, etc. could be potentially used in CODE and are currently under investigation.

The paste was composed of alumina powder, deionized water, ammonium polymethacrylate (DARVAN® C-N, Vanderbilt Minerals, Norwalk, CT, USA), and

methylcellulose (Methocel J5M S, Dow Chemical Company, Midland, MI, USA). For parts which were intended to be freeze dried (as will be discussed in section 2.6.1), 20 wt% glycerol was used as suggested by Sofie and Dogan [36] to prevent the growth of large ice crystals and freezing defects associated with water crystallization. The alumina powder was dispersed in water using 0.94 g Darvan C per 100 g of powder, and then ball-milled for ~15 hours to break up agglomerates and to produce a uniform mixture. Methylcellulose (<1 vol%) was dissolved in water and was used as a binder to increase paste viscosity and to assist in forming a stronger green body after drying. A vacuum mixer (Model F, Whip Mix, Louisville, KY, USA) was employed for 12 minutes to mix the paste homogeneously without introducing air bubbles. Finally, a vibratory table (Syntron Material Handling, Saltillo, MS, USA) was used to remove the remaining air bubbles.

2.4. DRYING BEHAVIOR OF PASTE FILMS

Since the CODE process involves layer-wise partial drying of ceramic paste, a set of experiments was designed and carried out to study the drying behavior of layers during the process. For a given layer thickness and paste properties, the evaporation rate and drying time should be adjusted. If the evaporation rate is too high, cracks may form on the layer surface or the bonding between two successive layers might become weak. On the other hand, if the evaporation rate is too low, the increase in the yield stress of the paste might not be sufficient to maintain the shape of the part or the required drying time might have to be increased too much, which in turn results in unacceptably long fabrication times. A similar argument holds for the drying time. If the drying time is too high, crack formation or weak layer boning may be observed, and if it is too low, the part cannot maintain its shape and deforms. Accordingly, the highest evaporation rate that does not result in crack formation, and the shortest drying time that does not result in part deformation, are desirable in the CODE process.

Crack formation in a layer during drying is the result of stresses caused by pressure gradients in the liquid phase as well as biaxial tension exerted by the substrate. When a portion of the liquid phase in the paste evaporates from the surface, the liquid "stretches" (driven mainly by capillary forces) to cover the dry region. This produces

tension in the liquid, which varies in the thickness direction if the evaporation rate is fast relative to the transport rate of the liquid. This pressure gradient may cause warping and/or cracking if the part body is not stiff and/or strong enough. Furthermore, in the first phase of drying (constant rate period), there is a reduction in the volume of the paste equal to the amount of water evaporated. However, during the drying of a layer on a substrate, the paste cannot shrink at the substrate-paste interface due to adhesion between the two layers. This causes biaxial tension in the paste which increases in the thickness direction. A comprehensive discussion of the drying phenomenon is provided in [37].

The total stress depends on layer thickness, surface tension, evaporation rate, viscosity, permeability, solids loading, etc. Whether or not this stress results in cracks depends on the fracture toughness, Young's modulus and Poisson's ratio of the paste, whose values change during drying. Lange [38] used Griffith's criterion to calculate the critical thickness of a drying film above which the crack formation initiates. Based on his calculations, the critical thickness is

$$h_c = \frac{G_c E^*}{Z \sigma^2} \tag{1}$$

where G_c is the critical stain energy release rate (a measure of fracture toughness), $E^* = E/(1-v)$, where E is the Young's modulus and v is the Poisson's ratio, σ is the stress and Z is a shape factor. Thus, to avoid cracking, one can either improve the strength of the paste (e.g. by adding more binder) or reduce the stresses (e.g. by adding surfactants to reduce surface tension or slow drying process of the paste).

Many researchers have studied the drying behavior of ceramic suspension films and examined the effect of various parameters on crack formation. Carreras et al. [39] investigated the effects of solution chemistry, binder and binder crosslinking on the critical cracking thickness of films obtained by drying aqueous alumina suspensions. Their results indicate that the critical cracking thickness significantly increases by crosslinking poly (vinyl alcohol) used as binder. Holmes et al. [40] used a laser speckle interferometry and experimentally studied the onset of cracking during drying of alumina suspensions cast onto a substrate to better understand this phenomenon. Contrary to other investigations, they postulated that the driving force for cracking actually arises from a misfit strain that occurs when the repulsive layers between the particles collapse

completely and after the particles have adhered to the substrate. Chiu et al. [41] examined the effect of processing variables on cracking behavior of binder-free granular ceramic films. These variables included particle size, liquid surface tension, evaporation rate, dispersion stability, and sedimentation time. They also examined various types of substrates including glass, Teflon and a pool of liquid mercury. For each case, a critical thickness was obtained above which, cracking occurred.

In the current study, layers of alumina paste were spread on glass substrates and dried using the same infrared heating lamp employed in the CODE process. The objective of these experiments was to study the effect of layer thickness and drying conditions on crack formation and evaporation rates.

The layer thickness can vary between ~100 μm and ~800 μm in the CODE process. Accordingly, layers of 250 μm and 500 μm were chosen to be spread on substrates. For each thickness, three different drying conditions were investigated. In the first set of tests, samples were dried at room condition (~23 °C, ~55% relative humidity, ~0 m/s flow of air). In the second set of tests, the same lamp employed in the CODE process (375 Watt, 120 Volt, BR40 Clear Heat Lamp Reflector Bulb, Westinghouse Electric Corporation, Philadelphia, PA, USA) was used at a distance of 0.21 m (from lamp filament to substrate) to dry the paste. In the third set of tests, the distance was reduced to 0.16 m to increase the evaporation rate. Every experiment was repeated three times and an average was taken. Thus, a total number of 18 samples (2 (thicknesses) × 3 (drying conditions) × 3 (repetitions)) were tested.

The amount of evaporated water was calculated based on the reduction of the mass of the spread paste as a function of time. A digital analytical balance with 0.1 mg readability was continually used to measure the changes in the mass of the paste. The measurement times were also recorded to calculate the evaporation rate as well as amount of evaporation. The instantaneous water content, W (wt%), in the paste was obtained using Equation (2):

$$W = \frac{M_i - M_d}{M_d} \times 100 \tag{2}$$

where M_t is the instantaneous total mass of the paste (i.e. the reading from the digital analytical balance) and M_d is the dry mass of the paste (measured after it is totally dried in an oven).

The most influential parameter in these experiments was the heat flux density ($\dot{q}_w$) from the lamp at the surface of the paste. The value of heat flux density was estimated using Equation (3):

$$\dot{q}_w = \frac{K_1 K_2 P \cos \alpha}{A_{surf} d^2}$$

(3)

where K_1 is the radiation coefficient of the lamp (i.e. the fraction of the input electrical energy transformed to radiation energy), K_2 is the projection coefficient (i.e. the fraction of the radiation energy projected to the paste), P is the power of the lamp, α is the angle of incidence, and d is the distance between lamp filament and paste. For the current experimental setup, K_1 was ~80% [42], K_2 was estimated to be ~300% based on the shape of the lamp shading; P and α were 375 W and ~0 °, respectively. Thus, for $d=0.21$, the value of heat flux density was ~1.6 kW/m^2 and, for $d=0.16$, it was ~2.8 kW/m^2.

The results are illustrated in Figure 3 and Figure 4 for 250 μm and 500 μm thicknesses, respectively. Films with 500 μm thickness, and the highest evaporation rate, cracked at ~200 s after ~25% water was evaporated. A sample with cracks is shown in Figure 5. No cracks were observed in any other samples from the remaining five data sets, even after drying was complete. The initial drying rates (i.e. slopes of the evaporation curves) are given in Table 1. As expected, both heat flux density and layer thickness played an important role in drying of the films. Increasing the heat flux density expedites the drying process. By increasing the thickness, the volume of the paste increases without a change in surface area. Thus, the amount of water evaporated per unit volume of paste decreases.

Table 1. Initial drying rates for films.

	250 μm layer	500 μm layer
No heat	2.5 %/min	1.2 %/min
1.6 kW/m^2	4.3 %/min	2.1 %/min
2.8 kW/m^2	10.9 %/min	6.9 %/min
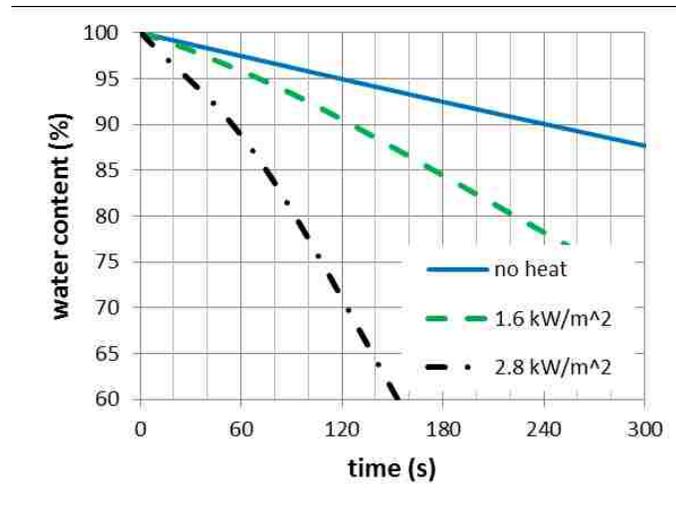
Figure 3. Evaporation curves for 250 μm layer.
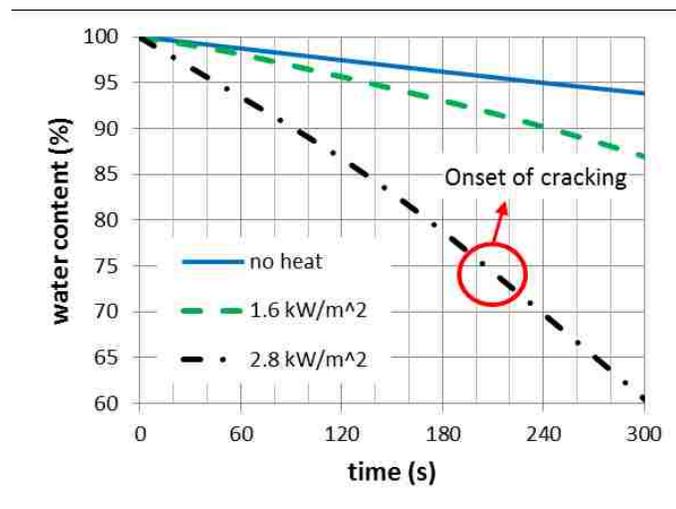
Figure 4. Evaporation curves for 500 μm layer.
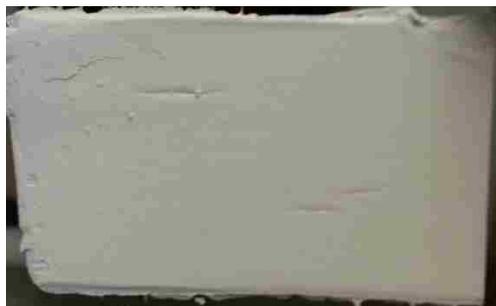
Figure 5. Cracks as a result of fast drying.

The results of these experiments were used to tune the process parameters as will be discussed in section 2.5.5. These parameters include the distance between the radiant heat source and the last deposited layer, which corresponds to evaporation rate, and the

dwell time between successive layers, which is approximately equal to drying time (since the lamp is radiating only during this time). It should be noted that these results are independent of the area and shape of the layers and can be used for any arbitrary layer geometry. In other words, the side area of a layer is negligible compared to its top area; thus, the amount of evaporated water is proportional to the area of the layer, and mass of evaporated water per unit mass of paste is independent of the area of the layer.

During the fabrication process, the new layer is deposited on the previous layer. Since the previously deposited layer is not rigid, as opposed to the glass substrate, the value of the biaxial tension exerted from the previous layer is lower than the glass. Another inaccuracy of these experiments is that in the CODE process, a portion of the heat received from the lamp is transferred to the previous layers whereas in these experiments, the heat was transferred to the glass.

2.5. FABRICATION SYSTEM

The experimental setup consists of a motion subsystem (gantry) capable of moving in three directions, extrusion devices mounted on the gantry and capable of extruding viscous ceramic paste at constant flowrates, an oil feeding device capable of controlling the level of oil in the tank, and an infrared heating subsystem capable of moving the infrared lamp and turning it on and off. The gantry is controlled by a motion card (Delta Tau Data Systems Inc., Chatsworth, CA, USA) whereas all other subsystems are controlled by a real-time control subsystem with LabVIEW (National Instruments Corp., Austin, TX, USA).

2.5.1. Motion Subsystem

The gantry consists of three orthogonal linear drives (Velmex, Bloomfield, NY, USA), each with a 508 mm travel range. The X-axis consists of two parallel slides and is used to support the Y-axis. The use of two parallel slides provides a smoother and more stable motion, thus providing a larger work space for part fabrication. The Z-axis is mounted on the Y-axis, and the extrusion mechanism is mounted on the Z-axis. Each of these axes has limit switches on both ends. Four DC servomotors (PMA22B, Pacific Scientific, Rockford, IL, USA), each with a resolver for position feedback at a resolution of 1000 counts per revolution, drive the various axes.

The three-axis gantry system is controlled using a Delta Tau Turbo PMAC card (Delta Tau Data Systems Inc., Chatsworth, CA, USA) which operates the motion subsystem through G & M code via PEWIN 32 software (Delta Tau Data Systems Inc., Chatsworth, CA, USA) running on a personal computer. As discussed in section 2.2, the G & M code is generated by the indigenously developed tool-path planning software.

2.5.2. Extrusion Subsystem

The extrusion subsystem is the core of the entire system and greatly affects the properties of the final products. Li et al. [43] investigated three mechanisms, i.e., a ram extruder, a needle valve and an auger valve, to extrude viscous suspensions. The results of that study indicated that the auger valve mechanism provided the most consistent flowrate and the highest quality extrusion-on-demand. Accordingly, the same extrusion subsystem was used in this study.

Figure 6 shows a schematic of the auger valve. The material is delivered by pressurized air to the auger chamber, and extruded by the rotating auger. The extrusion flowrate is controlled by the rotational speed of a servomotor driving the auger. Figure 7 shows the auger valve (Preeflow eco-PEN 300, ViscoTec Inc., Kennesaw, GA, USA) and its controller (eco-CONTROL EC200-K, ViscoTec Inc., Kennesaw, GA, USA) used in this study.

The eco-PEN 300 auger valve is a progressive cavity pump based dispenser which employs the "endless piston principle" technology [44]. It consists of a helical metal rotor and an elastomeric stator with double-helix holes which create several sealed cavities between them and progress down or up when the rotor turns. Every cavity has a particular volume, so a specific volume is being extruded with each rotation. The intricate geometry of the rotor and stator makes them taper and overlap, and ensures the cavities alternate to provide continuous and non-pulsing extrusion. This technology is capable of handling materials with a wide range of viscosities (10^{-3} to 10^3 Pa·s) including abrasive and shear sensitive materials [45].

The eco-CONTROL EC200-K controller is a separate desktop controller which controls the degrees of rotor rotation and the rotor speed to extrude specific volumes or continuous filaments at a specified flowrate. At the end of the extrusion, the rotor can be

reversed shortly to avoid dripping. The controller can be either operated independently with its menu interface or connected via I/O ports to the host controller.
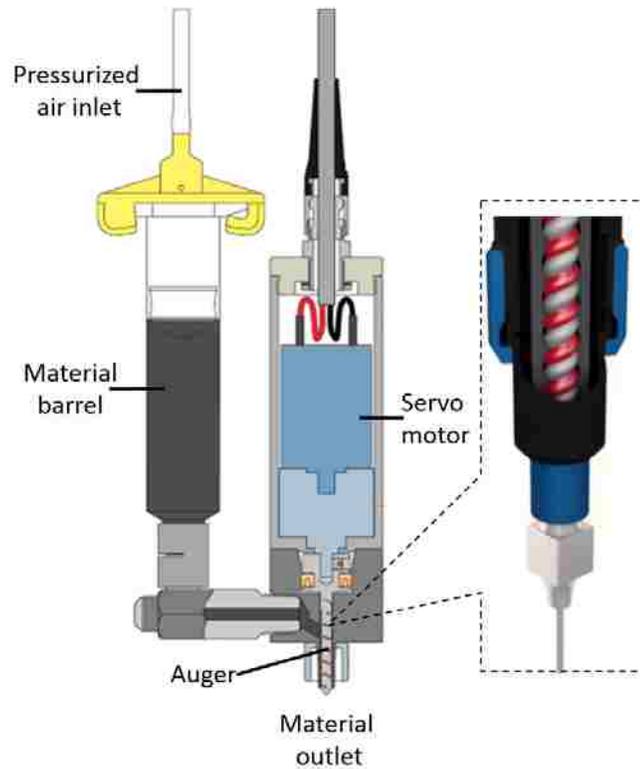
Figure 6. Schematic of an auger valve [46,47].

Figure 7. An auger valve and its controller [45].

2.5.3. Oil Filling Subsystem

The oil filling subsystem focuses on maintaining the appropriate oil level in the build tank after each layer is extruded. A mineral oil (Florasense Lamp Oil, MVP Group

International Inc., Charleston, SC, USA) was chosen as the liquid surrounding the part to preclude any interaction between the liquid and the paste. The oil level is monitored and controlled by LabVIEW using a closed loop system. The subsystem begins with an input from the G & M code signaling a desired oil level. The desired oil level is compared to the actual level, given by a level sensor, to produce an error. This error is sent to a PID controller to output a manipulated variable that gives power to a micro gear pump to control the oil flow rate from the reservoir. A large error in controlling the oil level could be detrimental to the part being fabricated. If too much oil is pumped into the tank, the top surface of the part will be covered by oil and the heat lamp cannot dry that layer. On the other hand, if the amount of oil is not sufficient and thus the oil level is one or more layers below the top layer, cracks and/or warpage might occur on the sides of the part.

2.5.4. Infrared Heating Subsystem

After a layer is extruded, the extrusion head returns to its original position in the far-left corner of the build tank to allow time for oil to be dispensed into the tank and the infrared heat source to partially dry the extruded layer. The infrared heating subsystem positions the infrared lamp (375 Watt, 120 Volt, BR40 Clear Heat Lamp Reflector Bulb, Westinghouse Electric Corporation, Philadelphia, PA, USA) above the building tank and turns it on for the amount of time specified in the G & M code. It then turns the lamp off and moves it away so that the extrusion subsystem can deposit the next layer without interfering with the heating subsystem.

Figure 8 shows thermal images from the parts in the build tank during the fabrication process before and after applying heat using the infrared lamp. Clearly, there is a considerable increase in the part temperature (~9 °C) which expedites the drying process.

2.5.5. Tuning Process Parameters

A set of experiments was designed and carried out to obtain the optimum process parameters including nozzle size, nozzle travel speed, raster spacing, layer thickness, paste flowrate, start dwell time, and early stop distance. Also, the distance between the lamp and the part, and radiation time of the lamp need to be tuned to evaporate the desired amount of water at the desired rate.
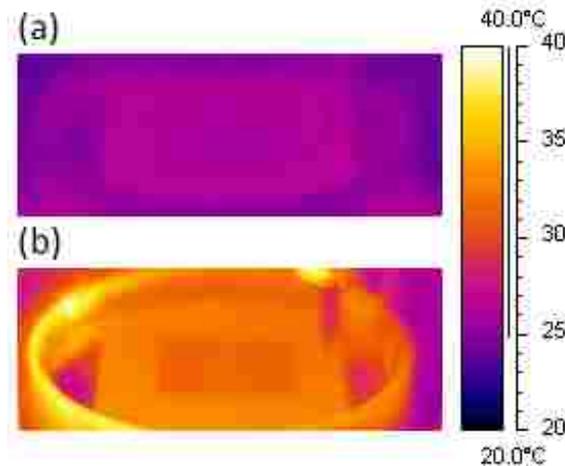
Figure 8. A thermal image of the part and substrate in the tank: (a) before radiation drying and (b) after radiation drying.

The choice of nozzle diameter depends on the required dimensional accuracy. A smaller nozzle enables printing of finer contours and lines, but prolongs the fabrication time. The extruder used in the CODE system is capable of extruding the paste from nozzles of 150-1000 μm diameter. Most of the sample parts illustrated in this paper (section 3) were fabricated with a 610 μm diameter nozzle.

The nozzle travel speed is the speed of the gantry subsystem in the horizontal (XY) plane. Clearly, a higher speed increases the productivity, but decreases the accuracy (due to vibrations and positioning errors of the gantry subsystem). Similar to many freeform extrusion fabrication systems, the bottleneck in achieving higher productivity in the CODE system is also the maximum safe travel speed. At velocities above ~30 mm/s, there is an observable deviation between the desired tool-path and the actual one. Thus, travel speeds of less than 30 mm/s were chosen to fabricate parts.

Raster spacing is the distance between the middle of the two adjacent lines of deposited material. If a solid part is to be printed, this distance should be equal to the width of the lines. Layer thickness is equal to the vertical distance between the nozzle and previous layer/substrate. Obviously, there is a compromise between accuracy and productivity when choosing raster spacing and layer thickness. For parts with simple geometry (e.g. bars and blocks), large width and thickness were selected to increase the productivity, and for delicate parts (e.g. gears), small width and thickness values were

chosen to increase the dimensional accuracy. With the current system, the width can vary from ~200 μm to ~1300 μm and the thickness can vary between ~100 μm and ~800 μm.

The required flowrate of the paste could easily be calculated, based on a continuity equation (using the cross-sectional area of extrudate and travel speed), and controlled, by adjusting the rotational speed of the auger valve. This theoretical value was fine-tuned during experiments to preclude any under/over filling.

Start dwell time is the time delay between sending a command to the auger valve to start extruding, and actual start in flow of paste. This value was measured experimentally by printing dash lines and was used in G & M codes to pause the motion of the gantry before each start.

There is also a delay between sending a command to the auger valve to stop extruding, and actual stop in flow of paste. The distance that the nozzle moves while extruding paste, after sending a command to stop the extrusion was also measured experimentally by printing dash lines. To compensate for this delay, a stop command was sent to the extruder before the nozzle reached the desired stop point.

The distance between the lamp and the part, and radiation time of the lamp, were estimated based on the drying experiments discussed in section 2.4. For a given layer thickness and heat flux density, the minimum required radiation time was obtained so that the amount of evaporation was sufficient to maintain the shape of the part. The same experiments were repeated with higher heat flux densities until a crack was observed in the part. In this way, the maximum heat flux density and minimum radiation time were determined for each layer thickness.

2.6. POST-PROCESSING

Once a part was completely formed, the oil bath was drained and the piece was bulk dried to remove remaining water. The binder was then removed through a burnout process. The calcined or "brown" part was then sintered to obtain a final part.

2.6.1. Bulk Drying

Two different methods were used to eliminate the remaining water content in the part. In the first approach, water in the part was first frozen and then removed through sublimation by using a freeze dryer (Genesis 25L, VirTis, Stone Ridge, NY, USA). The

temperature was set at -10 °C and pressure was 2.0 Pa (15 mTorr) for three days. Humid drying was used as an alternative approach. An environmental chamber (LH-1.5, Associated Environmental Systems, Ayer, MA, USA) was used to control the temperature and humidity during the drying process. After several experiments, 75% relative humidity at 25 °C was determined for the first 4-6 hours of drying. This condition guaranteed safe drying (i.e. no cracks or warpage). After the first stage of drying, shrinkage was completed and higher drying rates could be achieved without introducing flaws by increasing the temperature. Figure 9 shows the drying behavior of a sample part (5×5×2 cm^3) for which the drying temperature was held constant (at room temperature) throughout the process. From the figure, ~65 hours was required to dry the part. However, ~20 hours was achievable by increasing the temperature in the second stage. The properties of the parts produced using freeze drying and humid drying are compared in section 4.
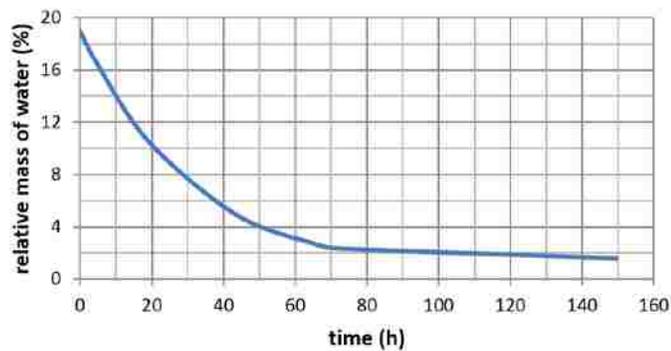
Figure 9. Drying behavior of a sample part at room temperature.

2.6.2. Binder Burnout and Sintering

A heating rate of 1 °C/min was chosen for the binder burnout process to avoid high weight reduction rates. The parts were maintained at 450 °C for two hours. The samples were then densified with a heating rate of 5 °C/min in an electric furnace (Deltech Inc., Denver, CO, USA). They were sintered at four different temperatures (1550, 1600, 1650 and 1700 °C) and two different hold times (2 and 5 h). The microstructure and density of each group were examined and are discussed in Section 4.

3. SAMPLE PARTS

3.1. IMPELLER

To examine the performance of extrusion-on-demand in practice, fairly complex parts with numerous starts and stops were printed. Figure 10 shows an example of these parts, which is an alumina impeller in the green state. As could be seen from the picture, no visible printing flaw is observed in the part.
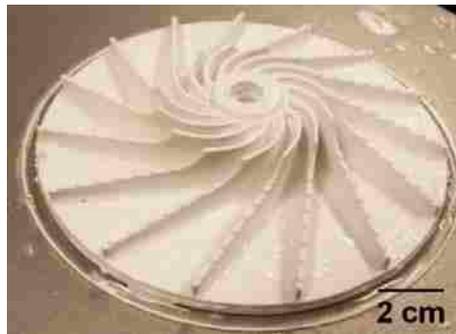
Figure 10. An alumina impeller in the green state.

3.2. GEAR

To investigate the capabilities of the process and system to fabricate solid and monolithic parts with complex geometries, a solid gear was chosen and successfully built. As shown in Figure 11, the part is free of pores between contours and lines.
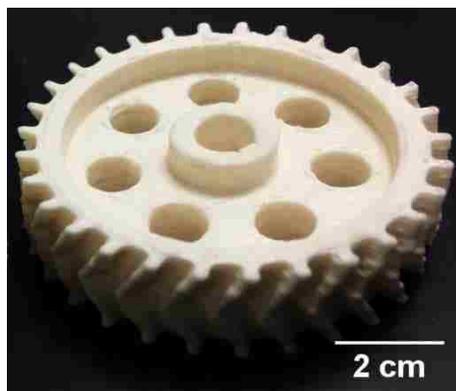
Figure 11. A sintered alumina gear.

3.3. SMART REFRACTORY LINING BLOCK

As an application of the CODE process, fabrication of smart lining blocks was considered. It is of prime importance to monitor several parameters (e.g. temperature,

pressure, and spalling of walls) in the integrated gasification combined cycle of coal and other carbon-containing fuels. A novel approach to this end is embedding several sensors in the linings of the chamber during the fabrication process. This approach could lead to more accurate measurements, better protection of the sensors, and maintenance of the strength of the linings. Figure 12 demonstrates a lining block in which a mock-up sensor is successfully embedded during the fabrication process.
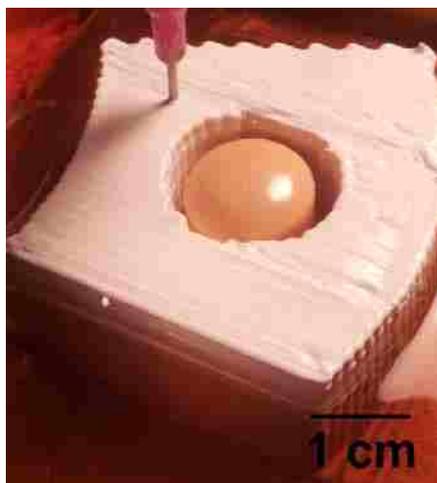
Figure 12. A refractory lining block with embedded mock-up sensor during the fabrication process.

3.4. CATALYST SUPPORT

An important characteristic of catalyst supports is their surface area to volume ratio. A scaffold structure has a high area to volume ratio; however, it is not feasible to fabricate the structure using traditional manufacturing processes. The CODE process was used to fabricate scaffolds as shown in Figure 13. They were successfully coated with a catalyst as illustrated in Figure 14.
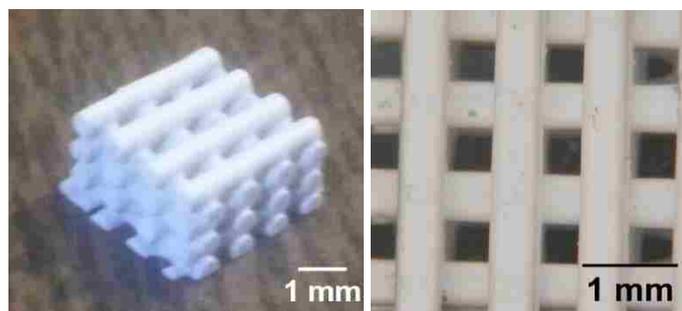
Figure 13. Printed scaffolds before coating.
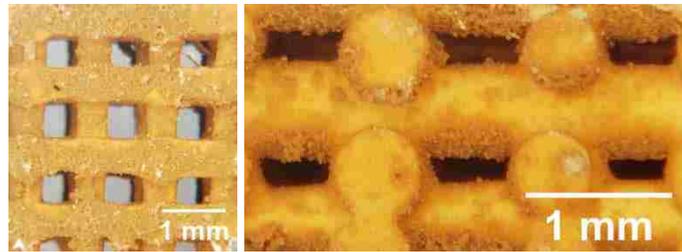
Figure 14. Scaffolds coated with a thin layer of catalyst.

3.5. PROSTHETIC HIP JOINT

Alumina is a common material used to produce prosthetic hip joints due to its hardness and biocompatibility [48]. Additive manufacturing of these joints can enable expedited production of custom-made joints at a reasonable cost. A spherical solid part resembling a hip joint was fabricated using the CODE process (see Figure 15). An advantage of this process is producing relatively strong green parts which could be readily ground to improve the surface quality prior to sintering. Figure 16 shows the same part after manual grinding. Clearly, there is a significant improvement in the surface quality.
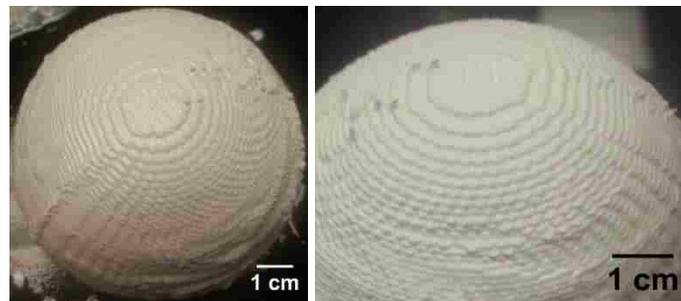
Figure 15. A solid spherical part resembling a prosthetic hip joint in the green state.
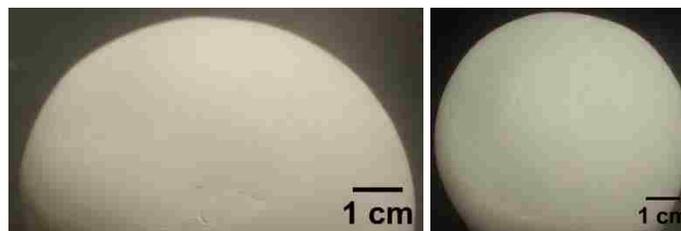
Figure 16. A spherical part after manual grinding in the green state.

3.6. HIGHER RESOLUTION PARTS

Clearly, another way to improve the surface quality is using a finer nozzle. Figure 17 shows two sintered parts; the one on top was printed using a nozzle with an internal diameter of 254 μm. The bottom part was printed using a nozzle of 610 μm diameter.
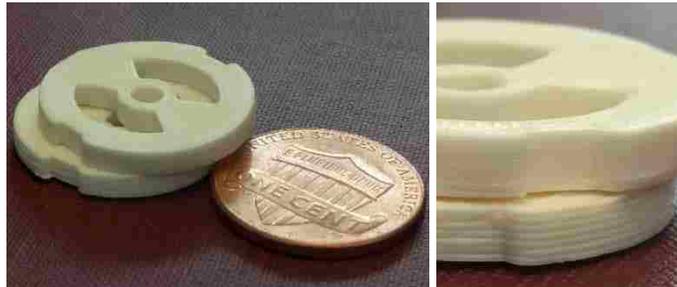
Figure 17. A part printed with a fine nozzle on top of the same part printed with a large nozzle.

4. PROPERTIES OF PRINTED PARTS

4.1. DENSITY

Archimedes' technique was used to measure the density of the printed parts after sintering. After the dry mass was recorded, samples were saturated by submersion in distilled water and placing them under vacuum for 12 h. The saturated and suspended masses were then measured to calculate the final density. The results are given in Table 2.

Table 2. Relative density of parts sintered at different schedules.

Sintering temperature (°C)	Sintering time (h)	Relative density if freeze dried (%)	Relative density if humid dried (%)
1550	2	-	97.7
1550	5	93.6	97.8
1600	5	95.7	98.5
1650	5	97.1	-
1700	5	98.2	-

When using the same sintering schedule, the density of freeze dried samples are considerably lower than samples dried in the humid environment. This is partly due to voids caused by ice crystal formation during freezing of samples as discussed in [49]. In addition, expansion of water (~9 vol%) during freezing results in a lower green body density. Unlike humid drying where ceramic particles are dispersed in a liquid medium

and can easily move during drying (causing shrinkage), in freeze drying, particles are not free to move during the drying process. Accordingly, the relative density of freeze dried parts are considerably lower than the humid dried parts (52% vs. 61%) and a higher sintering temperature/time is required to densify the freeze dried samples. Nevertheless, if sintered at appropriate conditions, dense parts could be fabricated using the CODE process. The remaining porosity (1.5%) is attributed to residual air bubbles in the paste and/or binder agglomerates which create voids during binder removal. The size of these defects is typically tens of micrometers.

4.2. MICROSTRUCTURE

Samples were polished to a 0.25μm finish using diamond particles and thermally etched at 1300 °C for 30 min to reveal their microstructure. Microstructural analysis was performed using a scanning electron microscope (Helios Nano Lab 600, FEI Corp., Eindhoven, Netherlands). Figure 18 shows the cross-section and microstructure of a printed sample (humid dried and sintered at 1550 °C for 2h). No printing flaws are observed in these pictures. The grains are equiaxed and small (<5 µm).
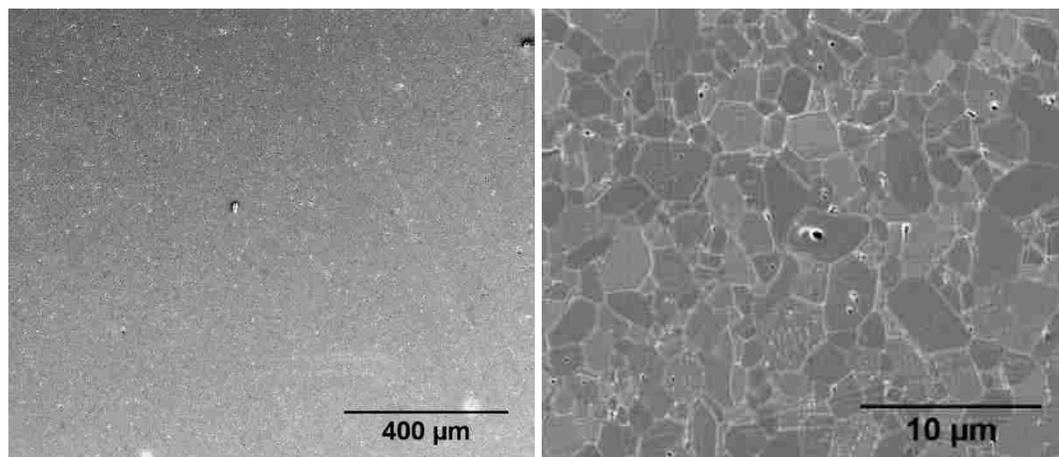
Figure 18. Cross-section and microstructure of a printed sample (humid dried and sintered at 1550 °C for 2h).

5. CONCLUSION

A freeform extrusion fabrication process for producing solid ceramic parts was introduced in this paper. The developed tool-path planning software, paste preparation

steps, subsystems of the fabrication system, and post-processing were explained. To examine the capabilities of the process, several parts for various applications were built and their density and microstructure studied. The CODE process has been shown to be able to produce large complex parts (up to tens of centimeters) with near theoretical density (>98%) and a uniform microstructure. Other extensive studies [50–52] demonstrated capabilities of CODE to produce mechanically strong parts from different materials. Other advantages include facile preparation of feedstock, low amount of binder content expediting the post-processing, feasibility of embedding sensors [53], and the capability of grinding products in the green state.

ACKNOWLEDGEMENTS

REFERENCES

[1]   J. Grau, J. Moon, S. Uhland, M.J. Cima, E. Sachs, High green density ceramic components fabricated by the slurry-based 3DP process, in: Solid Free. Fabr. Symp., Austin, TX, USA, 1997: pp. 371–378.

[2]   R. Noguera, M. Lejeune, T. Chartier, 3D fine scale ceramic components formed by ink-jet prototyping process, J. Eur. Ceram. Soc. 25 (2005) 2055–2059. doi:10.1016/j.jeurceramsoc.2005.03.223.

[3]   E.A. Griffin, S. McMillin, Selective laser sintering and fused deposition modeling processes for functional ceramic parts, in: Solid Free. Fabr. Symp., Austin, TX, USA, 1995: pp. 25–30.

[4]   M.L. Griffith, J.W. Halloran, Freeform fabrication of ceramics via stereolithography, J. Am. Ceram. Soc. 79 (1996) 2601–2608. doi:10.1111/j.1151-2916.1996.tb09022.x.

[5]   C. Griffin, J. Daufenbach, S. McMillin, Desktop manufacturing: LOM vs pressing, Am. Ceram. Soc. Bull. 73 (1994) 109–113.

[6] N. Travitzky, A. Bonet, B. Dermeik, T. Fey, I. Filbert-Demut, L. Schlier, T. Schlordt, P. Greil, Additive manufacturing of ceramic-based materials, Adv. Eng. Mater. 16 (2014) 729–754. doi:10.1002/adem.201400097.

[7] M.A. Jafari, W. Han, F. Mohammadi, A. Safari, S.C. Danforth, N. Langrana, A novel system for fused deposition of advanced multiple ceramics, Rapid Prototyp. J. 6 (2000) 161–175.

[8] G.E. Hilmas, J.L. Lombardi, R.A. Hoffman, Advances in the fabrication of functionally graded materials using extrusion freeform fabrication, Funct. Graded Mater. (1997) 319–324. doi:10.1016/B978-044482548-3/50053-6.

[9] M.C. Leu, B.K. Deuser, L. Tang, R.G. Landers, G.E. Hilmas, J.L. Watts, Freeze-form extrusion fabrication of functionally graded materials, CIRP Ann. - Manuf. Technol. 61 (2012) 223–226. doi:10.1016/j.cirp.2012.03.050.

[10] K. Stuffle, A. Mulligan, P. Calvert, J. Lombardi, Solid freebody forming of ceramics from polymerizable slurry, in: Solid Free. Fabr. Symp., Austin, TX, USA, 1993: pp. 60–63.

[11] R. Vaidyanathan, J. Walish, J.L. Lombardi, S. Kasichainula, P. Calvert, K.C. Cooper, The extrusion freeforming of functional ceramic prototypes, J. Miner. Met. Mater. Soc. (2000) 34–37. doi:10.1007/s11837-000-0066-4.

[12] S.C. Danforth, Fused deposition of ceramics: a new technique for the rapid fabrication of ceramic components, Mater. Technol. 10 (1995) 144–146.

[13] M.K. Agarwala, V.R. Jamalabad, N.A. Langrana, A. Safari, P.J. Whalen, S.C. Danforth, Structural quality of parts processed by fused deposition, Rapid Prototyp. J. 2 (1996) 4–19. doi:10.1108/13552549610732034.

[14] G.M. Lous, I.A. Cornejo, T.F. McNulty, A. Safari, S.C. Danforth, Fabrication of piezoelectric ceramic/polymer composite transducers using fused deposition of ceramics, J. Am. Ceram. Soc. 83 (2000) 124–128. doi:10.1111/j.1151-2916.2000.tb01159.x.

[15] A. Bandyopadhyay, P.K. Panda, M.K. Agarwala, S.C. Danforth, A. Safari, Processing of piezocomposites by fused deposition technique, J. Am. Ceram. Soc. 80 (1997) 1366–72. doi:10.1111/j.1151-2916.1997.tb02993.x.

[16] A. Safari, M. Allahverdi, E.K. Akdogan, Solid freeform fabrication of piezoelectric sensors and actuators, J. Mater. Sci. 41 (2006) 177–198. doi:10.1007/s10853-005-6062-x.

[17] S. Iyer, J. McIntosh, A. Bandyopadhyay, N. Langrana, A. Safari, S.C. Danforth, R.B. Clancy, C. Gasdaska, P.J. Whalen, Microstructural characterization and mechanical properties of Si3N4 formed by fused deposition of ceramics, Int. J. Appl. Ceram. Technol. 5 (2008) 127–137. doi:10.1111/j.1744-7402.2008.02193.x.

[18]   J. Cesarano III, R. Segalmen, P. Calvert, Robocasting provides moldless fabrication from slurry deposition, Ceram. Ind. 148 (1998) 94–102.

[19]   H.B. Denham, J. Cesarano III, B.H. King, P. Calvert, Mechanical behavior of robocast alumina, in: Solid Free. Fabr. Symp., Austin, TX, USA, 1998: pp. 589–596.

[20]   S. Michna, W. Wu, J.A. Lewis, Concentrated hydroxyapatite inks for direct-write assembly of 3-D periodic scaffolds, Biomaterials. 26 (2005) 5632–5639. doi:10.1016/j.biomaterials.2005.02.040.

[21]   J. Lewis, J. Smay, J. Stuecker, J. Cesarano, Direct ink writing of three-dimensional ceramic structures, J. Am. Ceram. Soc. 89 (2006) 3599–3609. doi:10.1111/j.1551-2916.2006.01382.x.

[22]   K. Cai, B. Román-Manso, J.E. Smay, J. Zhou, M.I. Osendi, M. Belmonte, P. Miranzo, Geometrically complex silicon carbide structures fabricated by robocasting, J. Am. Ceram. Soc. 95 (2012) 2660–66. doi:10.1111/j.1551-2916.2012.05276.x.

[23]   M. Houmard, Q. Fu, M. Genet, E. Saiz, A.P. Tomsia, On the structural, mechanical, and biodegradation properties of HA/β-TCP robocast scaffolds., J. Biomed. Mater. Res. B. Appl. Biomater. 101 (2013) 1233–42. doi:10.1002/jbm.b.32935.

[24]   T. Schlordt, S. Schwanke, F. Keppner, T. Fey, N. Travitzky, P. Greil, Robocasting of alumina hollow filament lattice structures, J. Eur. Ceram. Soc. 33 (2013) 3243–48. doi:10.1016/j.jeurceramsoc.2013.06.001.

[25]   T. Huang, M.S. Mason, G.E. Hilmas, M.C. Leu, Freeze-form extrusion fabrication of ceramics, in: Solid Free. Fabr. Symp., Austin, TX, USA, 2005: pp. 73–85.

[26]   T. Huang, G.E. Hilmas, W.G. Fahrenholtz, M.C. Leu, Dispersion of zirconium diboride in an aqueous, high-solids paste, Int. J. Appl. Ceram. Technol. 4 (2007) 470–79.

[27]   T. Huang, M.N. Rahaman, N.D. Doiphode, M.C. Leu, B.S. Bal, D.E. Day, Freeze extrusion fabrication of 13-93 bioactive glass scaffolds for repair and regeneration of load-bearing bones, Ceram. Trans. 228 (2011) 45–55. doi:10.1007/s10856-011-4236-4.

[28]   A. Li, A.S. Thornton, B. Deuser, J.L. Watts, M.C. Leu, G.E. Hilmas, R.G. Landers, Freeze-form extrusion fabrication of functionally graded material composites using zirconium carbide and tungsten, in: Solid Free. Fabr. Symp., Austin, TX, USA, 2012: pp. 467–79.

[29]   A.S. Thornton, Freeze-form extrusion fabrication of boron carbide, Missouri University of Science and Technology, 2014.

[30] M.S. Mason, T. Huang, R.G. Landers, M.C. Leu, G.E. Hilmas, Aqueous-based extrusion of high solids loading ceramic pastes: Process modeling and control, J. Mater. Process. Technol. 209 (2009) 2946–2957. doi:10.1016/j.jmatprotec.2008.07.004.

[31] X. Zhao, R.G. Landers, M.C. Leu, Adaptive extrusion force control of freeze-form extrusion fabrication processes, J. Manuf. Sci. Eng. 132 (2010) 1–9. doi:10.1115/1.4003009.

[32] B.K. Deuser, L. Tang, R.G. Landers, M.C. Leu, G.E. Hilmas, Hybrid extrusion force-velocity control using freeze-form extrusion fabrication for functionally graded material parts, J. Manuf. Sci. Eng. 135 (2013). doi:10.1115/1.4024534.

[33] H. Zomorodi, R.G. Landers, Extrusion based additive manufacturing using explicit model predictive control, in: Am. Control Conf., Boston, MA, USA, 2016: pp. 1747–1752.

[34] W. Li, A. Ghazanfari, D. McMillen, M. Leu, G. Hilmas, J. Watts, Fabricating ceramic components with water dissolvable support structures by the ceramic on-demand extrusion process, CIRP Ann. - Manuf. Technol. (2017).

[35] A. Ghazanfari, W. Li, M.C. Leu, Adaptive rastering algorithm for freeform extrusion fabrication processes, Virtual Phys. Prototyp. 10 (2015) 163–172. doi:10.1080/17452759.2015.1096798.

[36] S.W. Sofie, F. Dogan, Freeze casting of aqueous alumina slurries with glycerol, J. Am. Ceram. Soc. 84 (2001) 1459–1464. doi:10.1111/j.1151-2916.2001.tb00860.x.

[37] M.N. Rahaman, Ceramic processing and sintering, Taylor and Francis, Boca Raton, FL, 2007.

[38] F. Lange, Chemical solution routes to single-crystal thin films, Science (80-.). 273 (1996) 903–909.

[39] E. Santanach Carreras, F. Chabert, D.E. Dunstan, G. V. Franks, Avoiding "mud" cracks during drying of thin films from aqueous colloidal suspensions, J. Colloid Interface Sci. 313 (2007) 160–168. doi:10.1016/j.jcis.2007.03.076.

[40] D.M. Holmes, R. Vasant Kumar, W.J. Clegg, Cracking during lateral drying of alumina suspensions, J. Am. Ceram. Soc. 89 (2006) 1908–1913. doi:10.1111/j.1551-2916.2006.01053.x.

[41] R.C. Chiu, T.J. Garino, M.J. Cima, Drying of granular ceramic films: I, effect of processing variables on cracking behavior, J. Am. Ceram. Soc. 76 (1993) 2257–2264. doi:10.1111/j.1151-2916.1993.tb07762.x.

[42] K. Narisada, D. Schreuder, Light pollution handbook, volume 1, Springer, Dordrecht, Netherlands, 2004.

[43] W. Li, A. Ghazanfari, M.C. Leu, R.G. Landers, Methods of extrusion on demand for high solids loading ceramic paste in freeform extrusion fabrication, in: D. Bourell, J. Beaman, R. Crawford, S. Fish, H. Marcus, C. Seepersad (Eds.), Solid Free. Fabr. Symp., Austin, TX, USA, 2015: pp. 332–345.

[44] Micro dispensing in perfection, (n.d.). http://www.preeflow.com/media/preeflow2014english.pdf (accessed July 1, 2016).

[45] P. Swanson, The "endless piston" pump technology for precision dispensing, Oxfordshire, England, 2012. http://www.intertronics.co.uk/articles/wp12-1_endless_piston_pump-technology_for_precision_dispensing.pdf.

[46] Auger valve dispensing, (2003) 5. https://www.smtnet.com/library/files/upload/EFD_-_Auger_Valve_Dispensing.pdf (accessed July 1, 2016).

[47] Preeflow one for all, (n.d.). http://www.preeflow.com/en/media- center/videos/ (accessed July 1, 2016).

[48] B.J. McEntire, B.S. Bal, M.N. Rahaman, J. Chevalier, G. Pezzotti, Ceramics and ceramic coatings in orthopaedics, J. Eur. Ceram. Soc. 35 (2015) 4327–4369. doi:10.1016/j.jeurceramsoc.2015.07.034.

[49] J. Li, M.C. Leu, G.E. Hilmas, Effects of temperature on aqueous freeform extrusion fabrication, in: D. Bourell, J. Beaman, R. Crawford, S. Fish, H. Marcus, C. Seepersad (Eds.), Solid Free. Fabr. Symp., Austin, TX, USA, 2015: pp. 319–331.

[50] A. Ghazanfari, W. Li, M. Leu, J. Watts, G. Hilmas, Mechanical characterization of parts produced by ceramic on-demand extrusion process, Int. J. Appl. Ceram. Technol. (2017). doi:10.1111/ijac.12665.

[51] A. Ghazanfari, W. Li, M.C. Leu, J.L. Watts, G.E. Hilmas, Additive manufacturing and mechanical characterization of high density fully stabilized zirconia, Ceram. Int. (2017). doi:10.1016/j.ceramint.2017.01.154.

[52] W. Li, A. Ghazanfari, D. McMillen, M.C. Leu, G.E. Hilmas, J.L. Watts, Properties of partially stabilized zirconia components fabricated by the ceramic on-demand extrusion process, in: D.L. Bourell, R.H. Crawford, C.C. Seepersad, J.J. Beaman, S. Fish, H. Marcus (Eds.), Solid Free. Fabr. Symp., Austin, TX, USA, 2016: pp. 916–928.

[53] A. Ghazanfari, W. Li, M.C. Leu, Y. Zhuang, J. Huang, Advanced ceramic components with embedded sapphire optical fiber sensors for high temperature applications, Mater. Des. 112 (2016) 197–206. doi:10.1016/j.matdes.2016.09.074.

II. MECHANICAL CHARACTERIZATION OF PARTS PRODUCED BY CERAMIC ON-DEMAND EXTRUSION PROCESS[1]

ABSTRACT

Ceramic On-Demand Extrusion (CODE) is an additive manufacturing process recently developed to produce dense three-dimensional ceramic components. In this paper, the properties of parts produced using this freeform extrusion fabrication process are described. High solids loading (~60 vol%) alumina paste was prepared to fabricate parts and standard test methods were employed to examine their properties including density, strength, Young's modulus, Weibull modulus, toughness, and hardness. Microstructural evaluation was also performed to measure the grain size and critical flaw size. The results indicate that the properties of parts surpass most other ceramic additive manufacturing processes and match conventional fabrication techniques.

1. INTRODUCTION

Additive Manufacturing (AM) of advanced ceramics has several advantages over traditional processing techniques including ease of fabricating geometrically complex parts and reduction of manufacturing costs for one-of-a-kind parts or small batches. Accordingly, many researchers have either modified existing AM processes, which were designed to fabricate polymer components, for fabrication of ceramic components, or invented novel AM technologies specifically for ceramics. The former includes Selective Laser Sintering [1], Stereolithography [2], Three-Dimensional Printing [3], Ink-jet Printing [4], Laminated Object Manufacturing [5], and Fused Deposition of Ceramics [6]. The latter includes Extrusion Freeform Fabrication [7], Robocasting [8], and Freeze-form Extrusion Fabrication [9]. A comprehensive review on additive manufacturing of ceramic-based materials was recently published by Travitzky et al. [10].

Many efforts to additively manufacture ceramic components resulted in parts with defects (i.e., flaws or large porosity as a result of the AM process). It is well-known that

---

the properties of ceramics are very sensitive to porosity, and they would be expected to exhibit poor mechanical properties even at 80% relative density (e.g., [11]). Although these parts may have remarkable geometrical complexity and be suitable for some applications, they are not apt to be used as structural ceramics. In many cases, the mechanical properties of these parts are so poor that they are not even reported in papers and technical reports. According to Zocca et al. [12], AM of monolithic ceramics, enabling the components to match the physical and chemical properties of their conventionally manufactured counterparts, is still a challenge and remains the most important task that needs to be solved to promote AM of ceramics to more than a niche technology. However, extrusion-based and lithography-based AM processes are promising because they are capable of producing dense ceramic parts (>95% of theoretical density).

The Ceramic On-Demand Extrusion (CODE) process is a novel freeform extrusion fabrication technique capable of making large, complex parts with near theoretical density (>98%). Ghazanfari et al. [13] introduced and developed this process and employed it to demonstrate fabricating several sample parts for various applications. The objective of the present study is to comprehensively characterize ceramic parts produced using the CODE process. Density, strength, fracture toughness, hardness, stiffness and microstructure of aluminum oxide (Al_2O_3) parts were examined and compared to the properties of Al_2O_3 parts fabricated using conventional manufacturing and other AM processes.

2. EXPERIMENTAL PROCEDURE

2.1. PASTE PREPARATION

The paste is made of a commercially available alumina powder (A-16SG, Almatis Inc., Leetsdale, PA), deionized water, ammonium polymethacrylate (DARVAN® C-N, Vanderbilt Minerals, Norwalk, CT), and cold-water-dispersible methylcellulose (Methocel J5M S, Dow Chemical Company, Midland, MI). The powder properties are listed in Table 1.

The alumina powder was dispersed in water using 1 mg Darvan C per square meter of surface area of powder and ball-milled for 15 hours to break up agglomerates and to produce a uniform mixture. Methylcellulose dissolved in water (<1 vol%) was

used as a binder to increase paste viscosity and to assist in forming a stronger green body after drying. Binder was chemically surface-treated by the manufacturer to become temporarily insoluble in cold water. This time-delay in dissolving the binder allows for the formation of a homogeneous dispersion of binder in cold water and eliminates the necessity to increase water temperature to achieve a uniform dispersion. A vacuum mixer (Model F, Whip Mix, Louisville, KY) was employed to mix the paste homogeneously without introducing air bubbles for 12 minutes. Finally, a vibratory table (Syntron Material Handling, Saltillo, MS) was used to remove the remaining air bubbles.

Table 1. Powder properties.

Name	Particle Size (µm)	Surface Area (m²/g)	Purity
Al_2O_3 (A-16SG)	0.34	9.44	99.8%

2.2. PROCESSING

In the CODE process, viscous colloids of ceramic particles are extruded through a circular nozzle at controlled flowrates. The extrusion workhead is mounted on a gantry and can move in the X, Y and Z directions through G & M code commands[2]. The extrudate is deposited on a substrate located in a tank designed to hold a fluid medium. Once the deposition of each layer is completed, a liquid feeding subsystem pumps oil into the tank, surrounding the deposited layer, to preclude undesirable water evaporation from the sides of the deposited layers. The level of the oil is controlled so that it reaches just below the top surface of the part being fabricated. Infrared radiation is then used to uniformly dry the just deposited layer so that the part being fabricated can maintain its shape when the next layers are being deposited to build the part. The part is fabricated in a layer-by-layer fashion by repeating the layered deposition followed by layered radiation drying with an oil surrounding the already deposited layers during the part fabrication process. A schematic of the process is shown in Figure 1. Once the fabrication process is completed, the remaining water content in the fabricated part is removed further by bulk

---

[2] G & M codes are a set of letters and numbers used to program the movements and other actions (tool change, end of program, etc.) of a CNC machine.

drying to obtain green parts. The post-processing includes removing the binder content at elevated temperatures and then using a ceramic sintering process to obtain a dense part.

The experimental setup consists of a motion subsystem (gantry) capable of moving in three directions, an extrusion head mounted on the gantry and capable of extruding viscous ceramic pastes at controlled flowrates, an oil feeding device capable of controlling the level of the oil in the tank, and an infrared heating subsystem capable of moving the infrared lamp and turning it on and off. The gantry is controlled by a motion card (Delta Tau Data Systems Inc., Chatsworth, CA) whereas all other subsystems are controlled by a real-time control subsystem with LabVIEW (National Instruments Corp., Austin, TX). More details on the CODE system are available from [13] and [14].
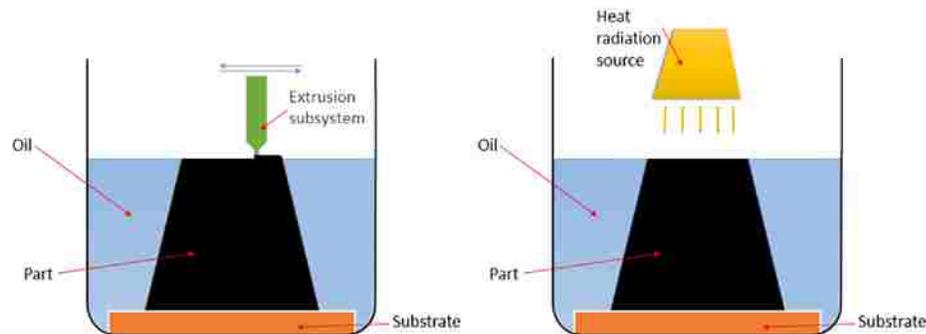
Figure 1. Schematic of the Ceramic On-Demand Extrusion process.

Thirty test bars were fabricated using the CODE process to examine the properties of the parts produced by this process. As shown in Figure 2, six bars were printed at a time. The printing was performed in the longitudinal direction of the bars. The as-printed size of the bars was $72 \times 7.8 \times 5.6$ mm^3 in length, width, and height, respectively. The process parameters used to print the bars are given in Table 2.

Table 2. Printing parameters used in the CODE process to fabricate test bars.

Nozzle diameter (μm)	610
Nozzle travel speed (mm/s)	30
Layer thickness (μm)	400
Number of layers	14
Line spacing (μm)	600
Number of lines in a layer	13
Lamp distance (m)	0.25
Radiation time (s)	30

2.3. POST-PROCESSING

        Once the parts were completely formed, the oil bath was drained and the fabricated pieces were dried. Humid drying was used to eliminate the remaining water in the parts. An environmental chamber (LH-1.5, Associated Environmental Systems, Ayer, MA) was employed to control the temperature and humidity during the drying process. After several experiments, 75% relative humidity at 25 °C was determined for the first 4-6 hours of drying. This condition guaranteed safe drying (i.e. no cracks or warpage). After the first stage of drying, the shrinkage ends and higher drying rates could be achieved, without introducing flaws, by increasing the temperature up to ~70 °C.

        The binder was then removed through a burnout process. A 1 °C/min heating rate was chosen to avoid large weight reduction rates. The parts were maintained at 450 °C for two hours. The calcined or "brown" parts were then sintered with a heating rate of 5 °C/min in an electric furnace (Deltech Inc., Denver, CO). The parts were then sintered in the same furnace at 1550 °C for 1.5 h followed by cooling to room temperature at a rate of 10 °C/min.

Figure 2. Test bars during the CODE process.

2.4. TESTS

        The size of the bars was measured with digital calipers after printing, drying, and sintering to calculate the shrinkage rate during the drying and sintering processes. Archimedes' technique was performed to measure the density of the printed parts after sintering. After the dry mass was recorded, samples were saturated by submersion in

distilled water under vacuum for ~12 hours. The saturated and suspended masses were then measured to calculate the final density.

Microstructure images were obtained from sections of the sintered test bars using Scanning Electron Microscopy (SEM). Specimens were polished to a 0.25 μm diamond finish using successively finer diamond abrasives with the following scheme: a 220-grit metal-bond diamond grinding disk for 10 min; a 600-grit disk for 10 min; a 1200-grit disk for 10 min; a 3 μm diamond lapping film for 5 min; a 2 μm diamond paste for 40 min; a 1 μm diamond paste for 90 min; and a 0.25 μm diamond paste for 150 min. Thermal etching was used to reveal the grain boundaries by placing the polished specimens in an electric furnace (Deltech Inc., Denver, CO) at 1300 °C for 30 min with a heating and cooling rate of 10 °C/min. A scanning electron microscope (Helios Nanolab 600, FEI, Hillsboro, OR) was employed to observe the specimens at various magnifications ranging from 100-20,000X. The cross-sections of the bars before and after the flexural tests were also observed under an optical microscope (KH-3000, Hirox, Hackensack, NJ) to examine possible flaws.

Four-point bending tests were performed at room temperature according to ASTM C1161 [15] to measure flexural strengths for 24 test specimens. A fully automated surface grinder (Chevalier, FSG-3A818, Santa Fe Springs, CA) was used to machine the specimens to standard "B" bars ($3 \times 4 \times 45$ mm^3). The sides and top surface of the bars were machined with a 600-grit diamond abrasive wheel. A 1200-grit wheel was used to grind the tensile surface. The bars were then manually chamfered using a 1200-grit metal-bond diamond grinding disk. Flexural strengths were measured using a fully articulating B-bar fixture with an outer span of 40 mm and an inner span of 20 mm (shown in Figure 3) in a screw-driven instrumented load frame (5881; Instron, Norwood, MA). The crosshead speed was 0.5 mm/min. Weibull modulus was calculated according to ASTM C1239 [16]. Young's modulus was determined using a deflectometer (a linear variable differential transformer) measuring the deflection of the center of the test bar during strength testing as shown in Figure 3.

Fracture toughness was measured by using the chevron-notched beam test specimens in four-point bending with a fully articulating test fixture for configuration A (L=50 mm, B=3 mm, W=4 mm, and a_0=0.8 mm) according to ASTM C1421 [17]. Six test

bars were ground to standard size using the same surface grinder employed for flexural tests. The chevron notches were machined using a dicing saw (Accu-cut 5200, Aremco Products, Ossining, NY) with a 0.15 mm thick diamond wafering blade. The same fixture and load frame used for flexural tests were employed to break the chevron-notched beams with a crosshead speed of 0.02 mm/min. The notch dimensions were then measured using an optical microscope (KH-3000, Hirox, Hackensack, NJ).

Figure 3. Fully articulating test fixture and deflectometer.

Vickers indentation test was carried out according to ASTM C1327 [18] using a microhardness tester (Duramin 5; Struers, Cleveland, OH) to measure hardness. Four samples were polished to a 0.25 μm diamond finish using the same scheme explained for microstructural tests. Hardness was calculated from five indents per sample. The indenter was pressed against the parts with a force of 4.91 N for 10 s. The indentation size was measured using an optical microscope with a 40X lens.

3. RESULTS AND DISCUSSION

3.1. SHRINKAGE AND DENSITY

The size of the bars reduced to $71 \times 7.5 \times 5.4$ mm^3 after drying, showing 1.4%, 3.8% and 3.6% reduction in length, width and height, respectively. This indicates a volumetric

shrinkage of 8.6%. The dimensions of the bars were $62.8 \times 6.3 \times 4.6$ mm^3 after sintering, showing 12.8%, 19.2% and 17.9% reduction in length, width and height, respectively, compared to the wet (as-printed) samples. This indicates a volumetric shrinkage of 42.1% compared to the wet samples. The results are given in Table 3 along with relative densities.

Table 3. Amount of shrinkage and relative densities of parts at each stage.

	Size (mm)	Linear shrinkage (%)	Volumetric shrinkage (%)	Relative density (%)
As-printed	$72.0 \times 7.8 \times 5.6$	-	-	57[*]
Dried	$71.0 \times 7.5 \times 5.4$	$1.4 \times 3.8 \times 3.6$	8.6	62[*]
Sintered	$62.8 \times 6.3 \times 4.6$	$12.8 \times 19.2 \times 17.9$	42.1	98

[*] These densities are calculated by dividing mass of alumina powder by volume of the part.

To examine whether the anisotropy in shrinkage is a result of printing direction or the geometry of the part, three blocks were printed. The initial size of the blocks was $20 \times 19.8 \times 20$ mm^3 and it reduced to $16.7 \times 16.6 \times 16.6$ mm^3, showing 16.5%, 16.2% and 17.0% reduction in length, width, and height, respectively. This shows an almost isotropic shrinkage and indicates that the percentage of shrinkage in each direction is mostly determined by the part geometry. It is hypothesized that friction between specimen and substrate causes the anisotropy in the shrinkage of long bars during drying and sintering; i.e. due to friction, it is more difficult for particles to move in the longitudinal direction of the bar than in the transverse (or thickness) direction. However, further evidence is required to confirm this conjecture.

3.2. MICROSTRUCTURE

Figure 4 shows a typical microstructure of a printed Al$_2$O$_3$ test specimen for a cross-section perpendicular to the printing direction. The grains are equiaxed and small (<5 µm). Grain size was measured by the lineal intercept method. Twenty horizontal lines, with random distances relative to each other, were drawn on the image of microstructure. The length of the lines was equal to the width of the image and each line had 20-30 interceptions with grain boundaries. The grain size was estimated using the following equation.

$$D = 1.56 \frac{\sum l_i}{\sum n_i} \tag{1}$$

where D is the average grain size in μm, l_i is the length of each line in μm and n_i is the number of interceptions for each line. An average grain size of 2.1 μm was determined using this method.
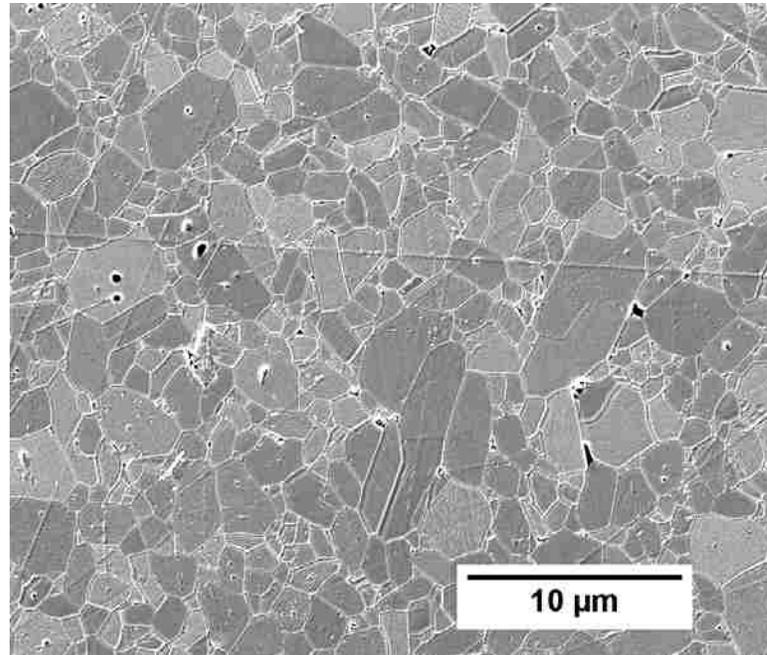
Figure 4. SEM image showing a typical microstructure of the Al_2O_3 produced via the CODE process.

3.3. MECHANICAL PROPERTIES

The cumulative distribution function for the Weibull distribution is:

$$P_f = 1 - \exp\left[-\left(\frac{\sigma_{max}}{\sigma_0}\right)^m\right] \tag{2}$$

where P_f is the probability of failure, σ_{max} is maximum tensile stress in a test specimen at failure, σ_0 is the Weibull characteristic strength (corresponding to a $P_f = 0.632$ or 63.2%), and m is Weibull modulus. The procedure in ASTM 1239 [16] was implemented in a Matlab script to fit the function on the raw data, find the Weibull parameters, and obtain the Weibull plot.

The readings of the deflectometer were plugged in Equation (3), which was obtained from Euler-Bernoulli beam theory (see e.g., [19] for an explanation of this theory), to calculate Young's modulus as follows:

$$E = \frac{11 P l^3}{768 I \delta} \tag{3}$$

where E is Young's modulus (N/m^2), P is the total load (N), l is the outer span of the fixture (m), I is the second moment of inertia of the test specimen cross-section about the neutral axis (m^4), and δ is the mid-span deflection (m). δ is measured by the deflectometer and P is measured by a load-cell. For a rectangular cross-section with four chamfered edges of size c, the adjusted moment of inertia is given in [15]:

$$I = \frac{b d^3}{12} - \frac{c^2}{9}\left(c^2 + \frac{(3d - 2c)^2}{2}\right) \tag{4}$$

where b and d are width and height of the bar (m), respectively, and c is the chamfer size (m).

The Weibull plot of the flexural strength data is shown in Figure 5. The Weibull characteristic strength was 385.3 MPa and the raw Weibull modulus was 8.33. According to ASTM 1239 [16], the unbiasing factor for the maximum likelihood estimate of the Weibull modulus when 24 specimens are used is 0.943. Thus, the unbiased Weibull modulus is 7.85. The average flexural strength was 364 MPa with a standard deviation of 50 MPa. Young's modulus was found to be 371±14 GPa. The average values of fracture toughness and hardness were 4.5±0.1 MPa•m$^{0.5}$ and 19.8±0.6 GPa, respectively. All of these values are in good agreement with available data in the literature for pressureless sintering of alumina produced by conventional methods (e.g., [20–22]). According to these references, a dense fine-grained alumina ceramic has a flexural strength of 300-500 MPa, a Young's modulus of 380-400 GPa, a fracture toughness of 3.5-5 MPa•m$^{0.5}$, and a Vickers hardness of ~20 GPa. Figure 6 shows typical fracture and indented surfaces from the specimens tested in this study.

The Griffith criterion was used to calculate the critical flaw size in each sample. Assuming the flaws are internal (based on observations discussed next), the size of flaws can be calculated using the following equation:

$$(5)$$

where $2c$ is the length of the flaw (m), K_{IC} is the fracture toughness (MPa•m$^{0.5}$), σ_f is the fracture stress (MPa), and Y is the stress intensity shape factor. σ_f is measured at the flaw location, which is assumed to be near the tensile surface. Y is equal to 1.77 and 1.13 for long flaws and round flaws, respectively, according to ASTM C1322 [23]. Thus, the estimated length of the flaw ($2c$) is 102±34 μm for long flaws and 252±84 μm for round flaws.
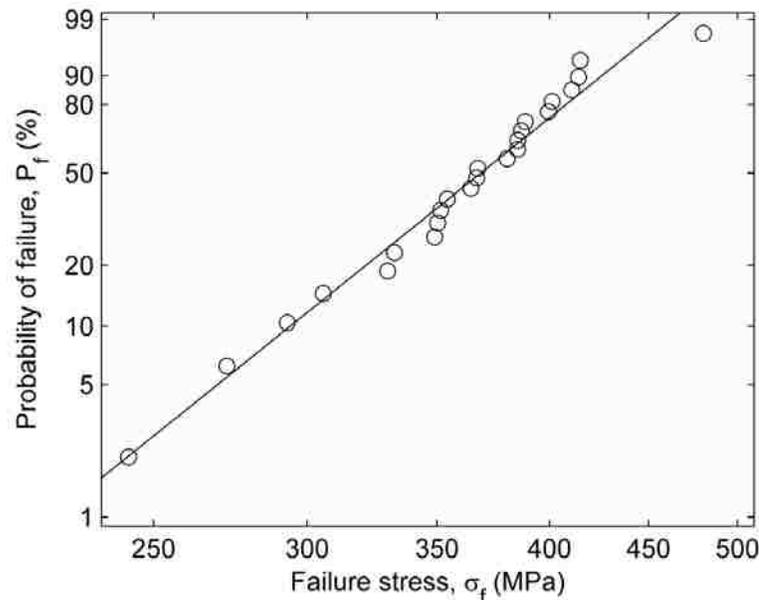
Figure 5. Weibull plot of the flexural strength data from Al$_2$O$_3$ test specimens.

Figure 7 shows a typical cross-section of printed samples using SEM at a low magnification. No printing flaws were observed in the images of the samples after fabrication. Figure 8 demonstrates two typical fracture origins believed to result from air bubbles or binder agglomerates in the paste. Most fracture surfaces revealed similar flaws near the tensile surface.

Available data in the literature for other additive manufacturing processes were collected for alumina to compare the results of this study with other AM processes. As stated in ASTM 1683 [24], the observed strength values of advanced ceramics are dependent on test specimen size, geometry and stress state. Thus, the procedure explained

in the ASTM standard was employed to convert the strength values reported in different sources to the strength of standard "B" bars ($3{\times}4{\times}45$ mm^3) in order to have a meaningful comparison. Other properties (e.g., modulus, hardness) are not size-dependent and thus the reported values were used in the comparison, even though different test methods and parameters may have affected the results to some extent.
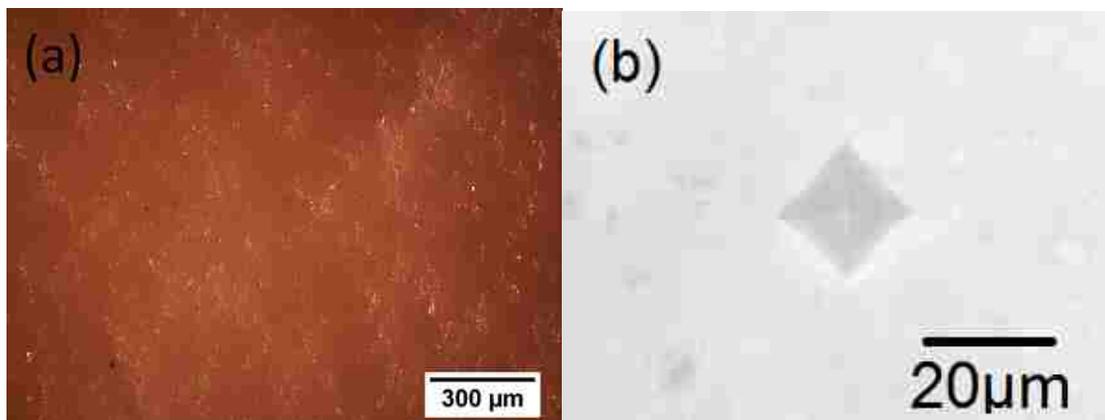
Figure 6. Typical fracture surface (a) and indented surface (b).

According to ASTM 1683 [24], Equations (6) and (7) can be used to obtain the Weibull material scale parameter from the mean flexural strength and vice versa. Equation (6) is for volume-origin flaws and Equation (7) is for surface-origin flaws (hence the subscripts V and A).

$$(\sigma_0)_V = \frac{\sigma_f \left[\left(\frac{K_i}{L_o} m_{V,sp} + 1\right)\left(\frac{1}{(m_{V,sp} + 1)^2}\right)V\right]^{1/m_{V,sp}}}{\Gamma\left(\frac{1}{m_{V,sp}} + 1\right)} \tag{6}$$

$$(\sigma_0)_A = \frac{\sigma_f \left\{K_{oi}\left(m_{A,sp} + 1\right) + b\left(\frac{K_i}{L_o} m_{A,sp} + 1\right)\left(\frac{1}{m_{A,sp} + 1}\right)\right\}^{1/m_{A,sp}}}{\Gamma\left(\frac{1}{m_{A,sp}} + 1\right)} \tag{7}$$

where σ_0 is the Weibull material scale parameter, σ_f is the mean strength measured in experiments, L_i and L_o are the lengths of inner and outer spans, respectively, m is the Weibull modulus, b and d are the width and height of sample, respectively, V is the gage volume ($b{\times}d{\times}L_o$), and Γ is the gamma function.
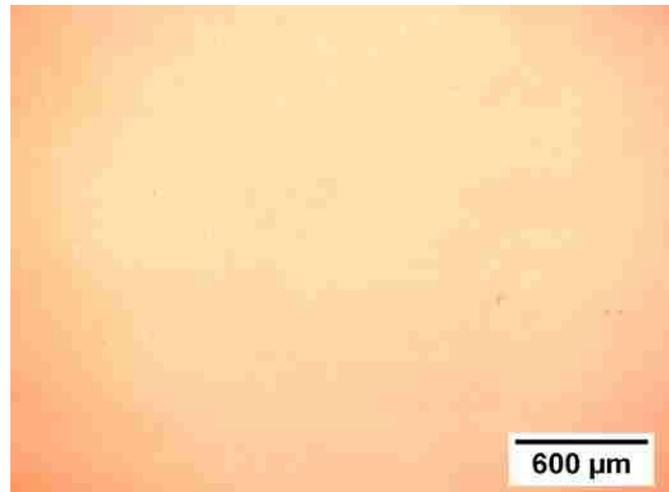
Figure 7. A typical cross-section under SEM showing a solid surface with no flaws.

As mentioned in the Introduction section, the mechanical properties of products of many AM processes of ceramics are poor and researchers often do not report the mechanical properties. However, there are some AM processes capable of producing dense ceramic parts with notable properties. For each of these processes, the highest values reported in the literature are collected and listed in Table 4 for comparison. These processes include Lithography-based Ceramic Manufacturing (LCM) [25], Selective Laser Sintering (SLS) [26], Robocasting (RC) [27], Freeze-form Extrusion Fabrication (FEF) [28,29], Three-Dimensional Printing (3DP) [30], and Binder Jetting (BJ) [31].

Figure 8. Two typical fracture origins near the tensile surface of the Al_2O_3 flexure test specimens.

It should be noted that in AM processes, the deposition orientation could affect the mechanical properties of the parts to some extent. For example, Huang et al. [29]

reported flexural strengths of 219 and 198 MPa for longitudinally printed and transversely printed samples, respectively. This effect is hypothesized to be small for CODE as no printing flaw was observed in the samples and no visible differences in cross-sections and microstructures of samples cut in different directions were identified. However, further evidence is required to confirm this hypothesis. Note that for other AM processes, the highest values reported in each reference are given in Table 4 for comparison.

Table 4 shows that the CODE process has a very good standing among AM processes in terms of mechanical properties. This is due to several facts including:

- fine alumina powder facilitating the sintering process,
- high solids loading paste resulting in a dense green body,
- printing at room temperature as opposed to high temperature or low temperature which may cause clogging of the nozzle as a result of paste drying or freezing,
- optimal partial drying during the printing process with the aid of an infrared lamp, which enables strong bonding between layers,
- uniform partial drying during the printing process with the aid of an oil bath surrounding the part, which precludes crack formation, warpage, and moisture/temperature gradient in the part,
- employing a new extrusion mechanism, which guarantees consistent flowrate and avoids pores in the part, and
- use of humid drying to remove water content after part fabrication which increases the green body density

Other advantages of the CODE process include low cost and simplicity of feedstock preparation, fabrication system and post-processing; potential for fabricating functionally graded materials via mixing two or more pastes of different materials at varying rates; capability of embedding sensors or other components during the fabrication process as demonstrated in [32]; and use of water as the liquid medium in the paste which facilities efficient post-processing and enables fabrication of large solid components (mainly because water can be more readily removed). However, the CODE process has two main limitations: 1) significant staircase effect; and 2) difficulty in fabricating fine features in complex parts. These limitations could be alleviated by

employing finer extrusion nozzles (up to ~150 μm diameter) which, on the other hand, would increase the fabrication time. Adaptive slicing [33] and adaptive rastering [34] techniques have been proposed to minimize the fabrication time when finer diameter nozzles are used.

Table 4. Mechanical properties of alumina parts produced by different additive manufacturing processes.

Process	Relative density (%)	Young's modulus (GPa)	Flexural strength (MPa)	Characteristic strength (MPa)	Weibull modulus	Fracture toughness (MPa•m$^{0.5}$)	Hardness (GPa)	2c (μm) assuming long flaws	2c (μm) assuming round flaws
CODE	98	371±14	364±50	385.3	8.3×0.943	4.5±0.1	19.8±0.6	102±34	252±84
LCM [25]	99	-	369*-383*	-	11.2×0.955	-	-	-	-
SLS [26]	88	-	255±17	-	-	-	-	-	-
RC** [27]	97	-	236*-248*	297	8.9×0.901	3.3±0.2	18.6±0.8	89	218
FEF** [28,29]	87-92	327±20	219	-	5.4×0.947	-	14.4±0.9	-	-
3DP **,† [30]	85	-	62	-	-	-	-	-	-
BJ** [31]	-	54±14.5	Very low‡	-	-	-	1.5±0.01	-	-

* Original value converted to standard "B" bar using equations (6) and (7) for fair comparison.
** Highest values in the paper are reported here.
† Vacuum infiltration was used to enhance the mechanical properties.
‡ The compressive strength was only 132 MPa, so the flexural strength was minimal.

4. CONCLUSIONS

Properties of advanced ceramic parts produced by a novel additive manufacturing process called the Ceramic On-Demand Extrusion (CODE) process have been characterized extensively in this paper. Thirty Al_2O_3 test bars were fabricated using the CODE process to examine the properties of the produced parts after sintering. The specimens had a relative density of 98%, a Young's modulus of 371±14 GPa, an unbiased Weibull modulus of 7.85, an average flexural strength of 364±50 MPa, a fracture toughness of 4.5±0.1 MPa•m$^{0.5}$, and a hardness of 19.8±0.6 GPa. These properties surpass those produced by most other additive manufacturing processes and match those produced by conventional fabrication techniques. This indicates the high potential of the CODE process to be employed in industrial applications, especially

where one-of-a-kind parts or a small number of customizable products with good mechanical properties are needed.

ACKNOWLEDGEMENTS

REFERENCES

[1]   Griffin EA, McMillin S. Selective laser sintering and fused deposition modeling processes for functional ceramic parts. In: *Solid Freeform Fabrication Symposium*. Austin, TX, USA; 1995:25-30.

[2]   Griffith ML, Halloran JW. Freeform fabrication of ceramics via stereolithography. *J Am Ceram Soc*. 1996;79(10):2601-2608.

[3]   Grau J, Moon J, Uhland S, Cima MJ, Sachs E. High green density ceramic components fabricated by the slurry-based 3DP process. In: *Solid Freeform Fabrication Symposium*. Austin, TX, USA; 1997:371-378.

[4]   Noguera R, Lejeune M, Chartier T. 3D fine scale ceramic components formed by ink-jet prototyping process. *J Eur Ceram Soc*. 2005;25(12):2055-2059. doi:10.1016/j.jeurceramsoc.2005.03.223.

[5]   Griffin C, Daufenbach J, McMillin S. Desktop manufacturing: LOM vs pressing. *Am Ceram Soc Bull*. 1994;73(8):109-113.

[6]   Danforth SC. Fused deposition of ceramics: a new technique for the rapid fabrication of ceramic components. *Mater Technol*. 1995;10(7-8):144-146.

[7]   Stuffle K, Mulligan A, Calvert P, Lombardi J. Solid freebody forming of ceramics from polymerizable slurry. In: *Solid Freeform Fabrication Symposium*. Austin, TX, USA; 1993:60-63.

[8]   Cesarano III J, Segalmen R, Calvert P. Robocasting provides moldless fabrication from slurry deposition. *Ceram Ind*. 1998;148:94-102.

[9]   Huang T, Mason MS, Hilmas GE, Leu MC. Freeze-form extrusion fabrication of ceramics. In: *Solid Freeform Fabrication Symposium*. Austin, TX, USA; 2005:73-85.

[10]   Travitzky N, Bonet A, Dermeik B, et al. Additive manufacturing of ceramic-based materials. *Adv Eng Mater*. 2014;16(6):729-754. doi:10.1002/adem.201400097.

[11]   Chen F, Cao F, Pan H, et al. Mechanical and dielectric properties of silicon nitride ceramics with high and hierarchical porosity. *Mater Des*. 2012;40:562-566. doi:10.1016/j.matdes.2012.03.026.

[12]   Zocca A, Colombo P, Gomes CM, Günster J. Additive manufacturing of ceramics: issues, potentialities, and opportunities. *J Am Ceram Soc*. 2015;98(7):1983-2001. doi:10.1111/jace.13700.

[13]   Ghazanfari A, Li W, Leu MC, Hilmas GE. A novel extrusion-based additive manufacturing process for ceramic parts. In: Bourell DL, Crawford RH, Seepersad CC, Beaman JJ, Fish S, Marcus H, eds. *Solid Freeform Fabrication Symposium*. Austin, TX, USA; 2016:1509-1529.

[14]   Zomorodi H, Landers RG. Extrusion based additive manufacturing using explicit model predictive control. In: *American Control Conference*. Boston, MA, USA; 2016:1747-1752.

[15]   ASTM C1161. *Standard Test Method for Flexural Strength of Advanced Ceramics at Ambient Temperatures*. West Conshohocken, PA, USA; 2013. doi:10.1520/C1161-13.

[16]   ASTM C1239. *Standard Practice for Reporting Uniaxial Strength Data and Estimating Weibull Distribution Parameters for Advanced Ceramics*. West Conshohocken, PA, USA; 2013. doi:10.1520/C1239-13.

[17]   ASTM C1421. *Standard Test Methods for Determination of Fracture Toughness of Advanced Ceramics*. West Conshohocken, PA, USA; 2010. doi:10.1520/C1421-10.

[18]   ASTM C1327. *Standard Test Method for Vickers Indentation Hardness of Advanced Ceramics*. West Conshohocken, PA, USA; 2015. doi:10.1520/C1327-15.

[19]   Sadd MH. *Elasticity: Theory, Applications, and Numerics*. second edi. Burlington, MA, USA: Elsevier; 2009.

[20]   Boch P, Niepce JC, eds. *Ceramic Materials: Processes, Properties and Applications*. 1st ed. Newport Beach, CA, USA: ISTE USA; 2007.

[21]   Brook RJ, ed. *Concise Encyclopedia of Advanced Ceramic Materials*. 1st ed. Elmsford, NY, USA: Pergamon Press; 1991.

[22]   Auerkari P. *Mechanical and Physical Properties of Engineering Alumina Ceramics*. Vol 1792. Vuorimiehentie, Finland; 1996.

[23] ASTM C1322. *Standard Practice for Fractography and Characterization of Fracture Origins in Advanced Ceramics*. West Conshohocken, PA, USA; 2010. doi:10.1520/C1322-05BR10.

[24] ASTM C1683. *Standard Practice for Size Scaling of Tensile Strengths Using Weibull Statistics for Advanced Ceramics*. West Conshohocken, PA, USA; 2015. doi:10.1520/C1683-10R15.

[25] Schwentenwein M, Homa J. Additive manufacturing of dense alumina ceramics. *Int J Appl Ceram Technol*. 2015;12(1):1-7. doi:10.1111/ijac.12319.

[26] Liu ZH, Nolte JJ, Packard JI, Hilmas G, Dogan F, Leu MC. Selective laser sintering of high-density alumina ceramic parts. In: Hinduja S, Fan K-C, eds. *Proceedings of the 35th International MATADOR Conference*. Vol 3. Taipei, Taiwan: Springer; 2007:351-354. doi:10.1007/978-1-84628-988-0_79.

[27] Feilden E, Blanca EG-T, Giuliani F, Saiz E, Vandeperre L. Robocasting of structural ceramic parts with hydrogel inks. *J Eur Ceram Soc*. 2016;36(10):2525-2533. doi:10.1016/j.jeurceramsoc.2016.03.001.

[28] Li J, Leu MC, Hilmas GE. Effects of temperature on aqueous freeform extrusion fabrication. In: Bourell D, Beaman J, Crawford R, Fish S, Marcus H, Seepersad C, eds. *Solid Freeform Fabrication Symposium*. Austin, TX, USA; 2015:319-331.

[29] Huang T, Mason MS, Zhao X, Hilmas GE, Leu MC. Aqueous-based freeze-form extrusion fabrication of alumina components. *Rapid Prototyp J*. 2009;15(2):88-95.

[30] Maleksaeedi S, Eng H, Wiria FE, Ha TMH, He Z. Property enhancement of 3D-printed alumina ceramics using vacuum infiltration. *J Mater Process Technol*. 2014;214(7):1301-1306. doi:10.1016/j.jmatprotec.2014.01.019.

[31] Gonzalez JA, Mireles J, Lin Y, Wicker RB. Characterization of ceramic components fabricated using binder jetting additive manufacturing technology. *Ceram Int*. 2016;42(9):1-7. doi:10.1016/j.ceramint.2016.03.079.

[32] Ghazanfari A, Li W, Leu MC, Zhuang Y, Huang J. Advanced ceramic components with embedded sapphire optical fiber sensors for high temperature applications. *Mater Des*. 2016;112:197-206. doi:10.1016/j.matdes.2016.09.074.

[33] Dolenc A, Makela I. Slicing procedures for layered manufacturing techniques. *Comput Des*. 1994;26(2):119–126.

[34] Ghazanfari A, Li W, Leu MC. Adaptive rastering algorithm for freeform extrusion fabrication processes. *Virtual Phys Prototyp*. 2015;10(3):163-172. doi:10.1080/17452759.2015.1096798.

III. ADDITIVE MANUFACTURING AND MECHANICAL CHARACTERIZATION OF HIGH DENSITY FULLY STABILIZED ZIRCONIA[1]

ABSTRACT

Mechanical properties of additively manufactured 8 mol% yttria-stabilized zirconia (8YSZ) parts were extensively studied for the first time. A novel freeform extrusion fabrication process, called Ceramic On-Demand Extrusion (CODE), was employed to deposit an aqueous viscous suspension (~50 vol% solids loading) of fully stabilized zirconia powder in a layer-by-layer fashion. Each layer was exposed to infrared radiation after deposition to attain partial solidification due to drying. Before exposure, the layer was surrounded by oil to preclude non-uniform evaporation, which could cause warpage and crack formation. After the fabrication process was completed, the parts were humid-dried in an environmental chamber and densified by sintering under atmospheric pressure. Standard test methods were employed to examine the properties of sintered parts including density, Vickers hardness, fracture toughness, Young's modulus, and flexural strength. Microstructural evaluation was also performed to observe the microstructural morphology and measure grain size. The results indicate that the properties of 8YSZ parts produced by the CODE process match those obtained by conventional fabrication techniques.

1. INTRODUCTION

Fully stabilized cubic zirconia has several desirable properties including high ionic conductivity, thermal and chemical stability, and mechanical strength [1]. The combination of these properties makes this material attractive for use as electrolytes in Solid Oxide Fuel Cells (SOFCs), oxygen sensors, oxygen separators and electrochemical reactors [2]. A geometrically complex design for an electrolyte can increase the efficiency of an SOFC by increasing the surface area between the cathode and the electrolyte [3]. It can also increase the load-bearing capacity, which is a critical factor for fuel cell stacks [4]. Several researchers have designed and fabricated structured

electrolytes or support structures for SOFCs using various manufacturing techniques, as explained below.

Beeaff and Hilmas [5] used an extrusion technique to fabricate a honeycomb of zirconia laminated to a planar electrolyte in order to increase the strength of the SOFC. Ding and Liu [6] fabricated cone-shaped tubular segmented-in-series SOFC stacks using slip casting and deposited yttria-stabilized zirconia films onto the anode tubes by dip coating. Their results showed good thermo-mechanical properties and enhanced performance for the fuel cell. Yamaguchi et al. [7] fabricated a cathode-supported honeycomb SOFC via extrusion of a monolith and used a slurry injection method for the channel surface coating in order to increase the volumetric power density. Ruiz-Morales et al. [8] fabricated a honeycomb electrolyte to reduce the electrolyte thickness and increase the structure's mechanical strength. Their results showed an improvement in volumetric power density and material usage. Rajeswari et al. [9] made structured electrolytes by thermally induced gelation of an aqueous zirconia slurry containing methylcellulose using microwave irradiation. Celik et al. [10] produced tapes of 3 mol% and 8 mol% yttria-stabilized zirconia using tape casting and laser-cut triangular patterns in some of the tapes. They employed cold isostatic pressing to sandwich solid layers between patterned layers and realized a new design. Their results indicated an enhancement in the performance of the fuel cells.

Although the above researchers were able to successfully fabricate parts with complex geometries using conventional manufacturing processes, Additive Manufacturing (AM) has a prominent advantage in fabricating complex parts with delicate geometrical features. Several studies have been conducted to exploit this advantage in fabricating parts from 8 mol% yttria-stabilized zirconia for SOFCs and other applications. Sukeshini et al. [11] used inkjet printing to fabricate electrolytes, as well as electrodes, for SOFCs. Their cells exhibited a maximum power density of 430 to 460 mW/cm^2 at 850 °C using hydrogen as the fuel source. Kirihara [12] built dendritic structures with geometrically ordered lattices using micro-patterning stereolithography with optimized process parameters, dewaxing, and sintering to achieve higher density. Tomov et al. [13] used direct inkjet printing and optimized the printing parameters to

improve the surface quality of their parts. Manogharan et al. [14] employed binder jetting to fabricate parts. However, they were not able to fabricate dense components.

Although mechanical properties are of prime importance in many applications, to the authors' knowledge, there is no paper in the literature reporting the mechanical properties of additively manufactured, fully stabilized zirconia parts. In fact, AM of monolithic ceramics, which enables the components to match the physical and chemical properties of their conventionally manufactured counterparts, is still a challenge and remains the most important task that needs to be solved in order to promote AM of ceramics to more than a niche technology [15].

In the current study, a novel extrusion-based AM process, called Ceramic On-Demand Extrusion (CODE), is used to produce 8 mol% yttria-stabilized cubic zirconia parts. In this freeform fabrication process, aqueous suspensions of ceramic particles were prepared and extruded in a layer-by-layer fashion followed by uniform radiation drying between successive layers with a liquid surrounding the part. Density, hardness, fracture toughness, strength, stiffness and microstructure of fully stabilized zirconia parts were examined and compared to the properties of fully stabilized zirconia fabricated using traditional manufacturing methods.

2. MATERIALS AND METHODS

2.1. FEEDSTOCK PREPARATION

The feedstock of the CODE process is an extrudable, viscous colloid prepared by dispersing ceramic particles in an aqueous solution. This suspension is referred to as paste throughout this paper. The zirconia paste was made of a commercially available 8 mol% yttria-stabilized zirconia (8YSZ) powder (TZ-8YS, Tosoh Corp., Grove City, OH, USA), deionized water, dispersant (Dolapix CE 64, Zschimmer & Schwarz GmbH, Lahnstein, Germany), and 30% NH_3-basis ammonium hydroxide solution (221228, Sigma Aldrich, St. Louis, MO, USA) for pH adjustment. The zirconia powder had a specific surface area of 7 m^2/g and an average particle size of 52 nm according to the manufacturer.

A nominally 50 vol% solids loading paste was prepared by dispersing zirconia powder in water using 7.1 mg dispersant per square meter of surface area of zirconia

powder and adjusting the pH to ~9, as measured by a pH meter (HI 2210, Hannah Instruments, Woonsocket, RI, USA). A vacuum mixer (Model F, Whip Mix, Louisville, KY, USA) was employed to mix the paste homogeneously without introducing air bubbles. Finally, a vibratory table (Syntron Material Handling, Saltillo, MS, USA) was used to remove any remaining air bubbles.

2.2. FABRICATION PROCESS

The CODE process is a freeform extrusion fabrication technique capable of making complex parts with near theoretical density (>98%). Ghazanfari et al. [16] introduced this process and employed it to produce several sample parts for various applications.

In the current study, eighteen "small blocks" (as-printed size: $25 \times 6 \times 4$ mm^3 in length, width, and height, respectively) and six "large blocks" (as-printed size: $60 \times 54 \times 7.5$ mm^3 in length, width, and height, respectively) were fabricated using the CODE process to examine the properties of the produced parts. Ceramic pastes were extruded through a circular nozzle that is mounted on a workhead attached to a gantry, which traversed in the X, Y and Z directions through G & M code commands (i.e., G & M codes are a set of letters and numbers used to program the movements and other actions (tool change, end of program, etc.) of a CNC machine). The extrudate was deposited on a substrate located in a tank designed to hold a fluid medium (i.e., mineral oil). Once the deposition of each layer was completed, a liquid feeding subsystem pumped oil (Florasense Lamp Oil, MVP Group International Inc., Charleston, SC, USA) into the tank, surrounding the deposited layer, to preclude undesirable evaporation of water from the sides of the deposited layers. The level of the oil was controlled so that it reached just below the top surface of the part being fabricated. Infrared radiation was then used to uniformly dry the deposited layer so that the part being fabricated could maintain its shape when the next layers were being deposited as the part was being built. The parts were fabricated in a layer-by-layer fashion by repeating the layer deposition followed by radiation drying with a liquid surrounding the already deposited layers. Figure 1 shows a large block in the green state after the fabrication process. The process

parameters used to print all the parts are given in Table 1. The processing time was ~6 min for each small block, and ~65 min for each large block.
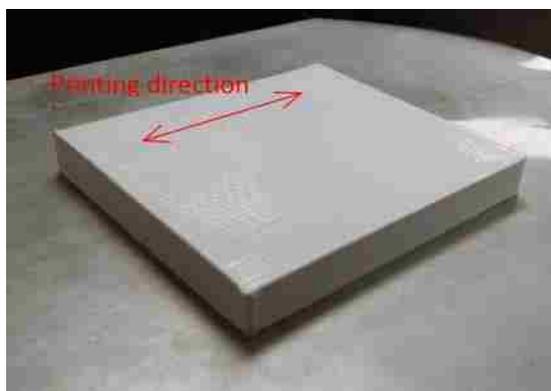
Figure 1. A sample block ($60\times54\times7.5$ mm^3) after fabrication using the CODE process.

Table 1. Printing parameters used in the CODE process to fabricate fully stabilized zirconia test blocks.

Nozzle diameter (μm)	610
Nozzle travel speed (mm/s)	30
Layer thickness (μm)	400
Number of layers	19
Line spacing (μm)	600
Number of lines in a layer	90
Lamp distance (m)	0.25
Radiation time (s)	30

2.3. DRYING AND SINTERING

After the fabrication process was completed, the samples were removed from the oil bath and their remaining water was eliminated using humid-drying. An environmental chamber (LH-1.5, Associated Environmental Systems, Ayer, MA, USA) was employed to control the temperature and humidity during the drying process at 25 °C and 75% relative humidity. This condition prevented warping and the formation of cracks during the drying process.

The dried parts were then sintered in an electric furnace (Deltech Inc., Denver, CO, USA). To determine the optimal sintering conditions, the eighteen small blocks were divided into six groups and sintered under six different conditions as discussed in Section 3.1. Based on a comparison of the properties of these six groups, two sintering conditions were chosen to sinter the six large blocks and study their properties.

2.4. CHARACTERIZATION

Archimedes' technique was performed to measure the density of the printed parts after sintering. After the dry mass was recorded, samples were saturated by submersion in distilled water under vacuum for ~12 h. The saturated and suspended masses were then measured to calculate the bulk density. This value was divided by the theoretical density of 8YSZ (5.97 g/cm^3 [17]) to find the average relative density of the samples. The size of the blocks was measured after printing, drying, and sintering to calculate the amount of shrinkage during the bulk drying and sintering processes.

Microstructural images were obtained using Scanning Electron Microscopy (SEM) from sections of the sintered test blocks. Specimens were polished to a 0.25 μm diamond finish using successively finer diamond abrasives. Thermal etching was then used to reveal the grain boundaries by placing the polished specimens in an electric furnace (Deltech Inc., Denver, CO, USA) at 1350 °C for 30 min with a heating/cooling rate of 10 °C/min. A scanning electron microscope (Helios Nanolab 600, FEI, Hillsboro, OR, USA) was employed to observe the specimens.

Vickers indentation test was carried out according to ASTM C1327 [18] using a microhardness tester (Duramin 5; Struers, Cleveland, OH, USA) to measure the hardness. The samples were polished to a 0.25 μm diamond finish using successively finer diamond abrasives. Hardness was calculated from 4 to 6 indents per sample. The indenter was pressed against the samples with a force of 4.91 N for 10 s. The indentation size was measured using an optical microscope with a 40X lens.

Fracture toughness was measured at room temperature by two methods. For the small blocks, it was estimated from the hardness tests by measuring the length of cracks extending from the corners of the Vickers indent as discussed in Section 3.1. For the large blocks, it was measured using chevron-notched beam specimens in four-point bending using a fully articulating test fixture for configuration A (L=50 mm, B=3 mm, W=4 mm, and a$_0$=0.8 mm) according to ASTM C1421 [19]. Eight test bars were ground to standard size for each group using a fully automated surface grinder (Chevalier, FSG-3A818, Santa Fe Springs, CA, USA). The chevron notches were machined using a dicing saw (Accu-cut 5200, Aremco Products, Ossining, NY, USA) with a 0.15 mm-thick diamond wafering blade. The same fixture and load frame used for flexural tests were

employed to break the chevron-notched beams with a crosshead speed of 0.015 mm/min. The notch dimensions were then measured using an optical microscope (KH-3000, Hirox, Hackensack, NJ, USA).

Four-point bending tests were performed at room temperature according to ASTM C1161 [20] to measure flexural strengths. The same surface grinder employed for chevron-notched beam specimens was used to machine the specimens to standard "B" bars ($3\times4\times45$ mm^3). All the surfaces of the bars were machined with a 600-grit diamond abrasive wheel. The bars were then manually chamfered using a 1200-grit metal-bond diamond grinding disk. Flexural strengths were measured using a fully articulating B-bar fixture with an outer span of 40 mm and an inner span of 20 mm in a screw-driven instrumented load frame (5881; Instron, Norwood, MA, USA). The crosshead speed was 0.5 mm/min. Young's modulus was determined using a deflectometer (a linear variable differential transformer) measuring the deflection of the center of the test bar during strength testing (deflectometer's data was recorded from the beginning of each test until the failure of the specimen).

3. RESULTS AND DISCUSSION

3.1. SINTERING STUDY

The 18 small blocks were sintered under 6 different conditions as given in Table 2. Their properties were evaluated in order to choose the best sintering condition for the large blocks. Their relative density was measured to be 99±0.2% regardless of their sintering conditions. Thus, they were judged based on hardness and fracture toughness. The values of hardness are given in Table 2 for each group. Groups 3 and 6 had the highest hardness values (15.3±0.4 GPa and 15.4±0.2 GPa, respectively). To compare the fracture toughness, the equation proposed by Liang et al. [21] was chosen due to its popularity for zirconia [22–32]. According to their method, the value of fracture toughness is estimated from the following equation:

$$\left(\frac{K_{IC}}{Ha\varphi^{0.5}}\right)\left(\frac{H}{E\varphi}\right)^{0.4} = 0.129\left(\frac{c}{a}\right)^{-1.5\left(\frac{c}{a}\right)^{-0.5+0.25\log\left(\frac{c}{a}\right)}} \tag{8}$$

where K_{IC} is the fracture toughness in MPa•m$^{0.5}$, H is the hardness in MPa, E is the Young's modulus in MPa, φ is a constant equal to 3, and a and c are the half diagonal

length of the indent and half length of the crack in m, respectively. α is obtained from Equation (2):

$$\alpha = 14 \left[1 - 8 \left(\frac{4\nu - 0.5}{1 + \nu} \right)^4 \right] \qquad (9)$$

where ν is Poisson's ratio which was assumed to be 0.29 [22–32].

Table 2. Schedules used in the sintering study and the corresponding hardness and toughness.

Group	Sintering condition				Vickers hardness (GPa)	Indentation fracture toughness (MPa•m$^{0.5}$)
	Heating rate (°C/min)	Sintering temperature (°C)	Hold time (h)	Cooling rate (°C/min)		
1	5	1500	1	2	14.3±0.3	3.37±0.09
2	5	1500	1.5	2	14.5±0.2	3.62±0.17
3	5	1500	2.5	10	15.3±0.4	3.02±0.24
4	5	1550	0.5	2	14.5±0.2	3.61±0.08
5	5	1550	0.8	10	14.3±0.1	3.50±0.16
6	5	1600	0.5	10	15.4±0.2	2.95±0.11

The values of fracture toughness are given in Table 2 for each group. An indented sample is shown in Figure 2. Groups 2 and 4 had the highest toughness values (3.62±0.17 MPa•m$^{0.5}$ and 3.61±0.08 MPa•m$^{0.5}$, respectively). Accordingly, the sintering schedules of Groups 3 and 4 were chosen, based on a combination of hardness and fracture toughness, to sinter the large blocks. It is noted that Groups 2 and 4 had almost identical properties and Group 4 was chosen only because it had a different sintering temperature from Group 3. Three of the large blocks were sintered with the same sintering schedule as Group 3, and the other three were sintered with the same conditions as Group 4.

Figure 3 shows representative microstructures of specimens from Groups 3, 4, and 6. The grains were equiaxed, intergranular porosity was not observed, and intragranular pores were small (<1 μm). Grain size was measured by the lineal intercept method. Twenty horizontal lines, with random distances relative to each other, were constructed on the image of microstructure. The length of the lines was equal to the width of the image and each line had 20 to 30 interceptions with grain boundaries. The grain size was estimated using the following equation.

$$D = 1.56 \frac{\sum_i l_i}{\sum_i m_i} \tag{10}$$

where D is the average grain size in μm, l_i is the length of each line in μm, and n_i is the number of interceptions for each line. An average grain size of 5.1, 6.1, and 7.3 μm was determined using this method for Group 3, 4, and 6, respectively.
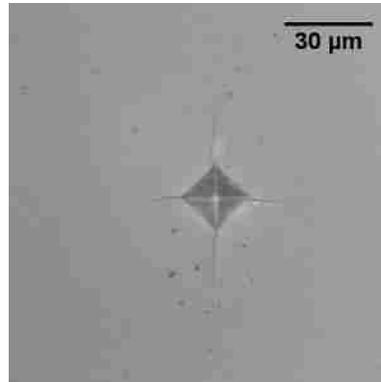
Figure 2. An indented sample used to measure hardness and indentation fracture toughness.
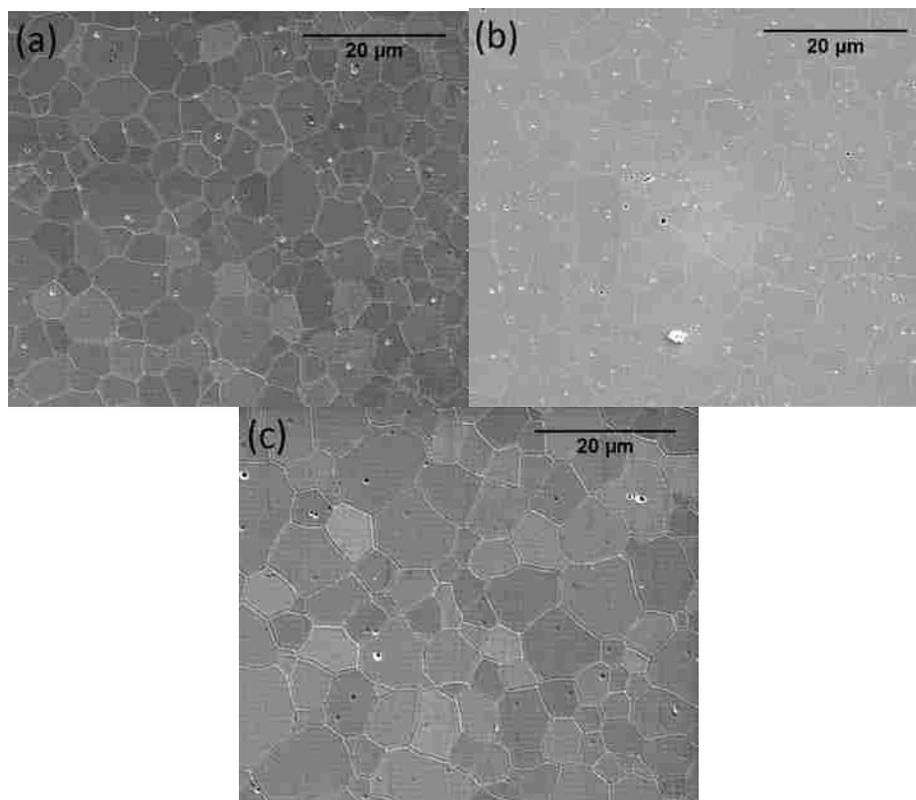
Figure 3. SEM images showing representative microstructures of fully stabilized zirconia parts produced using the CODE process: (a) Group 3, (b) Group 4, and (c) Group 6.

3.2. SHRINKAGE

The size of the large blocks reduced to $58.5 \times 53.2 \times 7.3$ mm^3 after drying, showing 2.5%, 1.5% and 2.7% reduction in length, width and height, respectively. This indicates a volumetric shrinkage of 6.5%. The dimensions of the bars were $46.8 \times 42.6 \times 5.7$ mm^3 after sintering, showing 22.0%, 21.1% and 24.0% reduction in length, width and height, respectively, compared to the wet (as-printed) samples. This indicates a volumetric shrinkage of 53.2% compared to wet samples. The slightly lower shrinkage percentage in the length and width directions, during drying and sintering, is hypothesized to be caused by friction between specimen and substrates, which hinders shrinkage; i.e. due to friction, it is more difficult for particles to move in the longitudinal and transverse directions of the parts than the thickness direction. However, further evidence is required to confirm this conjecture. The amounts of shrinkage during each step are given in Table 3.

Table 3. Amount of shrinkage of large blocks at each stage.

	Size (mm)	Linear shrinkage (%)	Volumetric shrinkage (%)
As-printed	$60 \times 54 \times 7.5$	-	-
Dried	$58.5 \times 53.2 \times 7.3$	$2.5 \times 1.5 \times 2.7$	6.5
Sintered	$46.8 \times 42.6 \times 5.7$	$22.0 \times 21.1 \times 24.0$	53.2

3.3. PROPERTIES

To calculate Young's modulus, Equation (4), which was obtained from Euler-Bernoulli beam theory (see e.g. [33] for an explanation of this theory), was used.

$$E = \frac{Pl^3}{48 I \delta} \tag{11}$$

where E is Young's modulus (N/m^2), P is the total load measured by a load cell (N), l is the outer span of the fixture (m), I is the second moment of inertia of the test specimen's cross-section about the neutral axis (m^4), and δ is the mid-span deflection measured by the deflectometer (m). For a rectangular cross-section with four chamfered edges of size c, the adjusted moment of inertia is given in [20]:

$$I = \frac{bd^3}{12} - c^2 \left[c^2 + \frac{(3d - 2c)^2}{3} \right] \tag{12}$$

where *b* and *d* are width and height of the bar (m), respectively, and *c* is the chamfer size (m). Based on this calculation, Young's modulus of Group 3 and 4 specimens were 195±8 and 208±6 GPa, respectively. This is in agreement with reported values in the literature ranging from 190 to 205 GPa [8,31,34,35].

The hardness values measured were 15.3±0.4 and 14.5±0.2 GPa for Group 3 and 4, respectively. These values are given in Table 4 along with values found in the literature for material produced by cold isostatic pressing and sintered. The hardness of parts produced by the CODE process are close to the upper limit of the data range found in the literature for 8YSZ (11 to 16 GPa) [31,36–39].

In the literature, the fracture toughness of 8YSZ ceramics has commonly been measured based on indentation tests, which is not an ASTM standard method and may result in large errors. As an example, Kibsey et al. [27] reported that, for the same sample, the predicted value of fracture toughness obtained from seven common equations varied between 2.3 and 13.5 MPa•m$^{0.5}$. Quinn and Bradt [40] also recommended that the indentation fracture toughness technique no longer be acceptable for ceramic materials. For 8YSZ, the reported data were in the range of 1.3 to 5.1 MPa•m$^{0.5}$ [31,36,38,39] as given in Table 4. This large variation is due to different equations used to estimate the fracture toughness based on indentation data, not because of the variations in material properties. Therefore, it is not possible to make a fair comparison between different groups. Nevertheless, if the same equation is used to estimate the fracture toughness for two sets of samples, the result is acceptable to make a comparison.

In addition to indentation fracture tests, the results of the chevron notch method are also given in Table 4. Based on this standard method, Group 3 and 4 had a fracture toughness of 2.1±0.1 and 2.5±0.1 MPa•m$^{0.5}$, respectively (compare with 3.02±0.24 and 3.61±0.08 MPa•m$^{0.5}$ estimated by indentation technique for Group 3 and 4, respectively). It should be noted that for 8YSZ samples, it was difficult to initiate a stable crack from the tip of the chevron notch even after a slow crosshead speed and a compression-compression fatiguing procedure was used as suggested by ASTM C1421. Only three specimens experienced a stable crack growth in each group and the fracture toughness was calculated based on these specimens (i.e., data from unstable cracks were discarded).

Table 4. Mechanical properties of 8YSZ produced via CODE and traditional techniques.

Process	Flexural strength (MPa)	Hardness (GPa)	Fracture toughness[*] (MPa•m$^{0.5}$)	Indentation fracture toughness (MPa•m$^{0.5}$)
CODE (Group 3)	232±55[**]	15.3±0.4	2.1±0.1	3.02±0.24
CODE (Group 4)	278±59[**]	14.5±0.2	2.5±0.1	3.61±0.08
CIP[†] [31]	-	11±0.9	-	5.1±1.1
CIP[†][36]	275[‡]	13	-	1.5±0.03
CIP[†] [38]	262±27[**]	11.9±0.4	-	1.3±0.1
CIP[†] [39]	-	13.5±0.2	-	3.16±0.06
CIP[†] and microwave sintering [39]	-	13.7±0.2	-	3.17±0.10

[*] From chevron-notched beam
[**] Four-point bending test of standard "B" bars according to ASTM C1161
[†] Cold Isostatic Pressing
[‡] Three-point bending test with a span of 30 mm and cross-section of 3×4 mm^2

The average flexural strengths were 232±55 and 278±59 MPa for Group 3 and 4, respectively. The test data are shown in Figure 4. For brittle materials, the measured value of strength greatly depends on test methodology and it is not fair to make a direct comparison between reported values from different sources if the test methodologies are not the same. For example, An et al. [34] cut square plates and round disks of two different diameters from identical plates made of zirconia and used three standard test methods to evaluate their strength. They reported strengths of 139, 483, and 894 MPa for the tensile, pressure-on-ring, and ball-on-ring tests, respectively. The only way to compare the results of different tests is to convert the data as explained in ASTM 1683 [41]. This method requires all the dimensions of samples and test fixture as well as Weibull modulus. Unfortunately, these values are not reported for 8YSZ in most papers and it is not possible to convert their data to those of four-point bending test. Accordingly, the flexural strength of samples in the current study was only compared to available data in literature for four-point bending tests of 8YSZ (typically 250 to 330 MPa [2,42–45]).

Detailed discussions about advantages, disadvantages, applications, fabrication of geometrically complex parts and properties of other materials produced via CODE process can be found elsewhere [16,46–48].
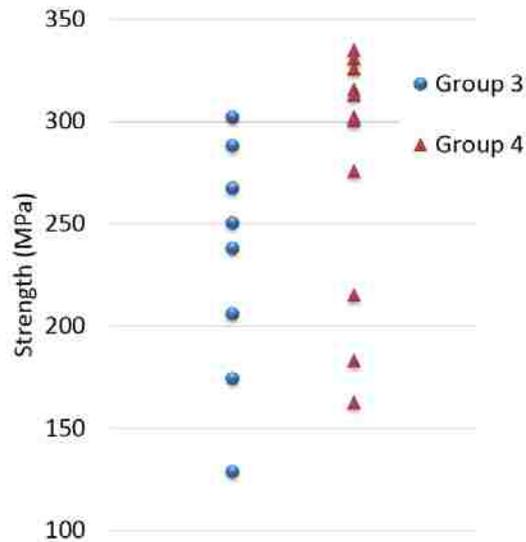
Figure 4. Flexural test data for Group 3 and 4 (the average values are 232 and 278 MPa, respectively).

4. CONCLUSIONS

A novel freeform extrusion fabrication process was employed to produce highly dense (with a relative density of >99%) parts from 8 mol% yttria-stabilized zirconia. Properties of these parts were studied using standard test methods and compared to those from other processes. Six sintering schedules were examined and two of them were chosen, based on their hardness and indentation fracture toughness, to produce final parts. The first group of final parts had a hardness of 15.3±0.4 GPa and an average flexural strength of 232±55 MPa, while the second group had a hardness of 14.5±0.2 GPa and an average flexural strength of 278±59 MPa.

To the authors' knowledge, other additive manufacturing processes have not been able to produce near theoretically dense, high strength parts or test bars from fully stabilized zirconia. Therefore, the results of this study were compared to traditional fabrication methods. All the properties including density, strength, hardness, fracture toughness, and Young's modulus matched the data found in literature for fabrication of fully stabilized zirconia using conventional techniques.

ACKNOWLEDGEMENTS

REFERENCES

[1]   P. Boch, J.C. Niepce, eds., Ceramic materials: processes, properties and applications, 1st ed., ISTE USA, Newport Beach, CA, USA, 2007.

[2]   S.P.S. Badwal, F.T. Ciacchi, V. Zelizko, The effect of alumina addition on the conductivity, microstructure and mechanical strength of zirconia - yttria electrolytes, Ionics (Kiel). 4 (1998) 25–32. doi:10.1007/BF02375776.

[3]   W. Winkler, The influence of the mass transfer on the geometric design of SOFC stacks, J. Power Sources. 86 (2000) 449–454. doi:10.1016/S0378-7753(99)00452-8.

[4]   F. Fleischhauer, R. Bermejo, R. Danzer, A. Mai, T. Graule, J. Kuebler, Strength of an electrolyte supported solid oxide fuel cell, J. Power Sources. 297 (2015) 158–167. doi:10.1016/j.jpowsour.2015.07.075.

[5]   D. Beeaff, G. Hilmas, Electrode support structures for planar solid oxide fuel cells, Key Eng. Mater. 264 (2004) 747–750. doi:10.4028/www.scientific.net/KEM.264-268.747.

[6]   J. Ding, J. Liu, A novel design and performance of cone-shaped tubular anode-supported segmented-in-series solid oxide fuel cell stack, J. Power Sources. 193 (2009) 769–773. doi:10.1016/j.jpowsour.2009.04.049.

[7]   T. Yamaguchi, S. Shimizu, T. Suzuki, Y. Fujishiro, M. Awano, Design and fabrication of a novel electrode-supported honeycomb SOFC, J. Am. Ceram. Soc. 92 (2009) 107–111. doi:10.1111/j.1551-2916.2008.02688.x.

[8]   J.C. Ruiz-Morales, D. Marrero-López, J. Peña-Martínez, J. Canales-Vázquez, J.J. Roa, M. Segarra, S.N. Savvin, P. Núñez, Performance of a novel type of electrolyte-supported solid oxide fuel cell with honeycomb structure, J. Power Sources. 195 (2010) 516–521. doi:10.1016/j.jpowsour.2009.08.017.

[9]   K. Rajeswari, P. Biswas, M.B. Suresh, U.S. Hareesh, R. Johnson, D. Das, Colloidal shaping of 8 mol% yttria-stabilized zirconia electrolyte honeycomb structures by microwave-assisted thermal gelation of methyl cellulose, Int. J. Appl. Ceram. Technol. 11 (2014) 154–163. doi:10.1111/j.1744-7402.2012.02852.x.

[10]   S. Celik, B. Timurkutluk, S. Toros, C. Timurkutluk, Mechanical and electrochemical behavior of novel electrolytes based on partially stabilized zirconia for solid oxide fuel cells, Ceram. Int. 41 (2015) 8785–8790. doi:10.1016/j.ceramint.2015.03.104.

[11]   A.M. Sukeshini, R. Cummins, T.L. Reitz, R.M. Miller, Inkjet printing of anode supported SOFC: comparison of slurry pasted cathode and printed cathode, Electrochem. Solid-State Lett. 12 (2009) 176–179. doi:10.1149/1.3243468.

[12]   S. Kirihara, Creation of functional ceramics structures by using stereolithographic 3D printing, Trans. JWRI. 43 (2014) 5–10.

[13]   R.I. Tomov, M. Krauz, J. Jewulski, S.C. Hopkins, J.R. Kluczowski, D.M. Glowacka, B.A. Glowacki, Direct ceramic inkjet printing of yttria-stabilized zirconia electrolyte layers for anode-supported solid oxide fuel cells, J. Power Sources. 195 (2010) 7160–7167. doi:10.1016/j.jpowsour.2010.05.044.

[14]   G. Manogharan, M. Kioko, C. Linkous, Binder jetting: a novel solid oxide fuel-cell fabrication process and evaluation, JOM. 67 (2015) 660–667. doi:10.1007/s11837-015-1296-9.

[15]   A. Zocca, P. Colombo, C.M. Gomes, J. Günster, Additive manufacturing of ceramics: issues, potentialities, and opportunities, J. Am. Ceram. Soc. 98 (2015) 1983–2001. doi:10.1111/jace.13700.

[16]   A. Ghazanfari, W. Li, M.C. Leu, G.E. Hilmas, A novel extrusion-based additive manufacturing process for ceramic parts, in: D.L. Bourell, R.H. Crawford, C.C. Seepersad, J.J. Beaman, S. Fish, H. Marcus (Eds.), Solid Free. Fabr. Symp., Austin, TX, USA, 2016: pp. 1509–1529.

[17]   R.P. Ingel, D. Lewis III, Lattice parameters and density for Y2O3-stabilized ZrO2, J. Am. Ceram. Soc. 69 (1986) 325–332. doi:10.1111/j.1151-2916.1986.tb04741.x.

[18]   ASTM C1327, Standard test method for Vickers indentation hardness of advanced ceramics, West Conshohocken, PA, USA, 2015. doi:10.1520/C1327-15.

[19]   ASTM C1421, Standard test methods for determination of fracture toughness of advanced ceramics, West Conshohocken, PA, USA, 2010. doi:10.1520/C1421-10.

[20]   ASTM C1161, Standard test method for flexural strength of advanced ceramics at ambient temperatures, West Conshohocken, PA, USA, 2013. doi:10.1520/C1161-13.

[21]   K.M. Liang, G. Orange, G. Fantozzi, Evaluation by indentation of fracture toughness of ceramic materials, J. Mater. Sci. 25 (1990) 207–214. doi:10.1007/BF00544209.

[22]   K. Tada, M. Watanabe, Y. Tachi, H. Kurishita, S. Nagata, T. Shikama, Fast reactor irradiation effects on fracture toughness of Si3N4 in comparison with MgAl2O4 and yttria stabilized ZrO2, J. Nucl. Mater. 471 (2016) 69–73. doi:10.1016/j.jnucmat.2015.12.026.

[23]   O.S. Fakolujo, Characterisation and properties improvement of armour ceramics, University of Ottawa, 2016.

[24]   I. Danilenko, F. Glazunov, T. Konstantinova, G. Volkova, V. Burkhovetski, Effect of oxide nanofillers on fabrication, structure, and properties of zirconia-based composites, J. Eur. Ceram. Soc. 33 (2013) 2321–2325. doi:10.1016/j.jeurceramsoc.2013.01.039.

[25]   F. Sahnoune, N. Saheb, P. Goeuriot, Properties of Mullite-Zirconia Composites Prepared through Reaction Sintering Kaolin, α-Al2O3, and ZrO2, Adv. Mater. Res. 160–162 (2011) 1772–1778. doi:10.4028/www.scientific.net/AMR.160-162.1772.

[26]   J.E. Petitjean, X. Huang, R.M. Kearsey, Fracture toughness KIC analysis of Co-doped 7YSZ, Mater. Sci. Technol. 27 (2011) 1606–1609. doi:10.1179/026708310X12756557336319.

[27]   M. Kibsey, J. Romualdez, X. Huang, R. Kearsey, Q. Yang, Mechanical properties of titania-doped yttria stabilized zirconia (TiYSZ) for use as thermal barrier coating (TBC), J. Eng. Gas Turbines Power. 133 (2011) 122101. doi:10.1115/1.4004125.

[28]   P.P. Shukla, J. Lawrence, H. Wu, Fracture toughness of a zirconia engineering ceramic and the effects thereon of surface processing with fibre laser radiation, Proc. Inst. Mech. Eng. Part B J. Eng. Manuf. 224 (2010) 1555–1569. doi:10.1243/09544054JEM1887.

[29]   F. Sahnoune, N. Saheb, Mechanical behavior of mullite-zirconia composites, EPJ Web Conf. 6 (2010). http://dx.doi.org/10.1051/epjconf/20100620005.

[30]   D. Chicot, G. Duarte, A. Tricoteaux, B. Jorgowski, A. Leriche, J. Lesage, Vickers Indentation Fracture (VIF) modeling to analyze multi-cracking toughness of titania, alumina and zirconia plasma sprayed coatings, Mater. Sci. Eng. A. 527 (2009) 65–76. doi:10.1016/j.msea.2009.08.058.

[31]   A. Ghosh, A.K. Suri, B.T. Rao, T.R. Ramamohan, Low-temperature sintering and mechanical property evaluation of nanocrystalline 8 mol% yttria fully stabilized zirconia, J. Am. Ceram. Soc. 90 (2007) 2015–2023. doi:10.1111/j.1551-2916.2007.01683.x.

[32] L.B. Garrido, E.F. Aglietti, L. Martorello, M.A. Camerucci, A.L. Cavalieri, Hardness and fracture toughness of mullite–zirconia composites obtained by slip casting, Mater. Sci. Eng. A. 419 (2006) 290–296. doi:10.1016/j.msea.2006.01.035.

[33] M.H. Sadd, Elasticity: theory, applications, and numerics, second edi, Elsevier, Burlington, MA, USA, 2009.

[34] K. An, H.G. Halverson, K.L. Reifsnider, S.W. Case, M.H. Mccord, Comparison of methodologies for determination of fracture strength of 8 mol % yttria-stabilized zirconia electrolyte materials, J. Fuel Cell Sci. Technol. 2 (2005) 99–103. doi:10.1115/1.1867974.

[35] J. Kondoh, Aging strengthening of 8 mol% yttria-fully-stabilized zirconia, J. Alloys Compd. 370 (2004) 285–290. doi:10.1016/j.jallcom.2003.09.025.

[36] S. Tekeli, The flexural strength, fracture toughness, hardness and densification behaviour of various amount of Al2O3-doped 8YSCZ/Al2O3 composites used as an electrolyte for solid oxide fuel cell, Mater. Des. 27 (2006) 230–235. doi:10.1016/j.matdes.2004.10.011.

[37] S. Heiroth, R. Ghisleni, T. Lippert, J. Michler, A. Wokaun, Optical and mechanical properties of amorphous and crystalline yttria-stabilized zirconia thin films prepared by pulsed laser deposition, Acta Mater. 59 (2011) 2330–2340. doi:10.1016/j.actamat.2010.12.029.

[38] A.G. Mawson, G.A. Carter, R.D. Hart, N.M. Kirby, A.C. Nachmann, Mechanical properties of 8 mol% yttria-stabilised zirconia for solid oxide fuel cells, Mater. Forum. 30 (2006) 148–158.

[39] M. Mazaheri, A.M. Zahedi, M.M. Hejazi, Processing of nanocrystalline 8 mol% yttria-stabilized zirconia by conventional, microwave-assisted and two-step sintering, Mater. Sci. Eng. A. 492 (2008) 261–267. doi:10.1016/j.msea.2008.03.023.

[40] G.D. Quinn, R.C. Bradt, On the vickers indentation fracture toughness Test, J. Am. Ceram. Soc. 90 (2007) 673–680. doi:10.1111/j.1551-2916.2006.01482.x.

[41] ASTM C1683, Standard practice for size scaling of tensile strengths using Weibull statistics for advanced ceramics, West Conshohocken, PA, USA, 2015. doi:10.1520/C1683-10R15.

[42] F.L. Lowrie, R.D. Rawlings, Room and high temperature failure mechanisms in solid oxide fuel cell electrolytes, J. Eur. Ceram. Soc. 20 (2000) 751–760. doi:10.1016/S0955-2219(99)00080-1.

[43] S.P.S. Badwal, F.T. Ciacchi, Oxygen-ion conducting electrolyte materials for solid oxide fuel cells, Ionics (Kiel). 6 (2000) 1–21. doi:10.1007/BF02375543.

[44] I.R. Gibson, G.P. Dransfield, J.T.S. Irvine, Influence of yttria concentration upon electrical properties and susceptibility to ageing of yttria-stabilised zirconias, J. Eur. Ceram. Soc. 18 (1998) 661–667. doi:10.1016/S0955-2219(97)00173-8.

[45] F.T. Ciacchi, K.M. Crane, S.P.S. Badwal, Evaluation of commercial zirconia powders forsolid oxide fuel cells, Solid State Ionics. 73 (1994) 49–61. doi:10.1016/0167-2738(94)90263-1.

[46] A. Ghazanfari, W. Li, M.C. Leu, Y. Zhuang, J. Huang, Advanced ceramic components with embedded sapphire optical fiber sensors for high temperature applications, Mater. Des. 112 (2016) 197–206. doi:10.1016/j.matdes.2016.09.074.

[47] W. Li, A. Ghazanfari, M.C. Leu, R.G. Landers, Methods of extrusion on demand for high solids loading ceramic paste in freeform extrusion fabrication, in: D. Bourell, J. Beaman, R. Crawford, S. Fish, H. Marcus, C. Seepersad (Eds.), Solid Free. Fabr. Symp., Austin, TX, USA, 2015: pp. 332–345.

[48] W. Li, A. Ghazanfari, D. McMillen, M.C. Leu, G.E. Hilmas, J.L. Watts, Properties of partially stabilized zirconia components fabricated by the ceramic on-demand extrusion process, in: D.L. Bourell, R.H. Crawford, C.C. Seepersad, J.J. Beaman, S. Fish, H. Marcus (Eds.), Solid Free. Fabr. Symp., Austin, TX, USA, 2016: pp. 916–928.

IV. ADAPTIVE RASTERING ALGORITHM FOR FREEFORM EXTRUSION FABRICATION PROCESSES[1]

ABSTRACT

An adaptive rastering algorithm has been developed to reduce the 'horizontal' staircase error and/or the fabrication time for freeform extrusion fabrication processes of 3D 'solid' parts. It analyzes the geometry of each layer and changes the width of each line of the raster adaptively in order to reduce the staircase error and/or increase the productivity. For each line, the maximum width that results in a staircase error smaller than a predefined threshold is determined for decreasing the fabrication time or increasing the dimensional accuracy, or both. To examine the efficacy of the proposed technique, examples are provided in which staircase errors and fabrication times are compared between uniform and adaptive rastering methods for each part. The results show a considerable improvement in accuracy and/or fabrication time for all parts studied when using the adaptive rastering algorithm.

1. INTRODUCTION

One of the main challenges facing additive manufacturing processes is the geometrical errors. There are several sources for these errors including representation of CAD files in STL format and approximating complex shapes by lines of deposited material. Many researchers have worked on STL files and tried to repair them (e.g. Leong et al. 1996a,b). This paper focuses on the latter source which is commonly referred to as the staircase effect in the additive manufacturing literature. If this effect is in the Z direction, between layers, as shown in Figure 1(left), it is called 'vertical' staircase effect, and if it is in the XY plane, between lines, as shown in Figure 1(right), it is called 'horizontal' staircase effect. An obvious method to decrease this type of error in both directions is using finer lines. However, this will result in prolonged fabrication time. Approaches to reduce the horizontal staircase effect include printing outer contours, which follow the boundary of every layer, and machining the part after fabrication. These

---

methods might be suitable for polymeric and metallic materials. However, for ceramics the former method may result in lower mechanical strength and the latter method is difficult and expensive. The reason that printing outer contours may considerably reduce the strength of the part is that it may introduce gaps between the outer contours and deposited lines of material in the inner regions and, since ceramics are very sensitive to voids and flaws, the part loses its strength.

Figure 1. Vertical staircase effect (a) versus horizontal staircase effect (b).

In many freeform extrusion fabrication machines, the bottleneck in achieving higher productivity is the maximum attainable travel speed (Gibson et al. 2010; Go & Hart 2015). When the travel speed is set to its maximum value, productivity could be further increased by increasing the feed rate. However, at a constant travel speed, higher material feed rates result in larger lines and, thus, larger staircase errors, creating a compromise between productivity and accuracy. Another approach is setting the travel speed at its maximum value and adaptively changing the feed rate depending on changes in geometry of the part. In other words, when there is no abrupt change in the geometry, higher feed rates are used to decrease the fabrication time; however, lower feed rates are used to build steep slopes and delicate features with fine lines. This concept has been employed in 'adaptive slicing' methods to reduce the 'vertical' staircase effect. Figure 2 shows a simple example where a hemisphere is adaptively sliced to increase the dimensional accuracy. A brief review of adaptive slicing methods is provided in the following paragraphs.
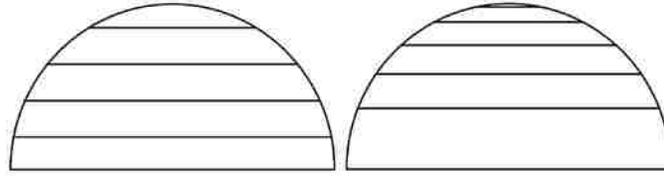
Figure 2. Uniform slicing (left) versus adaptive slicing (right) for a hemisphere.

Dolenc & Makela (1994) introduced the concept of adaptive slicing. They used cusp height to calculate the part's dimensional error for each layer thickness. The user specifies a maximum allowable value for the cusp height, and the surface normal of the preceding intersection plane in the CAD file is compared with that value to determine the optimal layer thickness. Although many researchers still use the cusp height criterion (e.g. Pande & Kumar (2008)), other methods have been proposed to calculate the error. Zhao & Laperriere (2000) proposed an area deviation error criterion to obtain the appropriate layer thickness. Kumar & Choudhury (2005) extended the error criterion to three-dimensional space and introduced a volume deviation criterion for direct adaptive slicing. Singhal et al. (2008) used surface roughness to determine the optimal value for layer thickness between user-defined minimum and maximum values. Hayasi & Asiabanpour (2013) projected all pairs of corresponding slices at the top and bottom of a layer onto the XY, XZ and YZ horizontal surfaces to detect any possible part geometry distortion. They also employed a bottom-up slicing approach where they start cutting at the minimum available thickness to avoid any large geometry deviation errors caused by sharply concave or convex corners.

Chen & Feng (2011) considered the deviation between the final polished part and the CAD file boundary, and optimized the thickness as well as the position of each layer to minimize the number of layers for a given tolerance. Recently, the concept of adaptive slicing has been applied to additive manufacturing of Functionally Gradient Materials (FGM). For example, Wang et al. (2013) proposed a data format for modeling FGM objects and presented an adaptive slicing algorithm based on the finite element concept for FGM, which slices an FGM object into layers and then stores the data according to the proposed data format.

Although the vertical staircase effect has been considered in many papers and various approaches have been proposed to change the layer thickness adaptively, the

horizontal staircase effect has rarely been taken into account. The reason lies in the fact that many additively manufactured parts are not solid (fully dense) and the voids and gaps between inner rasters and outer contours are insignificant. Moreover, the voids and gaps are not as critical for metals and polymers as they are for ceramics. In this paper, the horizontal staircase effect is considered and an algorithm is proposed to estimate this type of error. Furthermore, a technique is developed to reduce this error while increasing the productivity for freeform extrusion fabrication processes of 3D solid parts. Three examples are provided to illustrate the considerable improvement using the proposed method for various geometries.

2. ESTIMATION OF ERROR

As shown in Figure 3, each layer is composed of adjacent parallel lines. The heights of the lines (in the Z direction) are constant and equal to the layer thickness. Their width, w, is subject to change and can take different values in contiguous lines. The length of each line is limited by the STL file boundary such that their midline intersects with the STL boundary at both ends (shown by blue points in Figure 3).
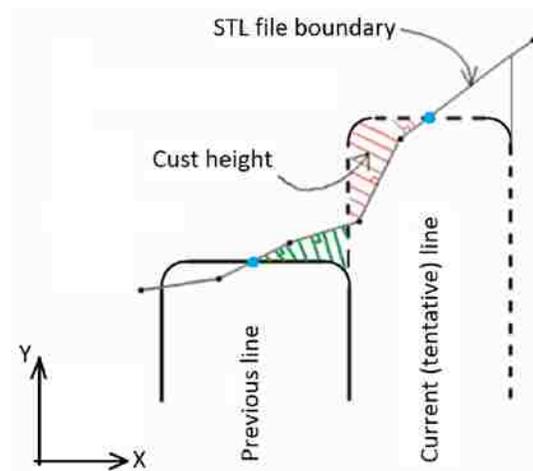
Figure 3. STL fine boundary and adjacent lines forming a layer. Cusp heights are a measure of error.

To estimate the staircase error for each line, the intersections of line boundaries and normals to the STL file boundaries are determined and the maximum of the lengths of these segments is defined as the cusp height and used as a measure of error (see Figure

3). In this figure, the green and red segments are perpendicular to the part boundary in the STL file and intersect with line boundaries. Their maximum length is used as the measure of horizontal staircase error.

As shown in Figure 4, for a point at an arbitrary distance, s_i, from a segment end point (x_1, y_1), the coordinates (x_i, y_i) are

$$\begin{cases} x_i = \dfrac{s_i}{l}(x_2 - x_1) + x_1 \\[2mm] y_i = \dfrac{s_i}{l}(y_2 - y_1) + y_1 \end{cases}$$

(13)

where l is the length of the segment. The cusp height, h_i, at this point is

$$h_i = \left| \begin{matrix} x_i' - x_i \\ y_i' - y_i \end{matrix} \right|$$

(14)
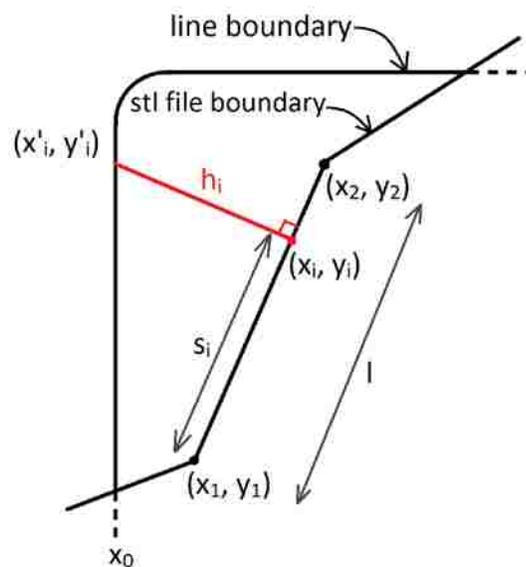
Figure 4. Calculation of cusp height.

Thus, for each segment, by calculating a sufficient number of cusp heights and choosing the maximum value, the error could be estimated. There are four error values to be determined at each step (two at one end as shown in Figure 3 in red and green colors, and two at the other end not shown in the figure) and the maximum of the four values is taken as the error for that line.

Since each layer is composed of a finite number of lines, an error diagram for each layer could be plotted by calculating the error values for each line. A program has been written in MATLAB which reads the geometry of the part from a CAD file in STL format, finds the intersections of the representative surfaces of the part with horizontal planes and forms the boundaries for each layer. After layer boundaries are obtained from the STL file, rastering is performed to fill in the build area with lines. Figure 5 shows an object along with the rastering and an error diagram for one of its layers rastered with lines of 1.5 mm width. Each error corresponds to one line and each line is represented by a straight line passing through its center. The horizontal staircase effect manifests in regions with sharp changes in the shape.
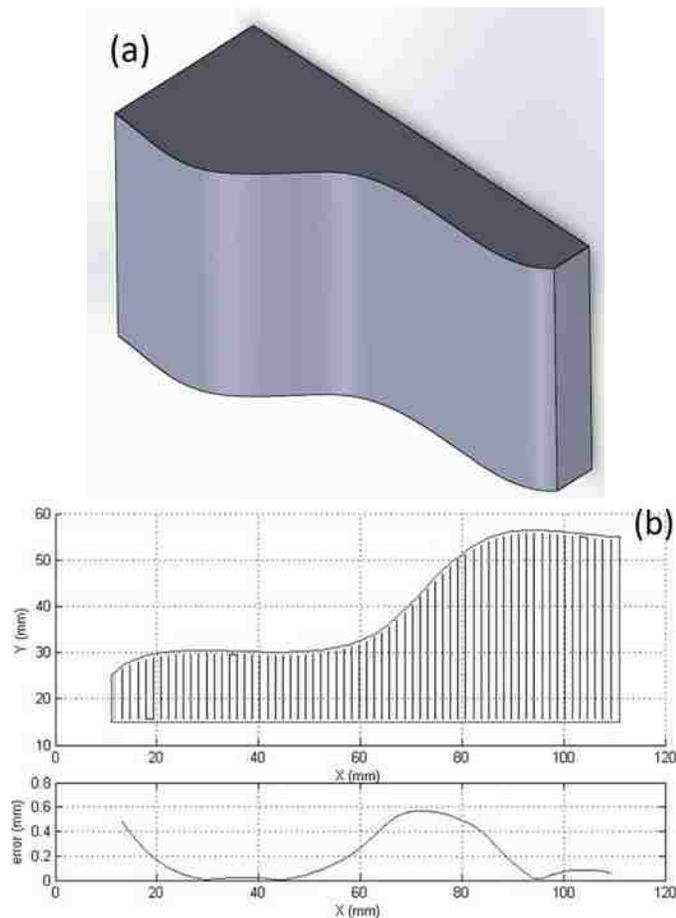
Figure 5. An object (a) along with the rastering and error diagrams for one of its layers rastered with lines of 1.5 mm width (b).

A smaller line width reduces the error, but increases the fabrication time. As an example, the layer illustrated in Figure 5 is considered and it is assumed that the travel speed is 100 mm/s. For various line widths, the required fabrication time is plotted versus the maximum error in Figure 6. The markers on the curve correspond to line widths of 0.2, 0.5, 1.0, 1.5, 2.0, 2.5 and 3.0 mm, from left to right, respectively (e.g. using a width of 1 mm results in a maximum error of 0.38 mm and 23.7 s of fabrication time). As the diagram clearly demonstrates, to achieve high accuracy, an unreasonably large amount of fabrication time is required. To overcome this problem, an adaptive rastering algorithm is proposed in the next section.
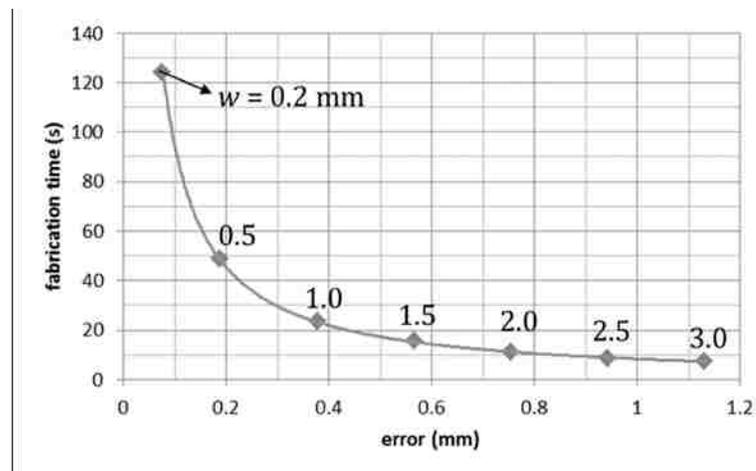
Figure 6. Fabrication time for each layer represented in Figure 5 as a function of maximum error.

3. ADAPTIVE RASTERING ALGORITHM

In this section, adaptive rastering is proposed as an efficacious solution to reduce horizontal staircase errors or fabrication time, or both. This technique is based on using the smallest line width as needed and larger line widths elsewhere in order that the errors stay within a pre-specified tolerance. In other words, the smallest line width is used where there is a sharp change in the part geometry and larger line widths for the rest of the part.

From a practical perspective, there are limitations on the minimum and maximum values of the line width. For a constant table speed (which is set at its maximum value), line width depends on the size of the extrusion nozzle as well as the feed rate. For a given

nozzle and a certain table speed, line width could only be adjusted in a certain range by changing the feed rate. Decreasing the feed rate below this critical value results in printing a discontinuous line. The upper bound of this range is limited by the fluidity of the extrudate since it can only flow a certain distance, d, from the nozzle as shown in Figure 7. Furthermore, changes in the feed rate cannot follow a step reference, i.e., sudden jumps in the value of feed rate is not physically possible. This means that either the widths of two consecutive lines have to be equal (so that no sudden change in feed rate is required), or the extrusion process has to be stopped between the two lines (so that the next line can be printed at desired width). Accordingly, to avoid an unreasonably large number of starts and stops, a limited number of line widths should be used. In this way, lines having the same width are printed continually. As an example, Figure 8 shows a layer rastered with three line widths. Initially, all the lines with the smallest width, w_1, are printed as shown in the left picture with cyan; next, lines of second width, w_2, are printed as shown in the middle picture with magenta; and finally, the widest lines, w_3, are printed as the right picture illustrates with green color.
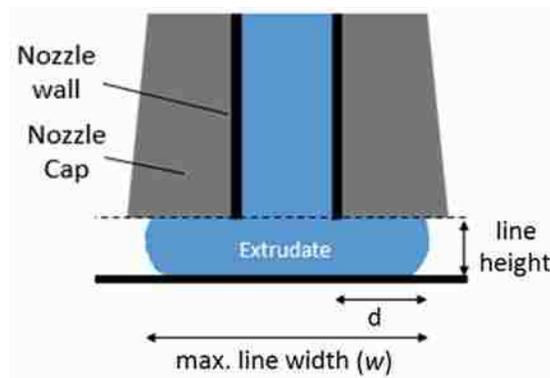
Figure 7. Dimensions of the extrudate.

It is worth noting that the same error estimation method explained in the second section above applies for calculating the error of discontinuous line segments shown in Figure 8. For each segment, the maximum cusp height is found, and the largest value among these cusp heights for the various segments is taken as the error for that line.

Figure 9 shows the flowchart of this algorithm assuming three line widths are allowed. Although three widths are assumed in the flowchart, any number of line widths can be assumed using essentially the same algorithm. Rastering starts from the leftmost

line. The smallest line width (w_1) is examined initially and the corresponding error is calculated. The error is compared against the maximum allowable value predefined by the user. If the error is below the tolerance, the second line width (w_2) is tested. If the error for w_2 is above the threshold, w_1 will be used to print that line. Otherwise, the largest line (w_3) is tested and, if the error is above the tolerance, w_2 will be used. Otherwise, w_3 will be chosen. This process is repeated for all lines until the entire layer is covered.
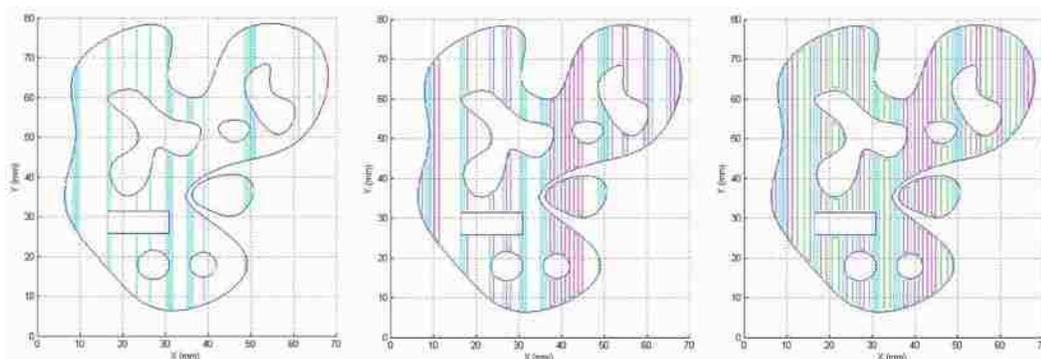
Figure 8. Rastering sequence of a layer with three line widths.
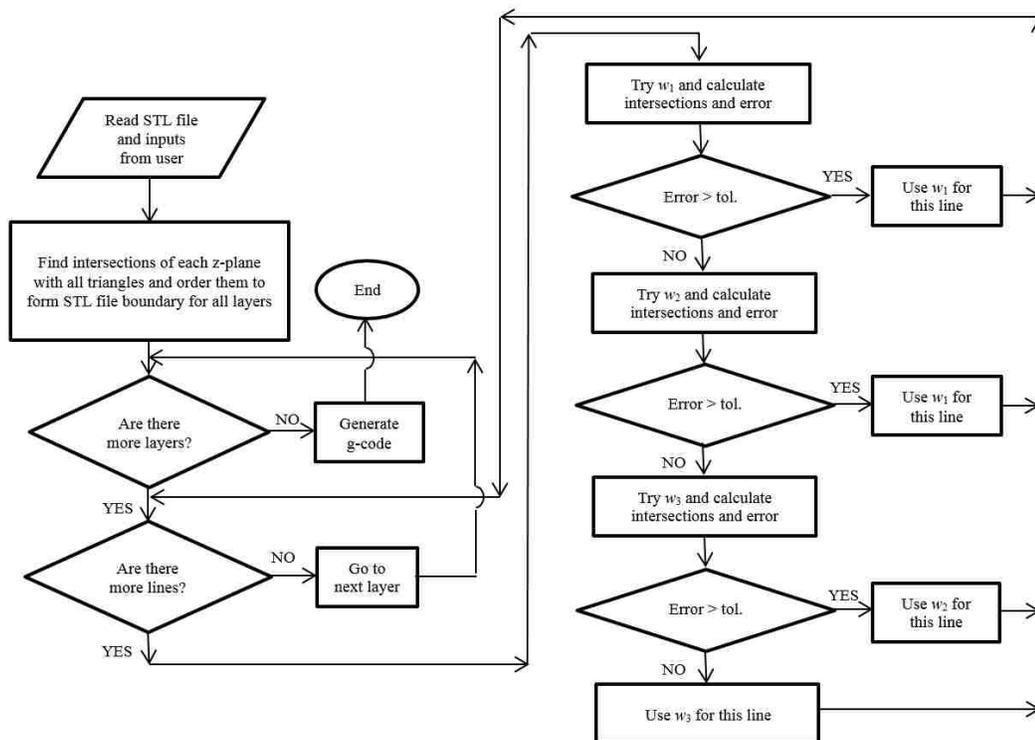
Figure 9. Flowchart of adaptive rastering algorithm.

To implement this method, a program has been developed in MATLAB which reads the geometry of the CAD file in STL format, slices the part into layers, determines the sequence and width of each line for all the lines to print each layer, and generates a g-code for a freeform extrusion fabrication machine to print the part.

It is important to note that the choice of line widths determines the maximum error and fabrication time. As an example, for the layer shown in Figure 5, values of 0.8, 1, and 3 mm for w_1, w_2, and w_3, result in a maximum error of 0.118 mm and a fabrication time of 44.5 s. The adaptively rastered layer along with the error diagram is illustrated in Figure 10 where cyan, magenta and green colors correspond to line widths of 0.8, 1.0 and 3 mm, respectively. Different values of line widths result in different fabrication times and errors. Figure 11 shows 19 points in 'fabrication time versus error' diagram, each of which corresponding to one set of line widths (w_1, w_2, w_3). The maximum error value mainly depends on the choice of the smallest line width, while the other widths are obtained by trial and error to reduce the fabrication time. For a predetermined error, there is a certain limit for reduction of fabrication time (e.g. for a maximum allowable error of 0.39 mm, the minimum fabrication time is 13.4 s). This limit forms the Pareto optimal frontier represented by the red curve in Figure 11. For points on this curve, further reduction in fabrication time is not feasible without an increase in error. Perspicuously, only points on the Pareto optimal frontier are used in adaptive rastering.
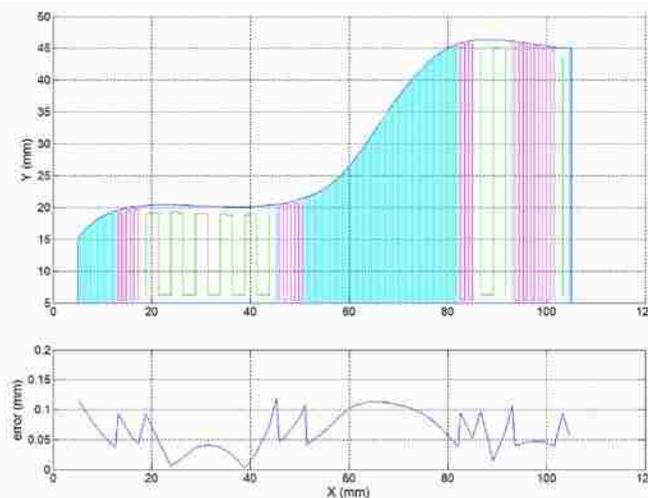
Figure 10. A layer adaptively rastered with 0.8, 1 and 3 mm line width shown in cyan, magenta and green colors, respectively. Each point in the error diagram corresponds to one line.
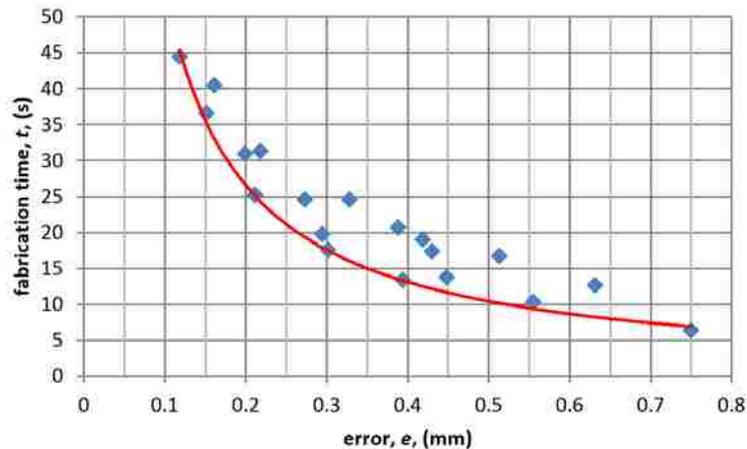
Figure 11. Fabrication time versus error for a layer represented in Figure 5 for various sets of line widths. Each point corresponds to one set of line widths (w_1, w_2, w_3) and the red line represents the Pareto optimal frontier.

Figure 12 compares uniform (from Figure 6) and adaptive (from Figure 11) rastering for the same layer. As the figure shows, three different approaches could be made for adaptive rastering of a part depending on the choices for line widths. For a point, A, on the blue curve, one approach could be choosing a set of line widths for adaptive rastering which reduces the fabrication time without an increase in error (point B on the red curve). Another approach is choosing line widths corresponding to point C where there is a considerable decrease in error while fabrication time remains unchanged. The third approach is moving from A to D which reduces both error and time.
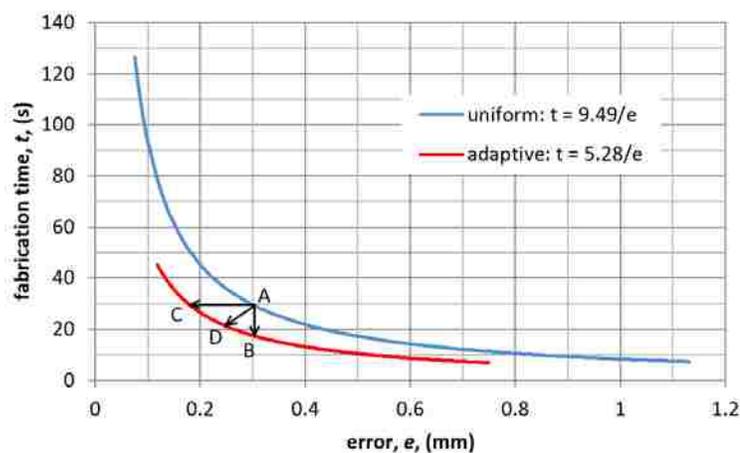
Figure 12. Uniform and adaptive rastering for a layer represented in Figure 5.

4. CASE STUDIES

4.1. PART #1

As an illustrative example, a cylinder is considered and three adaptive rastering approaches explained above are examined to adaptively raster each layer of the cylinder. In the first approach only the fabrication time is decreased; in the second approach errors are reduced; whereas the third approach reduces both errors and fabrication time simultaneously. The results are compared to uniform rastering with a line width of 1 mm which results in a maximum error of 0.485 mm and a fabrication time of 27.58 s for each layer (assuming 100 mm/s for the travel speed). As shown in Figure 13 (left), the error values decrease linearly toward the middle of the part. Figure 13 (right) shows an adaptively rastered layer using the second approach. Cyan, magenta and green colors correspond to line widths of 0.6, 1.0 and 1.6 mm, respectively. As the error diagram below the picture indicates, the maximum error is 0.325 mm. The results of the three approaches are represented in Table 1 and are compared against the uniform rastering. If the errors are not to be reduced, there is 34.5% decrease in fabrication time. If the productivity is not to be improved, errors decrease by 33.0%. There could also be a 14.0% and 20.6% simultaneous reduction in error and time, respectively, when using the third approach.

Table 1. Comparison between uniform and adaptive rastering for a layer of a cylinder.

Rastering	Line width (mm)	Maximum error (mm)	Reduction (%)	Fabrication time (s)	Reduction (%)
Uniform	1.0	0.485	-	27.58	-
Adaptive #1 (A → B)	1.0, 1.3, 2.0	0.485	**0**	18.06	**34.5**
Adaptive #2 (A → C)	0.6, 1.0, 1.6	0.325	**33.0**	27.58	**0**
Adaptive #3 (A → D)	0.8, 1.0, 1.6	0.417	**14.0**	21.90	**20.6**
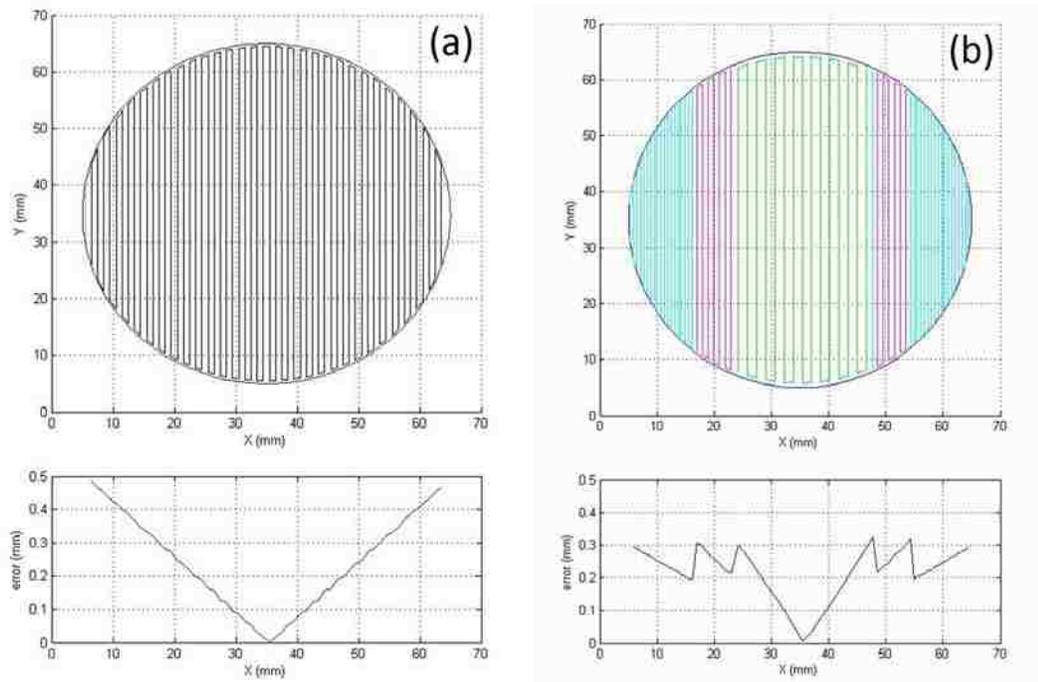
Figure 13. Uniform rastering of a layer of a cylinder (a) and adaptive rastering (b).

4.2. PART #2

In this example, the part shown in Figure 5 is considered. First, assuming uniform rastering, the maximum allowable error is determined to the extent that the manufacturer of the part attains maximum profit. Next, it is demonstrated how employing the adaptive rastering algorithm enables the manufacturer to produce cheaper parts with higher quality, and gain more profit. The mathematical models used in this example for cost and price are simplified models based on more advanced models found in microeconomics books (Mansfield 1994; Sower 2011; Mahanty 2014).

The manufacturer's objective is to maximize the 'amount of profit per unit time' which is

$$P = (p - c) \times n \tag{15}$$

where P is profit per unit time ($/h), p is price a customer is willing to pay per part, c is cost of fabricating each part and n is number of parts produced per unit time.

Assuming the price a customer pays linearly decreases with error, e, ($p = a - be$) and cost linearly depends on time, T, plus raw material, d, ($c = cT + d$), the profit ($/h) will be

$$P = ((a e - b e c) - (c T + d)) \times 60/T \qquad (16)$$

It is assumed that a perfect part ($e \approx 0$) could be sold at \$100 and an inferior part ($e = 1$ mm) at \$30 ($a = \$100$, $b = 70$ \$/mm), cost of using the 3D printer is 1 \$/min ($c = 1$ \$/min) and raw material is \$20 ($d = \$20$), and the part is made of 60 layers.

To write the profit in terms of only error, the relationship between fabrication time, T, and error, e, should be substituted in equation (4). Using Figure 12, the required time for manufacturing each part for both uniform and adaptive rastering is approximated by a homographic function of the form

$$T(e) = \frac{f}{e \left(\frac{1}{60} \right)} \qquad (17)$$

where $f = 9.49$ for uniform rastering and $f = 5.28$ for adaptive rastering. By substituting equation (5) into equation (4)

$$P \left(\frac{e}{T} \right) = [(a e - b e c) - (\frac{c f}{60} + d)] \times \frac{60 e}{f} \qquad (18)$$

and taking the derivative with respect to e, the optimum value of e for which the manufacturer will gain maximum profit could be easily found ($e = \frac{a e + d}{2 b} = 0.571$ mm).

As shown in Table 2, this results in a price of \$60, a cost of \$36.6, a productivity of 3.61 parts per hour, and a profit of 84.5 \$/h for uniform rastering, and a price of \$60, a cost of \$29.2, a productivity of 6.49 parts per hour, and a profit of 199.7 \$/h for adaptive rastering. Thus, the manufacturer gains 2.36 times more profit by employing the adaptive rastering algorithm.

Table 2. Comparison between uniform and adaptive rastering for part #2.

Rastering	Price (\$)	Cost (\$)	Productivity (parts/h)	Profit (\$/h)
Uniform	60	36.6	3.61	**84.5**
Adaptive	60	29.2	6.49	**199.7**

4.3. PART #3

The third part is very similar to one of the examples chosen by Panhalkar et al. (2014) for adaptive slicing and is illustrated in Figure 14 (left). Similar to Part #1, three approaches are examined to adaptively raster each layer. In the first adaptive rastering approach, only the fabrication time is decreased; in the second approach errors are reduced, whereas the third approach reduces both errors and fabrication time simultaneously. The results are compared to uniform rastering with a line width of 0.5 mm and layer thickness of 1 mm which results in a maximum error of 0.249 mm and a fabrication time of 230 min for the whole part (assuming 100 mm/s for travel speed). Figure 14 (middle and right) shows two adaptively rastered layers using the first approach. Cyan, magenta and green colors correspond to line widths of 0.5, 0.7 and 1.2 mm respectively. The results of the three approaches are represented in Table 3 and are compared against the uniform rastering. If the errors are not to be reduced, there is 40.9% decrease in fabrication time. If the productivity is not to be improved, errors decrease by 37.7%. There could also be a 14.0% and 25.6% simultaneous reduction in error and time, respectively, when using the third approach.

Table 3. Comparison between uniform and adaptive rastering for part #3.

Rastering	Line width (mm)	Maximum error (mm)	Reduction (%)	Fabrication time (min)	Reduction (%)
Uniform	0.5	0.249	-	230	-
Adaptive #1 (A → B)	0.5, 0.7,1.2	0.249	**0**	136	**40.9**
Adaptive #2 (A → C)	0.3, 0.5, 0.8	0.155	**37.7**	230	**0**
Adaptive #3 (A → D)	0.4, 0.6, 1	0.214	**14.0**	171	**25.6**

5. SUMMARY AND CONCLUSIONS

An adaptive rastering algorithm has been developed to reduce the 'horizontal' staircase error and/or to increase the productivity for freeform extrusion fabrication processes. To estimate the horizontal staircase error for each line, the intersections of deposition line boundaries and lines perpendicular to STL file boundaries were

determined and the maximum lengths of these segments was taken as the error. The algorithm determines the width of every line of the rasters in order to reduce the error, to increase the productivity, or to both reduce error and increase productivity simultaneously.
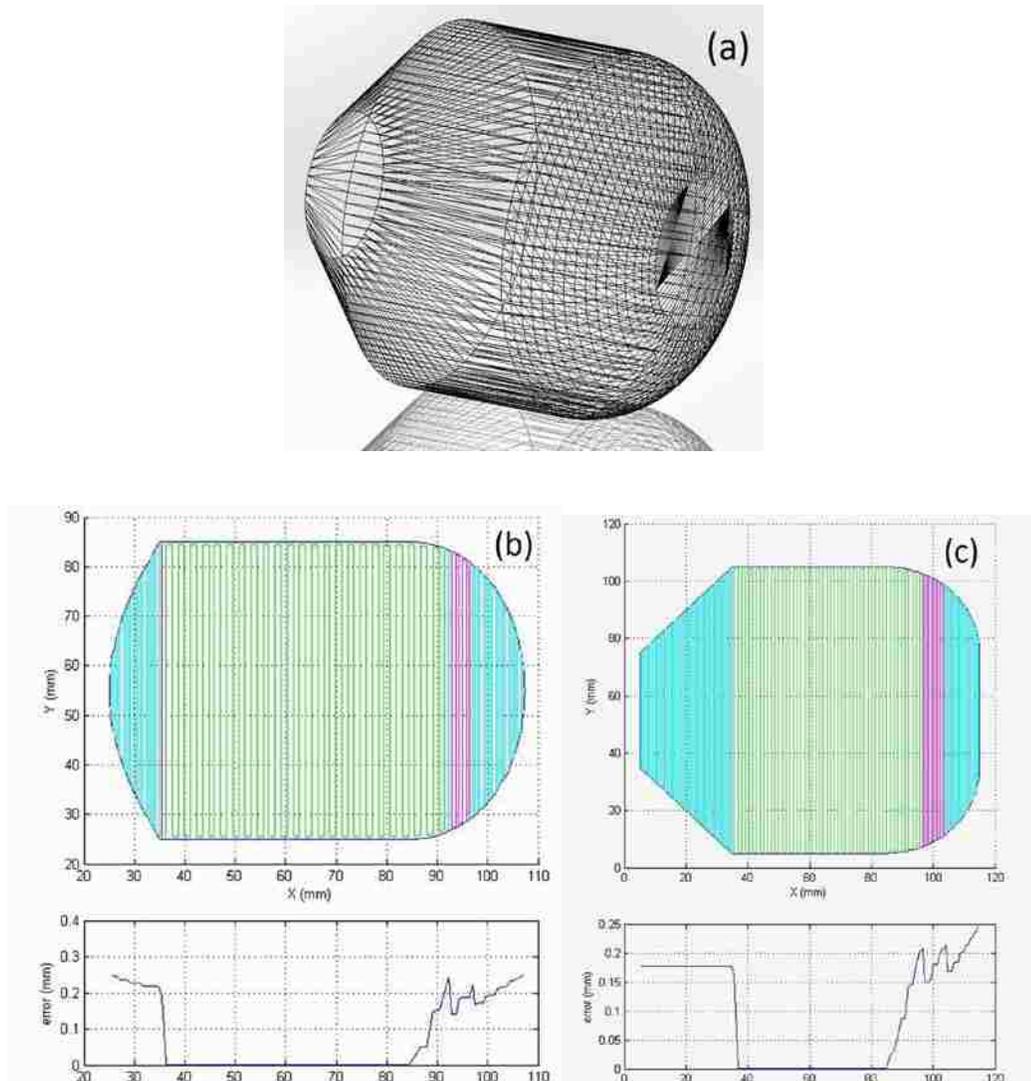
Figure 14. STL representation of Part #3 (a) and adaptive rastering of two sample layers (b) and (c).

Three representative parts were studied to examine the efficacy of the proposed technique. In the first case study, a cylinder was chosen for which the adaptive rastering resulted in 20.6% and 14% reduction in fabrication time and error, respectively. In the second example, an optimization problem was considered to maximize the amount of profit in a small manufacturing unit. The maximum attainable profit per hour was 2.36

times higher when adaptive rastering was employed. In the last case study, a more realistic part previously studied in adaptive slicing was adaptively rastered using different approaches. When the errors were not to be reduced, a 40.9% reduction was observed in fabrication time; when the productivity was held constant, errors decreased by 37.7%. Thus, it could be concluded that the adaptive rastering algorithm proposed in this paper can considerably improve the dimensional accuracy and/or fabrication time.

ACKNOWLEDGEMENTS

REFERENCES

Chen JS, Feng H 2011. Optimal layer setup generation in layered manufacturing with a given error constraint. The Society of Manufacturing Engineers. Journal of Manufacturing Systems 30: 165–174.

Dolenc A, Makela I 1994. Slicing procedures for layered manufacturing techniques. Computer-Aided Design 26: 119–126.

Gibson I, Rosen DW, Stucker B 2010. Additive Manufacturing Technologies. Springer.

Go J, Hart AJ 2015. Rate Limiting Tradeoffs in Machine Design for Extrusion-based Additive Manufacturing. Austin, Texas. 26th Annual International Solid Freeform Fabrication Symposium.

Hayasi MT, Asiabanpour B 2013. A new adaptive slicing approach for the fully dense freeform fabrication (FDFF) process. Journal of Intelligent Manufacturing 24: 683–694.

Kumar C, Choudhury AR 2005. Volume deviation in direct slicing. Rapid Prototyping Journal 11: 174–184.

Leong KF, Chua CK, Ng YM 1996. A study of stereolithography file errors and repair, Part 1: Generic solution. International Journal of Advanced Manufacturing Technology 12: 407-414.

Leong KF, Chua CK, Ng YM 1996. A study of stereolithography file errors and repair, Part 2: Special cases. International Journal of Advanced Manufacturing Technology, 12: 415-422.

Mahanty AK, 2014. Intermediate microeconomics with applications. Academic Press.

Mansfield E, 1994. Applied microeconomics. W. W. Norton and Company.

Pande SS, Kumar S 2008. A generative process planning system for parts produced by rapid prototyping. International Journal of Production Research 46: 6431–6460.

Panhalkar N, Paul R, Anand S 2014. Increasing part accuracy in additive manufacturing processes using a k-d tree based clustered adaptive layering. Journal of Manufacturing Science and Engineering.

Singhal SK, Prashant KJ, Pulak MP 2008. Adaptive slicing for SLS prototyping. Computer-Aided Design and Appli- cations 5: 421–3.

Sower V, 2011. Better Business Decisions Using Cost Modeling: For Procurement, Operations, and Supply Chain Professionals. Business Expert Press.

Wang S, Wang Y, Chen C, Zhu X 2013. An adaptive slicing algorithm and data format for functionally graded material objects. International Journal of Advanced Manufacturing Technology 65: 251–258.

Zhao ZW, Laperriere L 2000. Adaptive direct slicing of the solid model for rapid prototyping. International Journal of Production Research 38: 69–83.

V. OPTIMAL RASTERING ORIENTATION IN FREEFORM EXTRUSION FABRICATION PROCESSES[1]

ABSTRACT

Many researchers have tried to optimize the build direction of additively manufactured parts to minimize the vertical staircase effect. However, the horizontal staircase effect should also be considered when fully dense parts are to be fabricated. In this paper, part inaccuracy due to the horizontal staircase effect is considered in order to determine the optimal rastering orientation in building the part. An algorithm is developed to estimate this inaccuracy and a technique is proposed to minimize it. The effect of rastering orientation on staircase errors is examined, and the particle swarm optimization method is used to determine the optimum rastering angle that leads to minimum errors for each layer. Several case studies are considered where the staircase errors are calculated with and without optimizing the rastering orientation. The results show that the errors can be reduced considerably when using the optimal rastering orientation. To verify the analytical results, parts are fabricated using a freeform extrusion fabrication process at various angles and the errors are compared.

1. INTRODUCTION

Dimensional accuracy has always been an important challenge in all additive manufacturing technologies [1]. The inaccuracy is a result of employing lines of deposited material to approximate the complex shape of a part. This phenomenon is frequently called the staircase effect. When this effect occurs between adjacent layers, it is referred to as "vertical staircase effect" and if it is between contiguous lines in a layer, the term "horizontal staircase effect" is used. One way to reduce this effect is decreasing the size of the line which will patently protract the fabrication process as well. An efficacious scheme used to reduce the "vertical" staircase effect is optimizing the

---

deposition orientation. Many researchers have employed different optimization methods to achieve this aim considering various objective functions and constraints.

Cheng et al. [2] considered accuracy as the primary objective and productivity as the secondary objective in stereolithography and proposed a method to determine an optimum deposition orientation. Productivity was increased by reducing the number of layers. First, orientations resulting in low error values were chosen and among them, the one leading to the shortest fabrication time was selected. Alexander et al. [3] optimized part accuracy and cost in stereolithography and fused deposition modeling by determining the deposition orientation. They selected average weighted cusp height as a measure of accuracy and proposed models to predict cost as a function of orientation for the two processes. Thrimurthulu et al. [4] obtained an optimum deposition orientation for the fused deposition modeling process, which enhanced part surface finish and reduced build time. Models for evaluation of average part surface roughness and build time were developed and a real-coded genetic algorithm was used to obtain the optimum solution.

Canellidis et al. [5] proposed a framework that constitutes two independent modules. The first module evaluates how "good" a randomly selected orientation is by assessing the fabrication time, defined as build time plus post-processing time, as the main cost/time criterion and the part's average surface roughness as the overall quality criterion. The combined effect of the two criteria was evaluated through a weighted multi-criteria objective function. Phatak and Pande [6] sliced a CAD model of the part and hollowed it with the desired shell thickness. A genetic algorithm based strategy was then used to obtain the optimum part orientation. The objective of optimization was a weighted average of performance measures such as build time, part quality, and the material used in the hollowed model.

Paul and Anand [7] examined the relationship between cylindricity form error and build orientation using three methods: a simple analytical model, the CAD model of the part, and the STL file of the part. The results were then used to obtain the critical orientation zones that minimize the cylindricity error for a part. The method was demonstrated by determining the optimal orientation zones of a test part with multiple cylindrical features. In another paper [8], they also analyzed the effect of part orientation on cylindricity and flatness form errors. An algorithm to calculate the optimal orientation

for minimizing flatness and cylindricity errors was developed and tested. They noticed that an optimal orientation for minimum form errors may result in a greater utilization of support structures. Thus, they tried to minimize the volume of support structures while minimizing the cylindricity and flatness errors.

The most common practical approach to reduce the horizontal errors is surrounding the inner rasters by outer contours. However, although this approach improves the surface finish, it introduces gaps between the outer contours and inner rasters. These gaps affect the mechanical properties of the part, especially if the part is to be made of ceramic materials which are very sensitive to imperfections. In this paper, the horizontal staircase effect is minimized by optimizing the rastering orientation for each individual layer. An algorithm is developed to estimate the error and the Particle Swarm Optimization (PSO) method is used to find the rastering orientation which results in minimum error. One of the designed parts is fabricated via a freeform extrusion fabrication process to verify the analytical results.

2. ERROR ESTIMATION ALGORITHM

As shown in Figure 1, each layer is composed of parallel lines with a constant width and a constant thickness. Since in the fabrication process the material is extruded through a circular nozzle, the lines are assumed to have a circular end shape. Their length is limited between the part's stl file boundary such that the midline intersects with the stl boundary at both ends (shown by the blue points in Figure 1).
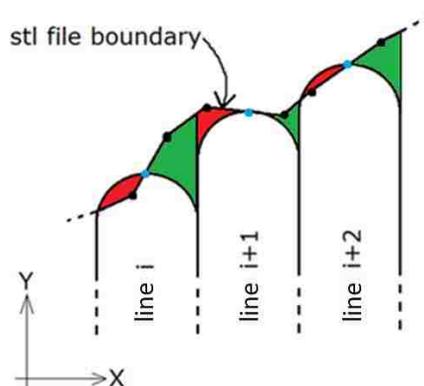
Figure 1. Stl file boundary and parallel lines forming a layer. Areas between lines and the stl file boundary filled with red and green colors are a measure of staircase error.

To estimate the staircase error for each line, the areas between the stl file boundary and line boundary are calculated and assumed to be a measure of error. There are four error values for each line (two at one end as shown in red and green colors in Figure 1, and two at the other end not shown in the figure) and the maximum of the four values is considered to be the error for that line. To calculate the four areas for each line, a numerical integration technique (trapezoidal rule) is employed. Each area can be obtained using

$$A_{ij} = \int_{x_0}^{x_0 + w} |f(x) - g(x)| dx = \frac{w}{2N} \sum_{k=1}^{N} |f(x_{k+1}) - g(x_{k+1})| + |f(x_k) - g(x_k)| \qquad (19)$$

where A_{ij} is the jth ($j = 1,2,3,4$) area corresponding to the ith line, x_0 corresponds to the left edge of the line, w is the line width, f represents the stl file boundary, g is the line boundary, and N is the number of equally spaced integration panels. The lines could be along any direction, but the same procedure is used to calculate the areas by rotating the coordinate system so that the Y direction is along the line's direction.

Since each layer is composed of a finite number of lines, an error diagram for each layer could be plotted by calculating the error for each line. A program is written in MATLAB which reads the geometry of the part from a CAD file in stl format, finds the intersections of the representative surfaces of the part with horizontal planes and forms the boundary for each layer. After the layer boundary is obtained from the stl file, rastering will be performed to fill in the desired area with lines for the layer. Figure 2 shows the rastering and error diagrams for a layer of an arbitrary object rastered with lines of 0.9 mm width. Each error value corresponds to one line and each line is represented by a straight line passing through its center.

By changing the rastering orientation of the layer, the errors change significantly as shown in Figure 3, where an arbitrary shape rastered with lines of 0.9 mm width is rotated 45° CCW. The rotation results in a 33.7% reduction in maximum error while the fabrication time remains constant. Thus, developing an optimization algorithm to find the optimum rastering orientation could result in a considerable improvement in part accuracy without sacrificing productivity.
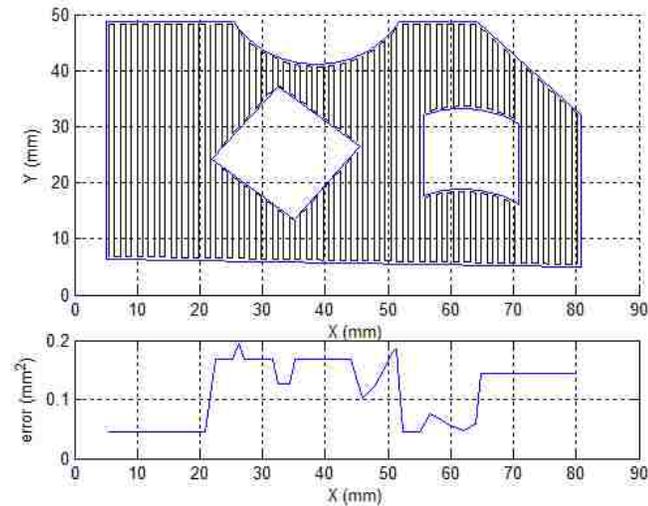
Figure 2. Rastering and error diagram for a layer of an arbitrary object rastered with 0.9 mm wide lines.
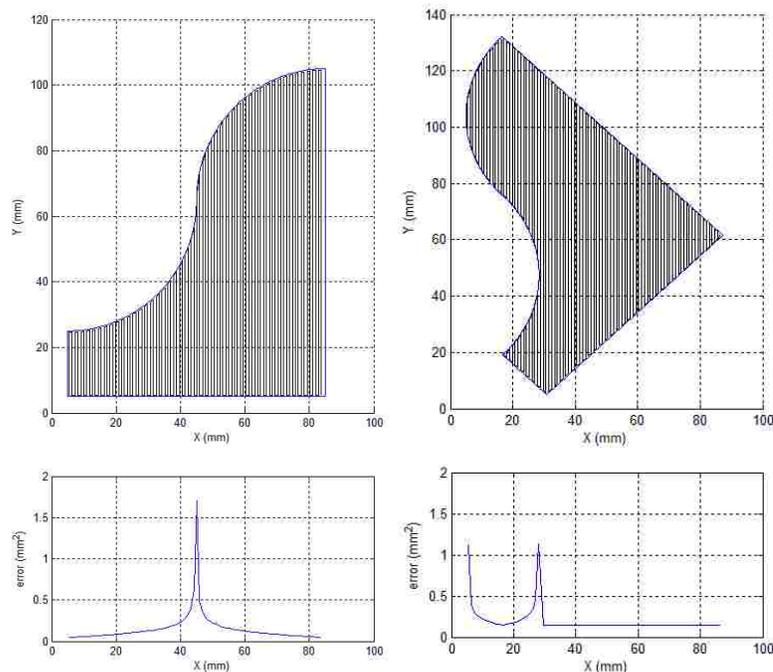
Figure 3. An arbitrary shape rastered at two different orientations along with the error daigram for each orientation.

3. PARTICLE SWARM OPTIMIZATION

Kennedy and Eberhart [9] introduced the Particle Swarm Optimization (PSO) method, which is an evolutionary computational technique based on swarm intelligence. In this method, each candidate solution to the optimization problem is considered as the trajectory of a particle and is adjusted in the search space based on the experience of its

own as well as other particles in the swarm. It is assumed that there are N particles in the swarm and the particles can move in a D-dimensional search space. The set of parameters in the ith iteration are represented by the position vector of the jth particle, $X_j^i = (x_{j1}^i, x_{j2}^i, ..., x_{jD}^i)$, and changes in the parameters are represented by velocity of the particle, $V_j^i = (v_{j1}^i, v_{j2}^i, ..., v_{jD}^i)$. Initially, the N particles are randomly distributed in the space and finally all of them will reach the optimal point.

The key step in PSO is calculating the velocity of each particle at each iteration. This velocity depends on the previous velocity of the particle, the historical best value for the particle, and the historical best value of all particles as follows:

$$V_j^i = \theta V_j^{i-1} + c_1 r_1 \left[P_{best,j}^{i-1} - X_j^{i-1} \right] + c_2 r_2 \left[G_{best}^{i-1} - X_j^{i-1} \right] \tag{20}$$

where $P_{best,j}$ is the position of jth particle corresponding to the best value of the objective function encountered by this particle in all the previous iterations; G_{best} is the position of the particle experiencing the best value of the objective function encountered in the previous iterations by any of the N particles; c_1 and c_2 are the cognitive (individual) and social (group) learning rates, respectively; r_1 and r_2 are uniformly distributed random numbers in the range 0 to 1; and θ is known as the inertial weight and is calculated by

$$\theta = \theta_{max} - \left(\frac{\theta_{max} - \theta_{min}}{i_{max}} \right) i \tag{21}$$

where θ_{max} and θ_{min} are the initial and final values of the inertia weight, respectively, and i_{max} is the maximum number of iterations. The values of $\theta_{max} = 0.9$ and $\theta_{min} = 0.4$ are commonly used [10].

Having the velocities of all particles, the position of each particle is

$$X_j^i = X_j^{i-1} + V_j^i \tag{22}$$

This iterative procedure continues until a convergence criterion is met (e.g., the difference between the global best fitness of the last two iterations is smaller than a certain value, or the global best fitness does not change after a certain number of iterations).

Note that other derivative-free optimization algorithms such as genetic algorithms, simulated annealing, ant colony optimization, fuzzy optimization, and neural-network-based methods may also be used to determine the optimum deposition angle.

4. RASTERING ORIENTATION OPTIMIZATION

The objective function to be minimized is the maximum error which is a function of rastering orientation. Two different approaches could be made to minimize the horizontal errors: (1) optimizing the orientation of the part in 3D space while the rasters remain in the same direction, and (2) maintaining part orientation constant while optimizing the rastering orientation separately for each layer.

In the first method, the following unconstrained optimization problem is solved

$$\text{minimize } e_{max}^{horz}(\theta_x, \theta_y, \theta_z) \tag{23}$$

where e_{max}^{horz} is the maximum horizontal error for the entire part, and $\theta_x, \theta_y \text{ and } \theta_z$ are the rotation angles of the part around x, y and z axes, respectively. The rasters are in the horizontal plane along the y direction. The iteration starts with a population of random values for the three angles. The maximum error for the entire part for each set of angles is calculated using the algorithm explained in the "error estimation algorithm" section. Based on these values PSO determines the next set of angles. This procedure continues until the optimum orientation is found for the part.

In the second approach, the part orientation is unchanged, and, for each layer, the optimum rastering angle, α^k, is determined to minimize the maximum error. Since the rasters are assumed to be horizontal, only one angle is enough to determine their orientation in space. The unconstrained optimization problem is

$$\text{minimize } e_{max}^k(\alpha^k) \quad k = 1, 2, ..., M \tag{24}$$

where k denotes layer number and M is the total number of layers. For the kth layer, initially, a population of random values is generated and corresponding errors are calculated using the algorithm explained in "error estimation algorithm" section. These values are then utilized in the second iteration to calculate the next angles via PSO, and

the procedure is repeated until a convergence criterion is met. The same process is carried out for $k+1^{th}$ layer until each layer is rastered at an optimal angle.

The first approach might be more effective in some cases (e.g., a 2.5D part could be aligned in such a way that all the layers have a rectangular boundary and errors are virtually zero). However, by changing the part orientation, vertical errors will also be affected and a dramatic increase in their values might be possible. The second method, on the other hand, does not alter the vertical errors. Thus, one of the methods described in the introduction section [2-8] could be first employed to determine the optimal part orientation to minimize the vertical errors, and then the proposed approach here could be used to minimize the horizontal errors without affecting the vertical errors. Moreover, the second method deals with each layer separately and independently, so the number of parameters to be optimized, i.e., the degrees of freedom, is equal to the number of layers whereas in the first method, there are only three parameters to manipulate.

Accordingly, the second approach was chosen and the rastering direction was optimized for each layer independently in order to minimize the horizontal errors. Table 1 represents the parameters used in PSO.

Table 1. Parameters used in PSO.

Maximum number of iterations (i_{max})	100
Population size (N)	10
Cognitive (individual) learning rates (c_1)	2
Social (group) learning rates (c_2)	2
Initial value of the inertia weight (θ_{max})	0.9
Final value of the inertia weight (θ_{min})	0.4
Change in global best for termination (mm^2)	0.00001

5. CASE STUDIES

5.1. SPUR GEAR

A spur gear (Figure 4) is considered in the first case study and lines of 0.9 mm width are chosen to raster the part. The initial rastering orientation is shown in Figure 5 (left) where the maximum error is 1.794 mm^2. Figure 6 illustrates how PSO converges to the optimal value in 35 iterations. The optimum rastering orientation for spur gear is 157.47° CW which results in 0.370 mm^2 error (see Figure 5 (right)). Thus, optimizing the rastering orientation results in a **79.4% reduction** in maximum horizontal error for this

spur gear. It should be noted that since only the rastering orientation is changed, the travelling distance of the table remains constant for each layer and for the entire part. Thus, the fabrication time does not change. Furthermore, the orientation of the part in 3D space is not altered. Hence, the amount of support material and the number of layers are the same as the original values.
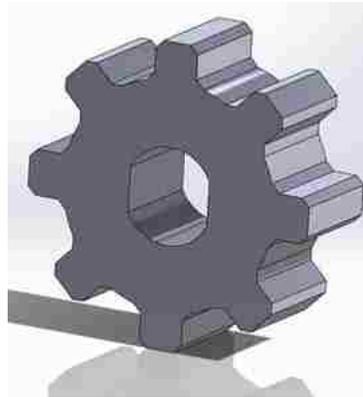
Figure 4. The spur gear used in the first case study.
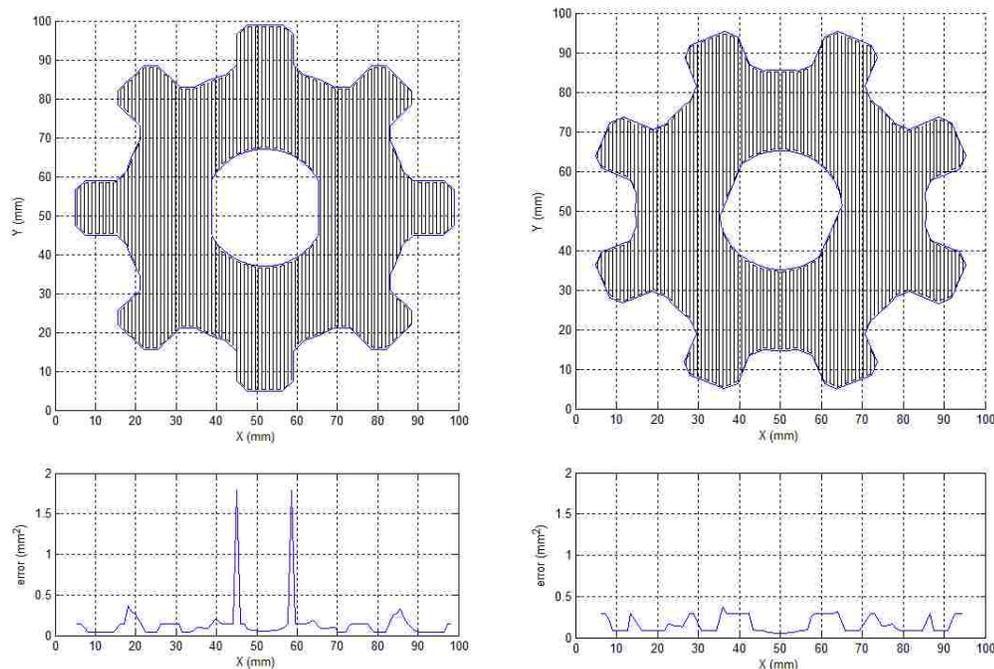
Figure 5. Original (left) versus optimal (right) rastering orientation along with error values for a layer of the spur gear. In the right picture, the orientation of the "part" is the same as the left picture and the rastering direction is changed by 157.47° CW. However, for convenience in illustrating the error diagram, the picture is drawn as if the part is rotated 157.47° CCW.
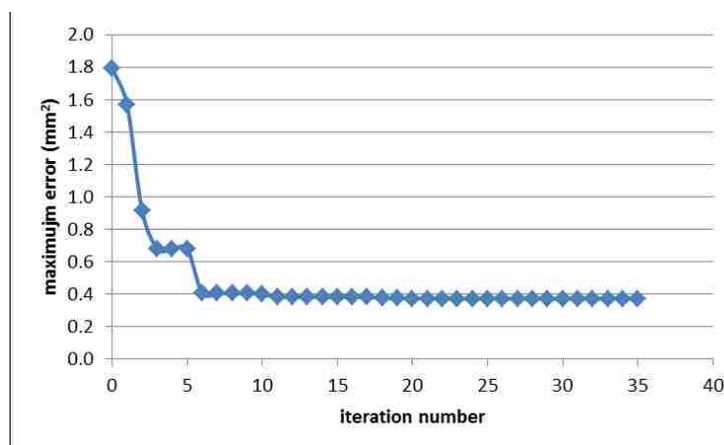
Figure 6. Maximum error versus. number of iterations for a layer of the spur gear.

5.2. LINER BLOCK

A liner block with embedded sensors is considered in the second case study. Figure 7 shows the liner block with two vertical and two horizontal cavities for sensors. Figures 8-11 show how efficacious the optimal rastering orientation is in reducing the horizontal staircase effect for representative layers of the liner block. In all figures, the orientation of the "part" in the right picture is the same as that in the left picture and rastering direction is changed CW. However, for convenience in illustrating the error diagram, the picture is drawn as if the part is rotated CCW.
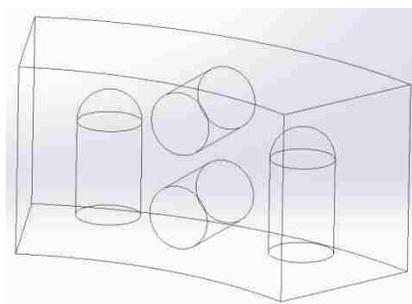
Figure 7. Liner block with two vertical and two horizontal cavities for sensors used as the second case study.

Table 2 compares the error values between the original orientation and the optimal orientation for those representative layers as well as the entire part. The original rastering orientation results in a maximum error of 1.396 mm^2 for all layers, whereas optimal orientations reduce these errors to 0.269, 0.254, 0.269 and 0.143 mm^2 for 10th, 30th, 50th and 70th layer, respectively.
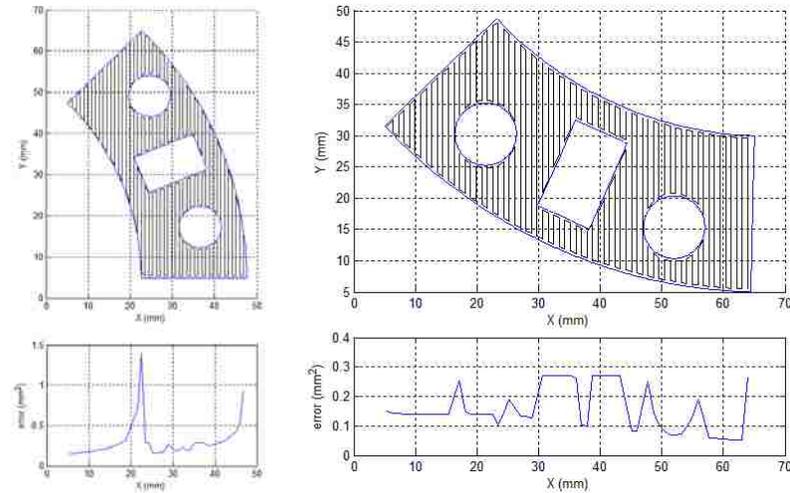
Figure 8. Original (left) versus optimal (right) rastering orientation along with error values for 10th layer of liner block. Optimum rastering orientation is 223.37° CW.
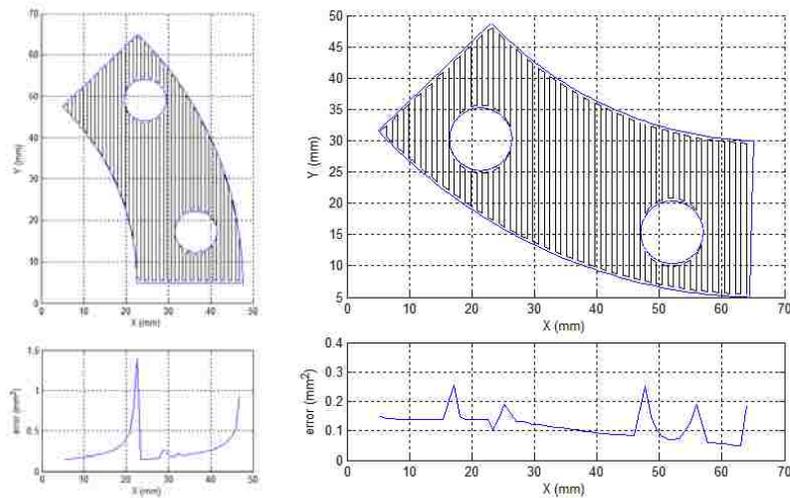
Figure 9. Original (left) versus optimal (right) rastering orientation along with error values for 30th layer of liner block. Optimum rastering orientation is 223.39° CW.

The liner blocks were built using a freeform extrusion fabrication process at different orientations as illustrated in Figure 12. In the top two pictures, large staircase errors can be visually observed for both horizontal and vertical cavities. These errors might affect the performance of the embedded sensors. In the bottom pictures, the errors are reduced by choosing suitable rastering orientations.
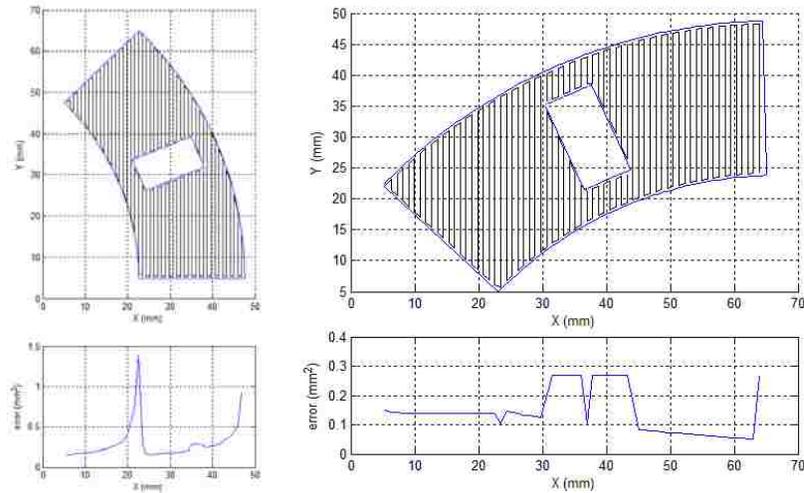
Figure 10. Original (left) versus optimal (right) rastering orientation along with error values for 50th layer of liner block. Optimum rastering orientation is 91.63° CW.
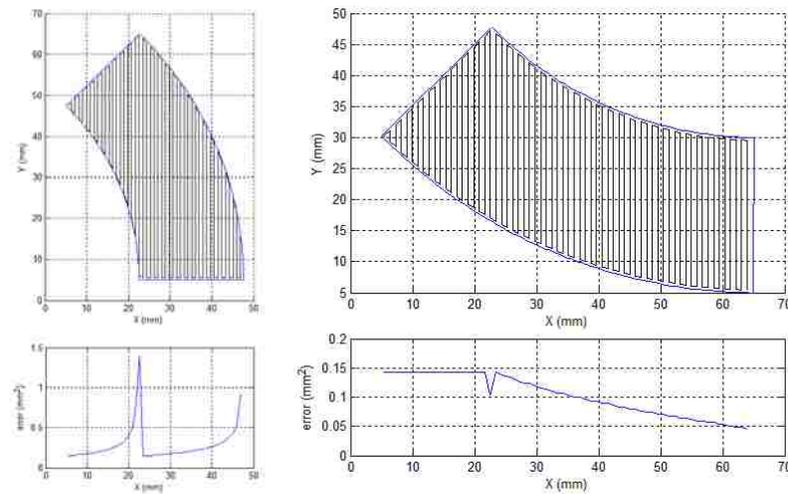
Figure 11. Original (left) versus optimal (right) rastering orientation along with error values for 70th layer of liner block. Optimum rastering orientation is 224.68° CW.

Table 2. Maximum errors of representative layers of liner block in original and optimal rastering directions.

Layer no.	Original orientation	Original error (mm^2)	Optimal orientation	Optimal error (mm^2)	Reduction (%)
10	0°	1.396	223.37°	0.269	**80.7**
30	0°	1.396	223.39°	0.254	**81.8**
50	0°	1.396	91.63°	0.269	**80.7**
70	0°	1.396	224.68°	0.143	**89.8**
Entire part	0°	1.396	223.37°	0.269	**80.7**

Figure 12. Liner blocks fabricated at different rastering angles.

6. SUMMARY AND CONCLUSIONS

The horizontal staircase effect, resulting from approximating a complex layer boundary and its interior by cuboid lines, was considered in this paper. An area deviation criterion was developed to estimate this effect for every line of a layer for an arbitrary object. It was then demonstrated that the direction of the lines has a significant influence on horizontal errors. Therefore, a derivative-free optimization method was utilized to determine the optimum orientation of rasters for each layer of a part to minimize the error.

Two cases were studied to investigate the efficacy of the proposed approach. In the first case, optimizing the rastering orientation of a spur gear resulted in a 79.4% reduction in maximum error. A liner block with embedded sensors was examined next. Depending on the geometry of each layer, the maximum errors were reduced between 80.7 to 89.8%. This part was also printed at various orientations using a freeform extrusion fabrication process.

According to the results, it could be concluded that the proposed approach is effective in reducing the horizontal staircase errors without altering any other

performance factors such as the vertical errors, fabrication time, amount of support material, and number of layers.

ACKNOWLEDGEMENTS

REFERENCES

[1]   I. Gibson, D. W. Rosen, and B. Stucker, *Additive Manufacturing Technologies*. Springer, 2010.

[2]   W. Cheng, J. Y. H. Fuh, A. Y. C. Nee, Y. S. Wong, H. T. Loh, and T. Miyajawa, "Multi-objective optimization of part-building orientation in stereolithography," *Rapid Prototyp. J.*, vol. 1, no. 4, pp. 12–23, 1995.

[3]   P. Alexander, S. Allen, and D. Dutta, "Part orientation and build cost determination in layered manufacturing," *Comput. Aided Des.*, vol. 30, no. 5, pp. 343–356, 1998.

[4]   K. Thrimurthulu, P. M. Pandey, and N. V. Reddy, "Optimum part deposition orientation in fused deposition modeling," *Int. J. Mach. Tools Manuf.*, vol. 44, no. 6, pp. 585–594, 2004.

[5]   V. Canellidis, J. Giannatsis, and V. Dedoussis, "Genetic-algorithm-based multi-objective optimization of the build orientation in stereolithography," *Int. J. Adv. Manuf. Technol.*, vol. 45, no. 7–8, pp. 714–730, 2009.

[6]   A. M. Phatak and S. S. Pande, "Optimum part orientation in Rapid Prototyping using genetic algorithm," *J. Manuf. Syst.*, vol. 31, no. 4, pp. 395–402, 2012.

[7]   R. Paul and S. Anand, "Optimal part orientation in Rapid Manufacturing process for achieving geometric tolerances," *J. Manuf. Syst.*, vol. 30, no. 4, pp. 214–222, 2011.

[8]   R. Paul and S. Anand, "Optimization of layered manufacturing process for reducing form errors with minimal support structures," *J. Manuf. Syst.*, 2014.

[9]   J. Kennedy and R. C. Eberhart, "Particle Swarm Optimization," in *IEEE International Conference on Neural Networks*, 1995, pp. 1942–1948.

[10]   S. S. Rao, *Engineering optimization: theory and practice*, 4th ed. John Wiley & Sons, 2009.

VI. COMPOSITION OPTIMIZATION FOR FUNCTIONALLY GRADIENT PARTS CONSIDERING MANUFACTURING CONSTRAINTS[1]

ABSTRACT

Being able to design and fabricate parts made of Functionally Gradient Materials (FGMs) with optimum properties is of prime importance. Very limited research has been carried out thus far regarding the optimization of composition of different constituent materials throughout the part. In this paper, a technique is introduced to maximize the stiffness of parts made of FGM by determining the material composition for each small element inside the part. To demonstrate the effectiveness of this technique, two examples are examined. In the first one, a two dimensional cantilever beam made of two materials is considered and a Sequential Approximate Optimization method is used to determine the optimum composition of materials for the beam so that the global stiffness is maximized. The only applied force on the beam is a nodal force acting at the tip. One of the constituent materials is stiffer and heavier than the other material. The optimization constraint is the total mass of the beam predetermined by the engineer. The problem is how to distribute materials throughout the beam so as to have the maximum stiffness. The second example is a simply supported beam under a uniform pressure. The same methodology is employed for this example to maximize the stiffness of the beam. The results show a considerable increase in the stiffness of the beams after optimization as compared to the beams with uniformly distributed materials. Additive Manufacturing (AM) methods that are capable of fabricating the designed parts and their constraints are also discussed.

1. INTRODUCTION

Functionally Gradient Materials (FGMs) are a type of composite materials made of two or more constituent materials with a continuously variable composition. FGMs are gaining more applications in industry because of their enhanced properties which may

---

[1] This paper was published in proceedings of the *ASME 2014 Manufacturing Science and Engineering Conference*, pp. 1-6, 2014.

include higher stiffness, resistance to thermal loads, improved residual stress distribution, or a combination of these favorable properties. Their main applications include situations where the designer needs different material properties at different locations in a single part, especially when continuous variations are desirable. For example, consider a lathe cutting tool at the tip of which high resistivity to elevated temperatures is required whereas at the shank high mechanical strength is desirable. A solution to this problem is to gradually vary the material composition from ceramic at the tip to metal at the shank. Numerous papers have dealt with various aspects of FGMs, and a paper by Birman and Byrd [1] provided a comprehensive review. Because of diverse applications of these materials, being able to design and fabricate parts made of FGMs with optimum properties is of prime importance. There are numerous papers in the literature about approaches to homogenization of FGMs, their responses to mechanical and thermal loads, testing methods and manufacturing aspects. However, very limited research has been carried out regarding the optimization of composition of different constituent materials throughout the part. In what follows, a review of literature regarding optimization of material composition is provided.

Huang et al. [2] optimized the composition of materials inside a flywheel in the radial direction. They used a bi-objective optimization algorithm to simultaneously maximize the kinetic energy stored in the wheel and minimize the maximum equivalent stress. They have also optimized the geometry by determining the thickness at 20 points. Silva and Paulino [3] and Paulino and Silva [4] assumed that the part is composed of a material with position-dependent properties (which changes exponentially and is not optimized). The topology optimization based on the Solid Isotropic Material with Penalization (SIMP) model was used to determine the optimum geometry of the beam to minimize the compliance, thus they have optimized the topology of a beam made of FGMs. Stump et al. [5] considered problems with mechanical loads and used Sequential Linear Programming to minimize the volumetric density of one material in a functionally gradient part made of two materials. The constraint was the maximum admissible stress and the Von Mises failure criterion was employed. In one of their examples, a 2D turbine blade made of two fictitious materials (one representing a ceramic and another representing an alloy) with a given geometry and three mechanical loads (two uniform

pressures and the centrifugal load) was considered. The amount of ceramic material was minimized considering the admissible stress. Wang and Wang [6] applied a complex variational method to minimize strain energy in 2D rectangular beams by assigning various materials to different locations. Although several materials have been used, they are not mixed together but rather form separate regions. Goupee and Vel [7] employed a real-coded Genetic Algorithm (GA) to find the 2D optimum material composition for functionally gradient plates under thermal loads. Two example problems were solved: In the first problem (a simply supported three-layered Ni-Al_2O_3 plate), they minimized the peak residual stress when the functionally gradient component was cooled from a high fabrication temperature. In the second problem (with Al-ZrO_2 composition), the goal was to minimize the mass of the beam with constraints on the peak effective stress and maximum temperature experienced by the metal. In [8], teeth made of HAP/Col (ceramic) and titanium under applied chewing forces were considered. The objectives were to maximize the densities of cortical and cancellous bones while minimizing the vertical displacement. The material gradient was only in the vertical direction and governed by a power law. Na and Kim [9] assumed a simple power law for material distribution which varied only in the z direction. The problem was about a 3D panel composed of ZrO_2 and Ti–6Al–4V, which underwent a sinusoidal mechanical load distributed over the top surface of the model and a temperature variation was also applied on the same side. The objectives were to minimize the maximum stress while maximizing the critical temperature which would result in thermo-mechanical buckling. Xu et al. [10] modeled a cylinder with two materials and used the Evolutionary Structural Optimization algorithm to optimize the material distribution (in the radial direction only) in order to reach a uniform stress distribution . Chiba and Sugano [11] optimized the material composition of an infinite functionally gradient plate made of Ti and ZrO_2 in only one direction using a genetic algorithm. The plate was exposed to different temperatures at top and bottom and the goal was to minimize the stress. Kou et al. [12] utilized Particle Swarm Optimization (PSO) to optimize 1D and 2D material distribution of parts exposed to temperature variations. The objective of optimization was to simultaneously minimize the Von Mises stress and the mass of a plate made of zirconia (ZrO_2) and titanium alloy (Ti-6Al-4V).

Most previous research only considered thermal stresses resulted from variations in temperature, and there is a paucity of work considering mechanical loads and resultant strains. In these papers, a pre-specified region of the part (e.g., upper surface of a plate) was made of ceramic and another pre-specified region (e.g., the lower surface) was made of metal, and the purpose of optimization was to interpolate the material composition between these two regions. However, if the sole purpose of designing these parts is tolerating thermal loads, there is no point in using FGMs and homogeneous ceramic parts could be utilized. Thus, mechanical loads should also be taken into account to have a more realistic problem to deal with. Also, as explained above, in those few papers that considered mechanical loads to optimize the material composition distribution, the objective was to reduce the stresses and usually a simple model for material distribution was assumed (either one dimensional or using an analytical equation). Additionally, manufacturing constraints have not been taken into account in previous research efforts on material composition optimization. While FGM may serve as an excellent optimization and material tailoring tool, the ability to incorporate optimization techniques and solutions in practical design depend on the capacity to manufacture these materials to required specifications. Conventional techniques are often incapable of adequately addressing this issue [1].

In the present paper, maximizing the stiffness of a part with functionally gradient materials is considered and a technique is proposed to determine the optimum material composition for each element inside the part using a Sequential Approximate Optimization (SAO) method. To illustrate the method, the composition of a 2D cantilever beam and a simply supported beam made of an FGM by mixing two materials at various proportions at different locations is optimized. A nodal force is applied at the tip of the cantilever beam and the simply supported beam is under a uniform pressure. For both cases, the objective is to have the maximum stiffness and the optimization constraint is the total mass of the beam, which is kept at a constant value. Thus, the total amount of each material is known and the problem is how to distribute these materials throughout the beam so as to have the maximum stiffness. Also, a suitable manufacturing method for fabrication of the designed parts is proposed and the required design constraints are discussed.

2. MATERIAL MODELING

In order to find the effective material properties for the mixture of two materials, several methods could be used. The most common ones are explained below.

The linear rule of mixture [13] is a simple and common estimate to find the effective properties for a two-phase material presented in eq. (1).

$$X^{ab} = \rho^a X^a + \rho^b X^b \tag{1}$$

where superscripts "*a*" and "*b*" indicate material types, ρ is the volumetric fraction of each material and X is the property. Here it is assumed that there is no porosity and thus $\rho^a + \rho^b = 1$.

The Effective Medium Theory (EMT) [14] is suitable for 2D composites consisting of a matrix containing randomly overlapping circular inclusions, where both the matrix and inclusion phases are isotropic elastic materials.

The Maxwell model assumes a dispersion of small particles within a continuous matrix phase and the particles being far apart from each other so that the local distortions to the transport characteristics around each particle do not interfere with their neighbors [15].

The reciprocity model [16] is based on the assumption that by reciprocating the volume fraction of the two materials in the composite, the microstructure remains statistically equivalent.

In this paper, the linear rule of mixture is utilized because of its simplicity and prevalence.

3. FINITE ELEMENT ANALYSIS

An FEA code capable of analyzing functionally gradient parts with various loads using Constant Strain Triangular (CST) elements has been developed in MATLAB. The code consists of five functions: "Input" function that reads the data from a text file and assigns the appropriate value to each variable (the input data include the total mass of the beam and its dimensions, mesh size, density, Young's modulus and Poisson's ratio for each material, mechanical constraints and loads); "Assemble" function which calculates the stiffness matrix and assembles the local matrices to find the global stiffness matrix of the beam; "Loading" function that obtains the final force vector based on nodal forces

and traction forces; "Solving" function which applies the constraints and solves the system of equations to determine the displacements, strains, stresses and reaction forces; Finally, "Showing" function shows the results.

A CST element (shown in Fig. 1) has 3 nodes each of which having 2 degrees of freedom (because of the 2D nature of the problem, each node can move in x and y directions and has two degrees of freedom).
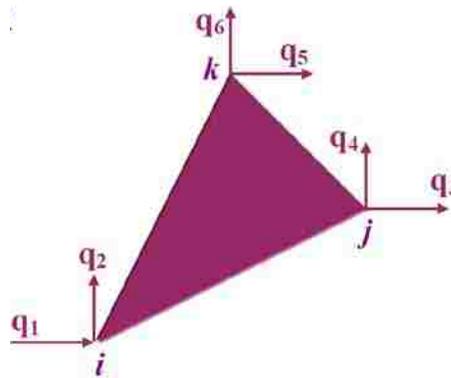
Figure 1. A CST element and its degrees of freedom.

The FEA approach for obtaining stresses and strains of parts made of this element type is explained briefly here and the reader can refer to [17] for more detailed information.

The shape functions for this element type are:

$$N_i = \frac{1}{2A_{ijk}} \left\| x_j y_k - x_k y_j \quad y_{jk} x - x_{jk} y \right\| \tag{2a}$$

$$N_j = \frac{1}{2A_{ijk}} \left\| x_k y_i - x_i y_k \quad y_{ki} x - x_{ki} y \right\| \tag{2b}$$

$$N_k = \frac{1}{2A_{ijk}} \left\| x_i y_j - x_j y_i \quad y_{ij} x - x_{ij} y \right\| \tag{2c}$$

$$N = \left\| \begin{matrix} N_i & 0 & N_j & 0 & N_k & 0 \\ 0 & N_i & 0 & N_j & 0 & N_k \end{matrix} \right\| \tag{2d}$$

where A_{ijk} is the area of the element and $x_{ij} = x_i - x_j$.

The stiffness matrix is obtained using

$$K = \int_V B^T D B \, dV \tag{3}$$

where *V* is the volume of the element, *B*-matrix is calculated by taking derivatives of *N* with respect to x and y:

$$B = \begin{bmatrix} \frac{\partial N_1}{\partial x} & 0 & \frac{\partial N_2}{\partial x} & 0 & \frac{\partial N_3}{\partial x} & 0 \\ 0 & \frac{\partial N_1}{\partial y} & 0 & \frac{\partial N_2}{\partial y} & 0 & \frac{\partial N_3}{\partial y} \\ \frac{\partial N_1}{\partial y} & \frac{\partial N_1}{\partial x} & \frac{\partial N_2}{\partial y} & \frac{\partial N_2}{\partial x} & \frac{\partial N_3}{\partial y} & \frac{\partial N_3}{\partial x} \end{bmatrix} \tag{4}$$

and for the plane-stress condition *D* is determined according to the following formula:

$$D = \frac{E}{1-v^2} \begin{bmatrix} 1 & v & 0 \\ v & 1 & 0 \\ 0 & 0 & (1-v)/2 \end{bmatrix} \tag{5}$$

in which, *E* is the Young's modulus and *v* is the Poisson's ratio.

After extracting the stiffness matrix of each element, the matrices are assembled together to form the global stiffness matrix. Then, the boundary conditions are applied and a simultaneous system of linear equations is solved to find the displacement of each node. After obtaining displacements, strains and stresses can be easily calculated. It is noted that the dimensions of the elements are determined considering the manufacturing constraints discussed in the following sections.

4. OPTIMIZATION ALGORITHM

The objective of the optimization is to determine the composition of materials inside each element so that the stiffness is maximized. An initial uniform distribution of material (all elements have the same volume fraction of material "a" and "b") is assumed and corresponding displacements resulted from applied loads are calculated by the FEA code explained in the previous section. Maximizing the stiffness is equivalent to minimizing the total compliance defined by the following equation:

$$c = U^T K U = \sum_{e=1}^{N} u_e^T k_e(\rho_e) u_e \tag{6}$$

where U is the total displacement vector containing the horizontal and vertical displacements of each node, K^{Gl} is the global stiffness matrix, u_i is the displacement vector for each element and t is the thickness of the beam. Accordingly, c is a real valued parameter which is a function of volumetric fraction and the objective of the optimization procedure is to minimize c in a way that the total mass remains constant. Thus, the number of variables to be optimized is equal to the number of elements. In each iteration the value of compliance is obtained and the optimization algorithm determines the material composition inside each element for the next step using the results of the current step. This procedure is repeated until the optimum material composition is obtained and the compliance is minimized (i.e., the stiffness is maximized).

Since the number of variables is very large, it is of prime importance to choose a suitable optimization algorithm to avoid prolonged CPU time. On the other hand, the form of objective function is not given explicitly in terms of design variables and rather is obtained by FEA which is considerably time consuming. In such problems, to make the number of analyses as few as possible, a Sequential Approximate Optimization (SAO) method is an appropriate option to consider. The reader is referred to [18] for more information about this optimization algorithm.

The constrained optimization problem to be solved using the SAO is stated as follows:

$$
\begin{aligned}
&\min c(\rho^a) \\
&s.t.\, M(\rho^a) = M_0 \\
&0 \le \rho_i^a \le 1
\end{aligned}
\tag{7}
$$

where M is the total mass of the beam and ρ^a is the volumetric fraction matrix of material "a" which is composed of volumetric fractions of individual elements (ρ_i^a). Note that since $\rho^a + \rho^b = 1$, all functions depend on ρ^a only.

The general updating scheme for the volumetric fraction matrix as suggested by SAO is presented in eqs. (8) and (9).

$$
\tag{8}
$$

$$\text{(9)}$$

where λ is calculated in each iteration step such that the mass constraint is satisfied and the derivatives are calculated using the following equations:

$$\text{(10)}$$

$$\text{(11)}$$

where d is the density.

Thus, the following procedure is carried out to find the optimum composition:

1. Read the input data (material properties, boundary conditions, etc.).
2. Assign an initial uniform distribution and calculate compliance using the FEA code.
3. Find the new volumetric fractions using the optimization algorithm.
4. Repeat the second step with new values for volumetric fractions and the third step until the change in compliance is negligible.

5. NUMERICAL EXAMPLE

The first illustrative example is a two-dimensional cantilever beam composed of 7075 aluminum alloy and aluminum oxide (Al_2O_3) at the tip of which a nodal force is applied. The mechanical properties of these materials are given in Table 1. The dimensions of the beam are 100 mm in length, 20 mm in width and 1 mm in height and it is assumed that the total mass cannot exceed 6.5 grams (this mass constraint is equivalent

to setting a maximum value of 38.6% for the **total** volume fraction of alumina). The problem is to minimize the beam's compliance for a given mass of the beam; i.e. the question is: what is the composition distribution that results in the stiffest structure made of two materials (note that alumina is stiffer but heavier than A7075)?

Table 1. Mechanical properties of constituent materials.

	Alumina	A7075
Density (g/cm^3)	3.95	2.81
Young's modulus (GPa)	380	73
Poisson's ratio	0.22	0.33

The optimal composition of material obtained is shown in Fig. 2, where the values correspond to volumetric fraction of alumina. This optimal distribution of material results in 39.6% increase in stiffness of the optimized beam compared to the case where there is a uniform distribution of material in the beam.
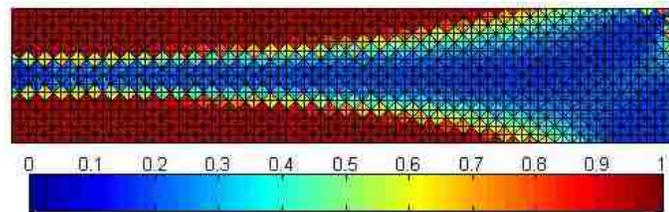
Figure 2. Optimum material distribution for a cantilever beam composed of two materials at the tip of which a nodal force is applied (the numbers on the legend correspond to volumetric fraction of stiffer material).

The second example is a simply supported beam made of the same materials as the first example and the same geometry. The mass constraint is also 6.5 grams and the objective is to determine material composition distribution to have maximum stiffness. The optimal composition of material obtained is shown in Fig. 3, where the values correspond to volumetric fraction of alumina. This optimal distribution of material results in 33.9% increase in stiffness of the optimized beam compared to the case where there is a uniform distribution of material in the beam.
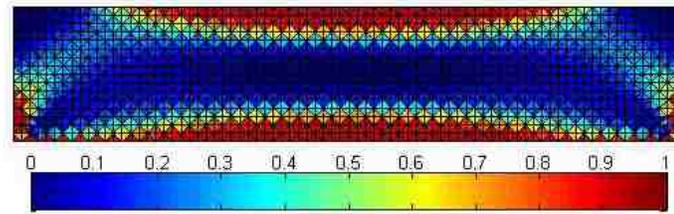
Figure 3. Optimum material distribution for a simply supported beam composed of two materials under a uniform pressure (the numbers on the legend correspond to volumetric fraction of stiffer material).

6. FABRICATION METHOD AND CONSTRAINTS

AM processes that can deliver different materials (usually through multiple feeding units) to the building areas have the ability to fabricate functionally gradient components, which is a primary advantage of AM technology that conventional methods cannot realize. In this section, AM methods capable of fabricating the designed functionally gradient part are discussed based on a recent review paper by Guo and Leu [19]. Then, one of these processes is proposed for fabricating the designed beam and several considerations about this process are taken into account.

As a powder deposition process, Laser Metal Deposition (LMD) [20], also known as Laser Engineered Net Shaping (LENS), is an AM process in which the metal powder is completely melted by a laser beam, resulting in fully dense parts without the need for post processing. LMD/LENS has the ability to vary the degree of material composition, leading to a functionally gradient part by feeding different material powders from multiple nozzles.

Several ceramic actuators and sensors with novel properties have been fabricated using a variant Fused Deposition Modeling (FDM) process developed by Jafari et al. [21]. The modified system has multiple deposition units and the ability to deposit up to four different types of materials in any given layer.

The Freeze-form Extrusion Fabrication (FEF) process [22] involves computer control of flows of aqueous pastes (each controlled separately), the mixing of these pastes, and the extrusion of the mixed paste to fabricate a 3D part layer-by-layer. Two or more pastes are extruded simultaneously by a multi-extruder mechanism. Continuous control over the material compositions and their gradients during the part fabrication

process can be achieved by planning (with time delay taken into consideration) and controlling the relative flow rates of the different pastes. As an example, assuming that two cylinders containing two different pastes have the same cross-sectional area, a desired paste mixture consisting of 20% paste "a" and 80% paste "b" (in volume percentage) can be achieved by controlling the two plunger velocities with the ratios of v1:v2 = 2:8, where v1 and v2 are the plunger velocities for pastes "a" and "b", respectively. The FEF process is proposed to fabricate the designed part.

The major constraints in fabricating the optimally designed functionally gradient beam are: the capabilities of the motors and controllers to follow the desired velocity profile (it is not possible to change the velocity of the motor abruptly and sudden changes in material composition should be avoided in design); the mixer might not be able to mix the pastes homogeneously and some undesired variations in composition will remain in the fabricated part; the diameter of the nozzle determines the minimum size of representative elements (i.e. the resolution of variations in material composition corresponds to the nozzle size; obviously, a smaller nozzle will result in higher resolution).

7. CONCLUSIONS

The material composition distribution of functionally gradient parts is optimized to achieve the stiffest structure for a given mass using a Sequential Approximate Optimization method. The numerical examples consist of a cantilever beam made of alumina and A7075 aluminum alloy with a nodal force applied at its tip and a simply supported beam under a uniform pressure. The results of optimization show a considerable increase in stiffness of the beams, demonstrating that the presented method has significant value for design and production of functionally gradient parts.

REFERENCES

[1]   Birman, V. and L.W. Byrd, *Modeling and Analysis of Functionally Graded Materials and Structures.* Applied Mechanics Reviews, 2007. **60**: p. 195-216.

[2]   Huang, J, G.M. Fadel, V.Y. Blouin and M. Grujicic, *Bi-objective optimization design of functionally gradient materials.* Materials and Design, 2002. **23**: p. 657–666.

[3]   Silva, E.C.N. and G.H. Paulino, *Topology optimization applied to the design of functionally graded material (FGM) structures*, in *XXI ICTAM*. 2004: Warsaw, Poland. p. 15-21.

[4]   Paulino, G.H. and E.C.N. Silva, *Design of Functionally Graded Structures Using Topology Optimization.* Materials Science Forum, 2005. **492-493**: p. 435-440.

[5]   Stump, F.V., E.C. Silva, and G.H. Paulino, *Optimization of material distribution in functionally graded structures with stress constraints.* Commun. Numer. Meth. Engng, 2007. **23**: p. 535–551.

[6]   Wang, M.Y. and X. Wang, *A level-set based variational method for design and optimization of heterogeneous objects.* Computer-Aided Design, 2005. **37**: p. 321–337.

[7]   Goupee, A.J. and S.S. Vel, *Two-dimensional optimization of material composition of functionally graded materials using meshless analyses and a genetic algorithm.* Comput. Methods Appl. Mech. Engrg, 2006. **195**: p. 5926–5948.

[8]   Lin, D., Q. Li, W. Li, S. Zhoua and M.V. Swain, *Design optimization of functionally graded dental implant for bone remodeling.* Composites: Part B, 2009. **40**: p. 668–675.

[9]   Na, K.S. and J.H. Kim, *Volume fraction optimization of functionally graded composite panels for stress reduction and critical temperature.* Finite Elements in Analysis and Design, 2009. **45**: p. 845-851.

[10]   XU, A., Y. Qu, Y. Yang and N.E. Mastorakis, *Topological Customization for Materials Composition of 3D Heterogeneous Multi-Functional Components*, in *8th WSEAS International Conference on Applied Computer and Applied Computational Science*. 2009.

[11]   Chiba, R. and Y. Sugano, *Optimisation of material composition of functionally graded materials based on multiscale thermoelastic analysis.* Acta Mech, 2012. **223,**: p. 891–909.

[12]   Kou, X.Y., G.T. Parks, and S.T. Tan, *Optimal design of functionally graded materials using a procedural model and particle swarm optimization.* Computer-Aided Design, 2012. **44**: p. 300–310.

[13]   Reddy, J.N. and C.D. Chin, *Thermomechanical analysis of functionally graded cylinders and plates.* J. Therm. Stresses, 1998. **21**: p. 593-626.

[14]   Snyder, K.A., E.J. Garboczi, and A.R. Day, *The elastic moduli of simple two-dimensional isotropic composites: Computer simulation and effective medium theory.* Journal of Applied Physics, 1992. **72**(12): p. 5948–5955.

[15]   Wang, M. and N. Pan, *Predictions of effective physical properties of complex multiphase materials.* 2008.

[16]   Mendelson, K.S., *A theorem on the effective conductivity of a two-dimensional heterogeneous medium.* Journal of Applied Physics, 1975. **46**(11): p. 4740–4741.

[17]   Desai, Y.M., T.I. Eldho, and A.H. Shah, *Finite Element Method with applications in engineering*. 2011: Dorling Kindersley.

[18]   Nakayama, H., Y. Yun, and M. Yoon, *Sequential Approximate Multiobjective Optimization Using Computational Intelligence*. Vector Optimization. 2009, Verlag Berlin Heidelberg: Springer.

[19]   Guo, N. and M.C. Leu, *Additive manufacturing: technology, applications and research needs.* 2013.

[20]   Balla, V.K., P.D. DeVasConCellos, W. Xue, S. Bose and A. Bandyopadhyay, *Fabrication of compositionally and structurally graded Ti-TiO2 structures using laser engineered net shaping (LENS).* Acta Biomaterialia, 2009. **5**(5): p. 1831–1837.

[21]   Jafari, M.A., W. Han, F. Mohammadi, A. Safari, S.C. Danforth and N. Langrana, *A novel system for fused deposition of advanced multiple ceramics.* Rapid Prototyping Journal, 2000. **6**(3): p. 161–175.

[22]   Leu, M.C., B.K. Deuser, L. Tang, R.G. Landers, G.E. Hilmas and J.L. Watts, *Freeze-form extrusion fabrication of functionally graded materials.* CIRP Annals - Manufacturing Technology, 2012. **61**: p. 223–226.

VII. A GENERIC METHODOLOGY FOR OPTIMAL DESIGN OF THREE-DIMENSIONAL FUNCTIONALLY GRADED MATERIALS CONSIDERING ADDITIVE MANUFACTURING CONSTRAINTS[1]

ABSTRACT

Although some conventional manufacturing technologies are capable of producing Functionally Graded Materials (FGMs), only a few additive manufacturing processes are able to build FGMs with complex distribution of material composition. To exploit this unique advantage of these processes, we have developed a methodology capable of optimizing the distribution of material composition for one-, two-, and three-dimensional parts for any given conditions. Mori-Tanaka model was employed to predict the behavior of FGM; a new technique was developed to represent material composition distribution by extending the NURBS surfaces to four-dimensional space; subroutines were developed in commercial finite element software to enable implementation of FGM; and a constrained particle swarm optimization method was selected and implemented to optimize the material composition distribution. Two case studies were conducted to examine the efficacy of the proposed methodology. The results indicated that the optimal parts outperformed the non-optimal parts to a great extent.

Keywords: Constrained particle swarm optimization; Functionally gradient material; 3D printing; Abaqus; Heterogeneous material.

1. INTRODUCTION

Functionally Graded Materials (FGM) are a type of composite materials made of two or more constituent phases with a continuously changing phase distribution throughout the volume. Typically, constituent phases are two materials with distinct thermo-mechanical properties, the volume fraction of each of which changes gradually throughout the part. There are numerous papers in the literature about approaches to homogenization of FGMs, their responses to mechanical and thermal loads, testing methods and manufacturing aspects. However, very limited research has been carried out regarding the optimization of composition of different constituent materials throughout

---

[1] This paper is intended for submission to *Materials and Design* journal.

the part. In what follows, a review of literature regarding optimization of material composition is provided.

Wang and Wang [1] applied a complex variational method to minimize strain energy in two-dimensional rectangular beams by assigning various materials to different locations. Although several materials have been used, they are not mixed together but rather form separate regions. Goupee and Vel [2] employed a real-coded genetic algorithm to find the two-dimensional optimum material composition for functionally graded plates under thermal loads. Two example problems were solved: In the first problem (a simply supported three-layered Ni-Al2O3 plate), they minimized the peak residual stress when the functionally graded component was cooled from a high fabrication temperature. In the second problem (with Al-ZrO2 composition), the goal was to minimize the mass of the beam with constraints on the peak effective stress and maximum temperature experienced by the metal. Lin et al. [3] considered human teeth made of HAP/Col (ceramic) and titanium under applied chewing forces and maximized the densities of cortical and cancellous bones while minimizing the vertical displacement. The material gradient was only in the vertical direction and governed by a power law. Na and Kim [4] assumed a simple power law for material distribution which varied only in the z direction. The problem was about a three-dimensional panel composed of ZrO2 and Ti–6Al–4V, which underwent a sinusoidal mechanical load distributed over the top surface of the model and a temperature variation was also applied on the same side. The objectives were to minimize the maximum stress while maximizing the critical temperature which would result in thermo-mechanical buckling. Xu et al. [5] modeled a cylinder with two materials and used the evolutionary structural optimization algorithm to optimize the material distribution (in the radial direction only) in order to reach a uniform stress distribution. Chiba and Sugano [6] optimized the material composition of an infinite functionally graded plate made of Ti and ZrO2 in only one direction using a genetic algorithm. The plate was exposed to different temperatures at top and bottom and the goal was to minimize the stress. Kou et al. [7] optimized one- and two-dimensional material distribution of parts exposed to temperature variations. The objective of optimization was to simultaneously minimize the Von Mises stress and the mass of a plate made of zirconia (ZrO_2) and a titanium alloy (Ti-6Al-4V). Ghazanfari and Leu [8]

used a sequential approximate optimization method to maximize the stiffness of beams with two-dimensional material distribution. Zhang et al. [9] proposed a framework to achieve an optimal material composition for different objective functions using a Monte Carlo-based and a gradient descend-based optimizer. They were also able to convert the continuous material distribution to discrete distribution for viable manufacturing.

Most previous researchers only considered thermal stresses resulted from variations in temperature, and there is a paucity of work considering mechanical loads and resultant strains. They were also typically not able to handle realistic material models and used a simple rule of mixture to estimate the properties of FGM. Furthermore, no paper was found in the literature addressing optimization of material composition distribution in three dimensions. Furthermore, most previous methods either assumed a one-dimensional material gradient or used an analytical equation with a few constants to represent the distribution of material composition. Additionally, manufacturing constraints were not taken into account in previous research efforts.

The current paper presents a generic and versatile methodology for optimal design of FGM, addresses the above-mentioned challenges facing previous research and handles manufacturing constraints. A reliable material model was selected and implemented to predict the properties of FGM. A new material representation technique was proposed which, among other advantages, reduces the number of variables in the optimization procedure. A commercial Finite Element Analysis (FEA) software was modified so that FGMs could be analyzed and problems with complex physics could be solved. Finally, a derivative-free optimization method capable of handling any objective function and constraint was implemented to optimize the material composition distribution iteratively.

2. MODELING THE MATERIAL BEHAVIOR

Many researchers have proposed various models to predict the effective properties of a composite material, including elastic moduli, electrical and thermal conductivity, diffusion coefficient, and coefficient of thermal expansion. These models are based on properties of each constituent phase, and size, shape, orientation, and concentration of these phases. A comprehensive review on these models was published by Torquato [10].

Mori-Tanaka method is one of the most commonly used models in the recent research [11]. Weng [12] obtained the closed form of Mori-Tanaka equations [13] for the case of spherical reinforcements. Based on this model, the effective Bulk Modulus, K_e, and the effective Shear Modulus, G_e, could be obtained according to Equation (1):

$$K_e = K_1\left(1 + \frac{a}{1 - \gamma_m a}\right), \qquad G_e = G_1\left(1 + \frac{b}{1 - \beta_m b}\right)$$ (1),

where

$$a = \frac{f_2(K_2 - K_1)}{\gamma_m(K_2 - K_1) + K_1}, \qquad b = \frac{f_2(G_2 - G_1)}{\beta_m(G_2 - G_1) + G_1}$$ (2),

and a and b are calculated from Equation (3):

$$\gamma_m = \frac{3K_1}{3K_1 + 4G_1}, \qquad \beta_m = \frac{G_1(9K_1 + 2G_1)}{5(3K_1 + 4G_1)}$$ (3),

where f_i, K_i, and G_i are volume fraction, Bulk Modulus, and Shear Modulus of phase i, respectively. Thus, having properties of each material, one could calculate the effective properties for any composition (clearly, at each point, $f_1 + f_2 = 1$).

A cross-property relation is one due to Levin [14] that links the effective thermal expansion coefficient, α_e, to the effective bulk modulus, K_e. Levin showed that for a two-phase composite,

$$\alpha_e = f_1\alpha_1 + f_2\alpha_2 + \frac{\alpha_2 - \alpha_1}{\frac{1}{K_1} - \frac{1}{K_2}}\left(\frac{1}{K_e} - \left(\frac{f_1}{K_1} + \frac{f_2}{K_2}\right)\right)$$ (4),

where α_i is the coefficient of thermal expansion of phase i. Thus, having coefficients of thermal expansion of each material, one could implement K_e from Equation (1) into Equation (4) and calculate the effective thermal expansion coefficient for any composition.

It is noted that although Mori-Tanaka and Levin's models were used in this study, any other simplified or advanced model could easily be implemented without affecting other parts of the proposed framework.

3. REPRESENTATION OF MATERIAL DISTRIBUTION

For one- or two-dimensional problems with a small number of elements, the finite element mesh could be used to represent the material distribution. In this case, each element could potentially have a specific volume fraction of each constituent phase. Thus, the number of variables in the optimization problem becomes equal to the number of elements in the finite element mesh. Clearly, for large problems, this approach is not pragmatic and results in prolonged computational time. In the current study, to reduce the number of variables and to guarantee a smooth transition in material composition, we developed a new representation technique based on Non-Uniform Rational Basis Spline (NURBS) curves and surfaces.

For a one-dimensional problem (e.g., optimization of material distribution along the length of a cantilever beam), the volumetric fraction of material 1, f_1, can change between 0 and 1 along the longitudinal direction of the part according to

$$f_1(u) = \frac{\sum_{i=0}^{n} f_{1,i} h_i N_{i,k}(u)}{\sum_{i=0}^{n} h_i N_{i,k}(u)} \tag{5}$$

where u corresponds to the position along the length; there are $n+1$ control points the composition at each of which is $f_{1,i}$; h_i is the weight of each point, and $N_{i,k}$ are the basis functions obtained from the following equation:

$$N_{i,k}(u) = \frac{(u - t_i) N_{i,k-1}(u)}{t_{i+k-1} - t_i} + \frac{(t_{i+k} - u) N_{i+1,k-1}(u)}{t_{i+k} - t_{i+1}}$$

$$N_{i,1}(u) = \begin{cases} 1 & \text{if } t_i \leq u < t_{i+1} \\ 0 & \text{otherwise} \end{cases} \tag{6}$$

where t_i is the parametric knot value. Uniform knot vectors were used in this study. More details about NURBS could be found in [15].

Thus, if the volumetric fraction of one material is known at control points, the composition at each point can be determined using Equation (5). Then, material properties are obtained for each point from Equations (1) and (4).

For a two-dimensional material distribution, similar to one-dimensional problems, the material composition could be represented by a two-dimensional NURBS surface in a three-dimensional space where the dimensions are x and y-coordinates of the points in the part, and the third dimension is the material composition at each point inside the part.

Similar to one-dimensional problems, the volumetric fraction of material 1, f_1, can change between 0 and 1 throughout the part according to

$$f_1\left(u, u'\right) = \frac{\sum_{i=0}^{n} \sum_{i'=0}^{n'} f_{1,ii'} A_{ii'} N_{i,k}(u) N_{i',k'}(u')}{\sum_{i=0}^{n} \sum_{i'=0}^{n'} A_{ii'} N_{i,k}(u) N_{i',k'}(u')}$$ (7),

where u and u' correspond to the x and y-coordinates and there are $(n+1)(n'+1)$ control points the composition at each of which is $f_{1,ii'}$. Again, once the composition at the control points are known, the composition at all other points can be obtained followed by calculation of material properties.

As a very simple illustrative example, the material distribution in a two-dimensional part is shown in Figure 1. There is a gradual transition from one material at the center to another material at the boundary of the part according to a fourth-order NURBS surface with 25 control points uniformly distributed inside the part.
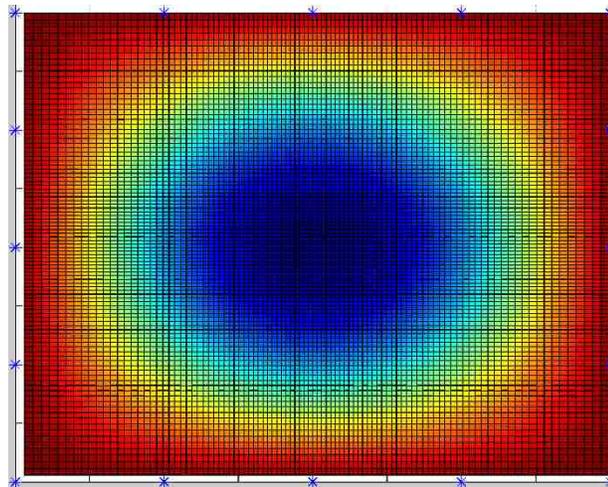
Figure 1. A very simple illustrative example showing how material composition gradually changes from one material at the center to another material at the boundary according to a NURBS surface using 25 control points.

For three-dimensional parts, including those with a complex geometry, we extended the NURBS surfaces to four-dimensional space where the dimensions are x, y and z-coordinates of the points in the part, and the fourth dimension is the material composition at each point inside the part. The volumetric fraction of material 1, f_1, can change between 0 and 1 throughout the part according to

$$f_1(u, u', u'') = \sum \sum \sum f_{1,ii'i''} \, N_{i}(u) \, N_{i'}(u') \, N_{i''}(u'')$$ (8),

where u, u' and u'' correspond to the x, y and z-coordinates and there are $(n+1)(n'+1)(n''+1)$ control points the composition at each of which is $f_{1,ii'i''}$. Again, once the composition at the control points are known, the composition at all other points can be obtained followed by calculation of material properties. The position of control points can be chosen either manually or automatically. It should also be noted that NURBS surfaces in four-dimensional spaces have also been used in medical imaging research to develop a realistic phantom for the cardiac motion [16].

4. FINITE ELEMENT ANALYSIS

To benefit from the wide range of finite element analyses provided by the advanced commercial software, Abaqus 6.14, we wrote a subroutine enabling implementation of FGM in Abaqus/Standard. The USDFLD function in Abaqus/Standard provides users with the capability of defining field variables as functions of time or other quantities [17]. Our codes enabled Abaqus to vary the material properties within a part according to the output of the *Material Representation Function* explained in Section 4. These codes include a Fortran code written using USDFLD function which enables implementation of FGM in Abaqus/Standard, and a Matlab code which prepares the Abaqus input file (*.inp* file) for analysis.

To check the accuracy of implementation of FGM in Abaqus/Standard, a very simple example problem was solved analytically and the results were compared against the result of finite element simulation. A cantilever Euler-Bernoulli beam with a nodal force, F, acting at its tip (at $x=l$) was considered and it was assumed that the Young's modulus changes linearly from E_1 at one end ($x=0$) to E_2 at the other end ($x=l$). The general equation describing beam deflection, w, is (see e.g., [18] for an explanation of this equation):

$$\frac{d^2 w(x)}{dx^2} = \frac{M(x)}{E(x) I(x)}$$ (9),

where x is the position along the longitudinal direction of the beam, M is the bending moment and I is the area moment of inertia of the cross-section. For simplicity, I was assumed to be constant throughout the beam. Substituting for M and E in Equation (9) results in Equation (10):

$$\frac{d^2 w(x)}{dx^2} = \frac{F(l-x)}{(E_1 + (E_2 - E_1)x/l)I} \tag{10}$$

The two boundary conditions required to solve the above differential equation are:

$$@x=0: w'(x)=0, \ w(x)=0 \tag{11}$$

After integrating Equation (10) and applying boundary conditions, the deflection equation was obtained:

$$w(x) = \ldots \tag{12}$$

where

$$\ldots \tag{13}$$

Assuming a beam-width of 0.1 m, a height of 0.1, a length of 1 m, a force of 10 kN, and Young's moduli of $E_1=200$ GPa and $E_2=400$ GPa, the deflection at the tip of the beam is $w=1.636$ mm.

Modeling the same problem in Abaqus using 10,000 linear brick elements with reduced integration (C3D8R) resulted in a maximum deflection of 1.639 mm. This clearly indicates the successful implementation of FGM in Abaqus. Details of modeling for each sample problem in the Abaqus/CAE environment are explained in Section 7, Numerical Examples.

5. OPTIMIZATION ALGORITHM

5.1. CONSTRAINED PARTICLE SWARM OPTIMIZATION

Kennedy and Eberhart [19] introduced the Particle Swarm Optimization (PSO) method, which is an evolutionary computational technique based on swarm intelligence. In this method, each candidate solution to the optimization problem is considered as the trajectory of a particle and is adjusted in the search space based on the experience of its own as well as other particles in the swarm. It is assumed that there are N particles in the swarm and the particles can move in a D-dimensional search space. The set of parameters in the ith iteration are represented by the position vector of the jth particle, $X_j^i = (x_{j1}^i, x_{j2}^i, \ldots, x_{jD}^i)$, and changes in the parameters are represented by the velocity of the particle, $V_j^i = (v_{j1}^i, v_{j2}^i, \ldots, v_{jD}^i)$. Initially, the N particles are randomly distributed in the space and finally all of them will reach the optimal point.

The key step in PSO is calculating the velocity of each particle at each iteration. This velocity depends on the previous velocity of the particle, the historical best value for the particle, and the historical best value of all particles as follows:

$$V_j^i = \theta V_j^{i-1} + c_1 r_1 \| P_{best,j} - X_j^{i-1} \| + c_2 r_2 \| G_{best} - X_j^{i-1} \| \tag{14},$$

where $P_{best,j}$ is the position of jth particle corresponding to the best value of the objective function encountered by this particle in all the previous iterations; G_{best} is the position of the particle experiencing the best value of the objective function encountered in the previous iterations by any of the N particles; c_1 and c_2 are the cognitive (individual) and social (group) learning rates, respectively; r_1 and r_2 are uniformly distributed random numbers in the range 0 to 1; and θ is known as the inertial weight and is calculated by

$$\theta = \theta_{max} - \left(\frac{\theta_{max} - \theta_{min}}{i_{max}} \right) i \tag{15},$$

where θ_{max} and θ_{min} are the initial and final values of the inertia weight, respectively, and i_{max} is the maximum number of iterations. The values of $\theta_{max} = 0.9$ and $\theta_{min} = 0.4$ are commonly used [20].

Having the velocities of all particles, the position of each particle is

$$x_i^k = x_i^{k-1} + v_i^k$$ (16).

This iterative procedure continues until a convergence criterion is met (e.g., the difference between the global best fitness of the last two iterations is smaller than a certain value, or the global best fitness does not change after a certain number of iterations).

Similar to other stochastic optimization methods, the PSO algorithm is originally defined for unconstrained problems. Perez and Behdinan [21] proposed a parameter-less adaptive penalty scheme to accommodate the inclusion of constraints in PSO. Their scheme uses the swarm information, such as the average of the objective function and the level of violation of each constraint during each iteration, in order to define different penalties for different constraints. The original objective function is replaced by

$$F''(X) = \begin{cases} F(X) & \text{if } X \text{ is feasible,} \\ F(X) + \sum_{k=1}^{m} \lambda_k G_k(X) & \text{otherwise,} \end{cases}$$ (17),

$$\lambda_k = |\overline{F(X)}| \frac{\overline{G_k(X)}}{\sum_{k=1}^{m} [\overline{G_k(X)}]^2}$$

where $F(X)$ is the original objective function, m is the number of constraints, $G_i(X)$ is a specific constraint value (with violated constraints having values larger than zero), $\overline{F(X)}$ is the average of the original objective function values in the current swarm, and $\overline{G_k(X)}$ is the violation of the lth constraint averaged over the current population.

Note that other derivative-free optimization algorithms such as genetic algorithms, simulated annealing, ant colony optimization, fuzzy optimization, and neural-network-based methods may also be used to determine the optimum material composition distribution.

5.2. IMPLEMENTATION

In the current study, X is a vector containing volumetric fractions (i.e., material composition) of material one, f_1, at all the control points. Thus, the number of variables in the optimization problem is equal to the number of control points. The objective

function(s) is/are the results of FEA (e.g., maximum stress, natural frequencies, and maximum displacement) or any user-defined function (e.g., cost and mass). The constraints can also be either the results of FEA (e.g., failure stress) or any user-defined function (e.g., maximum mass and material composition at certain locations).

For any given problem, the optimization process starts with an initial guess for the material composition at control points. The initial population can be generated either randomly or by user. The *Material Representation Function* then generates the material composition distribution throughout the part. In the next step, the finite element problem is submitted to Abaqus. Once the analysis is complete, the results are read by a Matlab code from the *.dat* file generated by Abaqus. The optimization algorithm then generates the next iteration based on analysis results and this process continues until the material distribution is optimized.

5.3. CONSIDERING MANUFACTURING CONSTRAINTS

Several Additive Manufacturing techniques such as Inkjet Printing, PolyJet Technology, Stereolithography, Ultrasonic Consolidation, Metal Deposition, and Extrusion-based processes have been utilized thus far to produce parts made of multiple materials. A comprehensive review on multiple material additive manufacturing was recently published by Vaezi et al. [22]. However, only PolyJet Technology and Extrusion-based processes are capable of continuously changing the material composition along all directions and produce complex FGMs. Here, we focus on Extrusion-based processes.

Extrusion-based additive manufacturing of FGM (e.g., Freeze-form Extrusion Fabrication [23] and Ceramic On-Demand Extrusion [24]) involves computer control of flows of each material, the mixing of these materials, and the extrusion of the mixed material to fabricate a three-dimensional part layer-by-layer. Two or more materials are extruded simultaneously by a multi-extruder mechanism. Continuous control over the material compositions and their gradients during the part fabrication process can be achieved by planning (with time delay taken into consideration) and controlling the relative flow rates of the different materials.

The major constraint in fabricating the optimally designed functionally gradient parts using the extrusion-based processes is the capability of the extrusion mechanisms to follow the desired velocity profiles; i.e., it is not possible to change the velocity of the extrusion abruptly, and sudden changes in material composition should be avoided in design. This limitation was modeled in the optimization procedure as a constraint. The maximum allowable difference of volumetric fractions of material 1, Δf_1, between any two adjacent points was set as a constraint in the optimization procedure using Equation (17).

6. NUMERICAL EXAMPLES

6.1. SUMMARY OF PROPOSED METHODOLOGY

As shown in Figure 2, the procedure starts with an initial guess for the material composition at control points. The NURBS surface generator, a function written using Matlab, produces the material composition for all other points in the part based on the initial guess. Having the composition at each point, the material modeling function calculates the material properties at each point according to their composition. Another function, also written in Matlab environment, generates the FEA input file (i.e., *.inp* file for Abaqus solver), implements the material properties, and runs the Abaqus solver. The results of the FEA are read from the output file (*.dat* file) and fed to the optimization algorithm. Based on the result of each particle, the optimization algorithm generates the next iteration and the procedure continues until the optimality criterion is met.

6.2. TWO-DIMENSIONAL THERMAL PROBLEM

A two-dimensional rectangular functionally graded part made of two materials was considered in this example. The length and width of the plate were 20 cm and its thickness was assumed 1 cm. The composition gradually transitioned from alumina at the center of the part to zirconia at its surface. The objective was to reduce residual stresses caused by a 1000 °C temperature change. A fourth-order NURBS surface with 25 control points was used to generate the material distribution and a four-node bilinear plane strain element with reduced integration (CPE4R) was employed in FEA. Properties of alumina

and partially stabilized zirconia are given in Table 1. Bulk and Shear moduli were calculated from Equations (18) and (19).
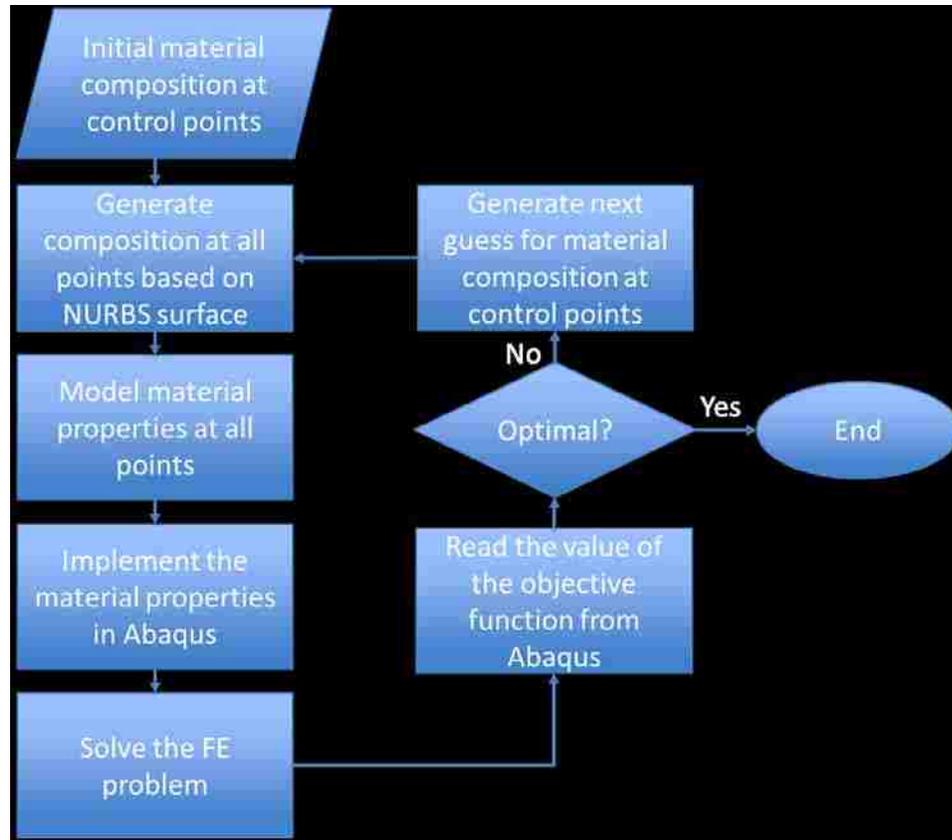
Figure 2. Flowchart of the proposed methodology.

$$K_i = \frac{E_i}{3(1-2v_i)} \qquad G_i = \frac{E_i}{2(1+v_i)} \tag{18},$$

where E_i is the Young's modulus and v_i is the Poisson's ratio. The calculated values were implemented in Equation (1) to obtain the effective Bulk and Shear moduli at each point inside the part. Finally, the effective Young's modulus and Poisson's ratio were calculated at each point from Equation (19):

$$E = \frac{9K_v G_v}{3K_v + G_v} \qquad v = \frac{3K_v - 2G_v}{2(3K_v + G_v)} \tag{19}.$$

To obtain the effective coefficient of thermal expansion at each point, Equation (4) was used.

Due to the symmetry of the problem, only a quarter of the part was modeled in Abaqus. The initial distribution of material composition and the resulting stress field are shown in Figure 3. As can be seen in the figure, there was a gradual transition from alumina at the center of the part to zirconia at the surface. Due to the smaller coefficient of thermal expansion of alumina, the maximum tensile stress was observed at the center of the part with highest concentration of alumina. The maximum principal stress for the initial distribution of material composition was 303 MPa.

Figure 4 shows the optimum distribution of material composition for this problem resulting in the minimum stress. The maximum principal stress was reduced from 303 MPa to 173 MPa during the optimization process, which clearly indicated the efficacy of the proposed methodology.

Table 1. Properties of constituent materials.

	Alumina	Zirconia
Young's modulus (E)	400 GPa	200 GPa
Poisson's ratio (v)	0.21	0.25
Coefficient of thermal expansion (α)	7×10^{-6} °C^{-1}	10^{-5} °C^{-1}
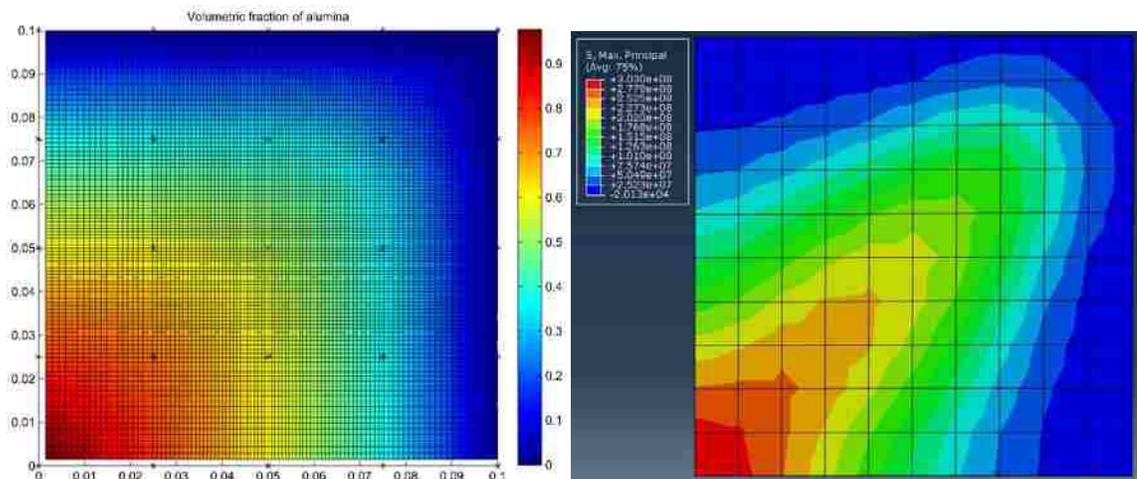
Figure 3. Initial material distribution and the resulting stress field for a two-dimensional problem.

6.3. THREE-DIMENSIONAL THERMO-MECHANICAL PROBLEM

As an industrial example, a three-dimensional smart lining block in a gasification chamber was considered. The dimensions of the block are shown in Figure 5. To monitor the pressure and temperature in a gasification chamber, a novel approach is embedding sensors in the lining blocks during their fabrication process [25]. The sensors are located inside a zirconia tube and the main body of the lining block is made from alumina. In order to reduce the stresses caused by a mismatch between coefficients of thermal expansion of zirconia and alumina, it is desirable to have a gradual transition from zirconia at the center of the block to alumina at its surface.
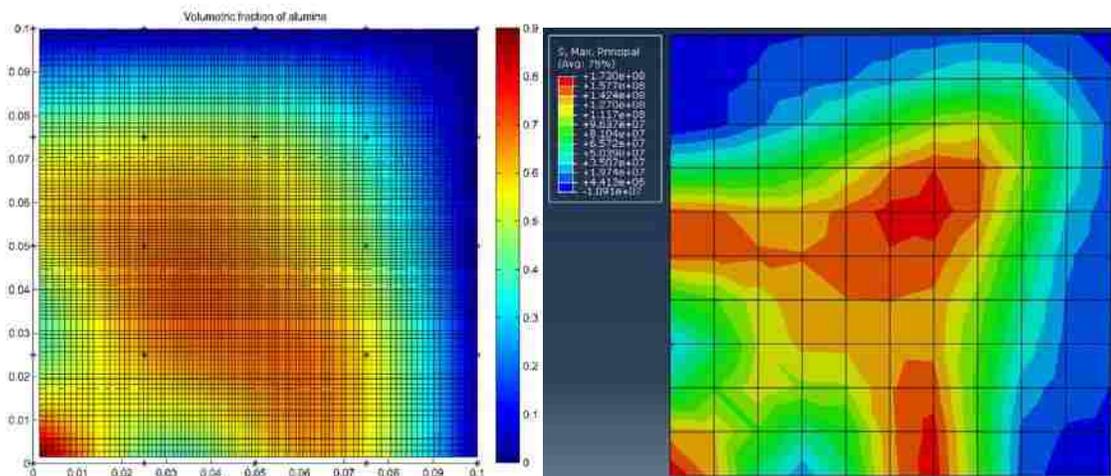
Figure 4. Optimum material distribution and the resulting stress field for a two-dimensional problem.
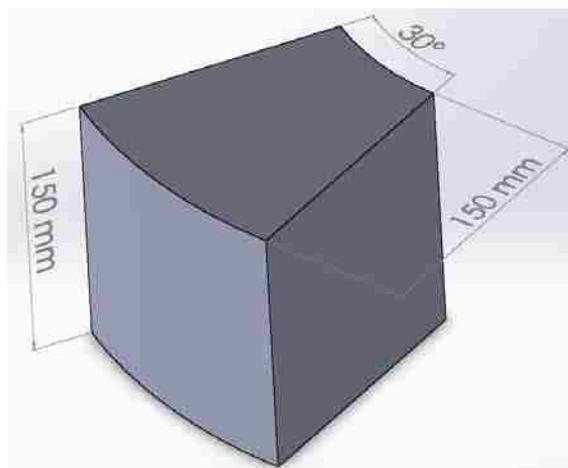
Figure 5. Dimensions of the lining block.

The smart lining block experiences two different types of loads, a pure thermal load resulted from cooling down from sintering temperature to room temperature (assumed to be 850 °C), and a combination of thermal and mechanical loads during working condition. The internal pressure of the chamber was 85 MPa and its temperature was 400 °C. Both of these loads were considered in the optimization problem and the objective was to minimize the maximum principal stress.

A three-dimensional NURBS surface in four-dimensional space with 64 control points (4 points in each direction) was used to generate the material distribution for one quarter of the part (due to symmetry). An eight-node continuum three-dimensional element with reduced integration (C3D8R) was employed in FEA. Initially, a simple smooth transition in the material composition was implemented manually. The resulting maximum principal stress was 289.6 MPa that occurred during the pure thermal load resulted from cooling down from sintering temperature to room temperature. The maximum principal stress field is shown in Figure 6. The optimization algorithm was able to reduce this stress to 195.3 MPa after 20 iterations. Figure 7 shows distribution of principal stresses in the lining block with optimum material composition.
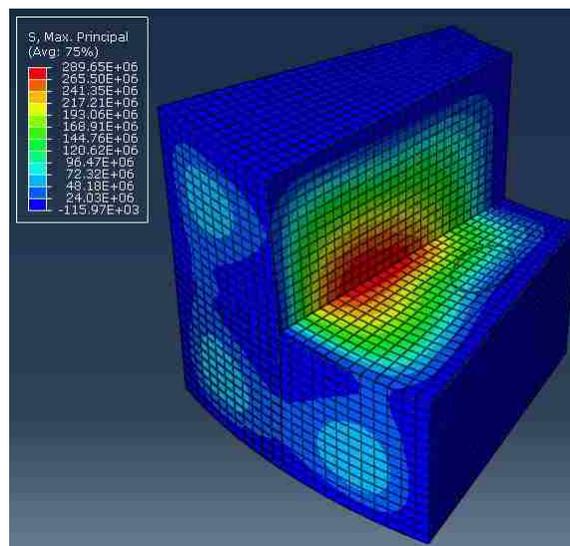
Figure 6. Principal stress distribution in a lining block before the optimization procedure.
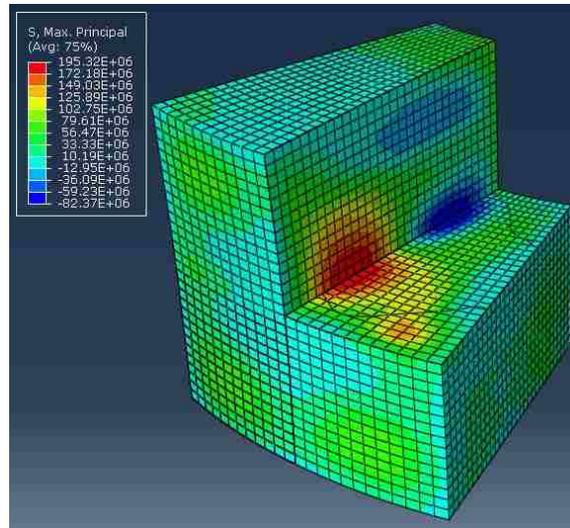
Figure 7. Principal stress distribution in a lining block with optimum material composition.

6.4. THREE-DIMENSIONAL DYNAMIC PROBLEM

To examine the efficacy of the proposed methodology in dynamic problems, a three-dimensional Reaction Wheel was considered. Reaction Wheels are used in satellites as an attitude control actuator. While their mass needs to be as low as possible, their moment of inertia and first natural frequency should be large. A functionally graded wheel with a radius of 10 cm composed of alumina and aluminum was modeled using ten-node tetrahedral elements (C3D10). Due to the symmetry of the problem, only a quarter of the part was modeled in Abaqus. Material properties are given in Table 2.

Table 2. Properties of constituent materials in the third example problem.

	Alumina	Aluminum
Young's modulus (E)	400 GPa	73 GPa
Poisson's ratio (v)	0.21	0.33
Density (ρ)	3950 kg/m^3	2810 kg/m^3

The following bi-objective constrained optimization problem was implemented to maximize the first natural frequency and moment of inertia while maintaining a constant mass:

$$\text{subject to} \quad \frac{I}{I_0} \geq 1, \quad \frac{\omega^2}{\omega_0^2} \geq 1$$

(20),

where I is the moment of inertia, ω is the first natural frequency, and M is the mass of the wheel. For a homogeneous wheel with a mass of 0.3 kg, I_0 and ω_0 were found to be 1.98×10^{-3} kgm^2 and 5964 rad/s, respectively. The first mode shape of the wheel is shown in Figure 8. The optimization algorithm was able to increase these values to 2.30×10^{-3} kgm^2 and 6841 rad/s in 50 iterations.
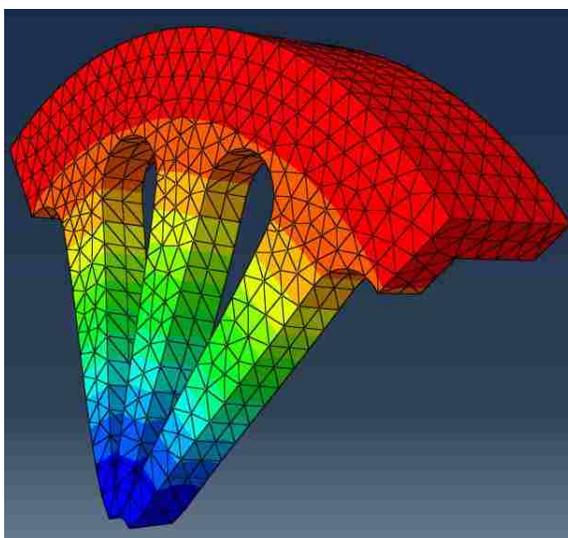
Figure 8. The first mode shape of a quarter Reaction Wheel.

7. CONCLUSIONS

To exploit the capabilities of additive manufacturing technologies in producing functionally graded materials with complex material distribution, a methodology was developed in this study to optimize the distribution of material composition for functionally graded parts. In the two case studies conducted, more than 35% reduction in the maximum stress was observed as a result of optimizing the material composition distribution. The advantages of the proposed methodology include:

- Providing flexibility in incorporating any material model for predicting the behavior of functionally graded parts,

- Capability of handling complex material distributions and three-dimensional geometries,
- Analysis of multi-physics problems (e.g., dynamic, thermo-mechanical, thermo-fluid, electromagnetic, and thermal-electrical-structural problems),
- Feasibility of considering any objective function for optimization, and
- Capability of handling constraints including manufacturing constraints and desired material at any location.

ACKNOWLEDGEMENTS

REFERENCES

[1]   M.Y. Wang, X. Wang, A level-set based variational method for design and optimization of heterogeneous objects, Comput. Des. 37 (2005) 321–337.

[2]   A.J. Goupee, S.S. Vel, Two-dimensional optimization of material composition of functionally graded materials using meshless analyses and a genetic algorithm, Comput. Methods Appl. Mech. Engrg. 195 (2006) 5926–5948.

[3]   D. Lin, Q. Li, W. Li, S. Zhoua, M. V Swain, Design optimization of functionally graded dental implant for bone remodeling, Compos. Part B. 40 (2009) 668–675.

[4]   K.S. Na, J.H. Kim, Volume fraction optimization of functionally graded composite panels for stress reduction and critical temperature, Finite Elem. Anal. Des. 45 (2009) 845–851.

[5]   A. Xu, Y. Qu, Y. Yang, N.E. Mastorakis, Topological Customization for Materials Composition of 3D Heterogeneous Multi-Functional Components, in: 8th WSEAS Int. Conf. Appl. Comput. Appl. Comput. Sci., 2009.

[6]   R. Chiba, Y. Sugano, Optimisation of material composition of functionally graded materials based on multiscale thermoelastic analysis, Acta Mech. 223, (2012) 891–909.

[7]   X.Y. Kou, G.T. Parks, S.T. Tan, Optimal design of functionally graded materials using a procedural model and particle swarm optimization, Comput. Des. 44 (2012) 300–310.

[8]   A. Ghazanfari, M.C. Leu, Composition optimization for functionally gradient parts considering manufacturing constraints, in: ASME 2014 Int. Manuf. Sci. Eng. Conf., Detroit, Michigan, USA, 2014: pp. 1–6.

[9]   F. Zhang, C. Zhou, S. Das, An efficient design optimization method for functional gradient material objects based on finite element analysis, in: Proc. ASME 2015 Int. Des. Eng. Tech. Conf. Comput. Inf. Eng. Conf. (IDETC/CIE 2015), ASME, Boston, MA, USA, 2015.

[10]   S. Torquato, Random Heterogeneous Materials: Microstructure and Macroscopic Properties, 1st ed., Springer Science+Business Media, LLC, New York, 2002. doi:10.1007/978-1-4757-6355-3.

[11]   V. Birman, L.W. Byrd, Modeling and analysis of functionally graded materials and structures, Appl. Mech. Rev. 60 (2007) 195–216.

[12]   G.J. Weng, Some elastic properties of reinforced solids, with special reference to isotropic ones containing spherical inclusions, Int. J. Eng. Sci. 22 (1984) 845–856.

[13]   T. Mori, K. Tanaka, Average stress in matrix and average elastic energy of materials with misfitting inclusions, Acta Metall. 21 (1973) 571–574. doi:10.1016/0001-6160(73)90064-3.

[14]   V.M. Levin, Thermal expansion coefficients of heterogeneous materials, Mech. Solids. 21 (1967) 9–17.

[15]   I. Zeid, NURBS, in: Mastering CAD/CAM, Tata McGraw-Hill, New Delhi, 2005: pp. 323–344.

[16]   W.P. Segars, D.S. Lalush, E.C. Frey, D. Manocha, M.A. King, B.M.W. Tsui, Improved dynamic cardiac phantom based on 4D NURBS and tagged MRI, IEEE Trans. Nucl. Sci. 56 (2009) 2728–2738. doi:10.1109/TNS.2009.2016196.

[17]   Abaqus 6.14 user subroutines reference guide, Dessault Systems, 2014.

[18]   M.H. Sadd, Elasticity: theory, applications, and numerics, second edi, Elsevier, Burlington, MA, USA, 2009.

[19]   J. Kennedy, R.C. Eberhart, Particle swarm optimization, in: IEEE Int. Conf. Neural Networks, Perth, Australia, 1995: pp. 1942–1948.

[20]   S.S. Rao, Engineering optimization: theory and practice, 4th ed., John Wiley & Sons, 2009.

[21]   R.E. Perez, K. Behdinan, Particle swarm approach for structural design optimization, Comput. Struct. 85 (2007) 1579–1588. doi:10.1016/j.compstruc.2006.10.013.

[22] M. Vaezi, S. Chianrabutra, B. Mellor, S. Yang, Multiple material additive manufacturing – Part 1: a review, Virtual Phys. Prototyp. 8 (2013) 19–50. doi:10.1080/17452759.2013.778175.

[23] M.C. Leu, B.K. Deuser, L. Tang, R.G. Landers, G.E. Hilmas, J.L. Watts, Freeze-form extrusion fabrication of functionally graded materials, CIRP Ann. - Manuf. Technol. 61 (2012) 223–226. doi:10.1016/j.cirp.2012.03.050.

[24] A. Ghazanfari, W. Li, M.C. Leu, G.E. Hilmas, A novel freeform extrusion fabrication process for producing solid ceramic components with uniform layered radiation drying, Addit. Manuf. 15 (2017) 102–112. doi:http://dx.doi.org/10.1016/j.addma.2017.04.001.

[25] A. Ghazanfari, W. Li, M.C. Leu, Y. Zhuang, J. Huang, Advanced ceramic components with embedded sapphire optical fiber sensors for high temperature applications, Mater. Des. 112 (2016) 197–206. doi:10.1016/j.matdes.2016.09.074.

VIII. ADVANCED CERAMIC COMPONENTS WITH EMBEDDED SAPPHIRE OPTICAL FIBER SENSORS FOR HIGH TEMPERATURE APPLICATIONS[1]

ABSTRACT

This paper describes an extrusion-based additive manufacturing process that has been developed to enable embedment of sapphire optical fiber sensors in ceramic components during the part fabrication. In this process, an aqueous paste of ceramic particles is extruded through a moving nozzle to build the part layer-by-layer. In the case of sensor embedment, the fabrication process is halted after a certain number of layers have been deposited; the sensors are placed in their predetermined locations, and the remaining layers are deposited until the part fabrication is completed. Because the sensors are embedded during the fabrication process, they are fully integrated with the part and the problems of traditional sensor embedment can be eliminated. Scanning electron microscopy was used to observe the embedded sensors and to detect any possible flaws in the part or embedded sensor. Attenuation of the sensors was measured in near-infrared region (1500-1600 nm wavelength). Standard test methods were employed to examine the effect of embedded fibers on the strength and hardness of the parts. The results indicated that the sapphire fiber sensors with diameters smaller than 250 micrometers were able to endure the freeform extrusion fabrication process and the post-processing without compromising the part properties.

1. INTRODUCTION

Embedded sensors have been widely used in structural health monitoring and proven very effective in civil and structural engineering [1,2]. However, there are currently no viable techniques for in-situ monitoring of the health status of the critical components in energy production systems. In addition, the existing techniques for process monitoring are inadequate to operate reliably in the extremely harsh environments over a long time [3]. The sensing capabilities can be incorporated in the design phase of various energy systems by embedding sensors into the critical

---

[1] This paper was published in *Materials and Design* journal, vol. 112, pp. 197-206, 2016.

components, enabling a new paradigm in harsh-environment sensing. The embedded sensors not only provide the real-time information on the health status of the component, but also reduce the complexity in sensor installation and increase the robustness of the sensors for reliable measurements of various parameters that are important for system control and optimization.

Embedded sensors are conventionally attached to or mounted on the component after the structure is fabricated. Several embedment techniques for strain sensors have been proposed in the literature [4–10]. However, these techniques could result in an unsecured sensor attachment, offsets between the sensor readings and the actual status of the structure, potential performance degradation of the host materials or structures, and relative slip at the interface of the matrix and sensor encapsulation [11–15]. For strain measurements, in most cases, the strain sensitivity of an embedded sensor is significantly different from that of the bare sensor [2]. In harsh environments, the sensors are either surface mounted far from critical locations to avoid interference with the operation of the structures, or destructively inserted into the critical locations through appropriate channels in the structures, making it difficult to provide measurements with a high spatial and temporal resolution [16]. Additive manufacturing (AM) is potentially a promising method that could be employed to embed the sensors into the host structure during the component fabrication. This allows secured sensor placement, enhances the survivability, improves the measurement accuracy and reliability, and preserves the structural integrity of the parts.

AM has been recently exploited to embed fibers, sensors or other components in parts to enhance the properties of parts (e.g., strengthen them) or produce smart components. Most of the research in this area is based on ultrasonic consolidation (UC) or ultrasonic additive manufacturing (UAM) process. Janaki et al. [17] used this process to embed SiC fibers and stainless wire meshes in an Al 3003 matrix and produced fiber-reinforced metal matrix composites. Li et al. [18] embedded fiber Bragg gratings (FBG) in metal foil using UC processes and investigated the embedding process, cross-sections of welded samples, the form change and wavelength shift of the Bragg peak during the processes, and the sensing characteristics of the embedded FBGs. Maier et al. [19] embedded optical fiber sensors incorporating FBGs in a polymeric component made by

the selective laser sintering process. Dapino [20] also used UC to fabricate Galfenol beams for adaptive vibration absorbers, NiTi/Al composites for zero coefficient of thermal expansion applications, and structures with embedded cooling channels. Monaghan et al. [21] exploited UC to integrate optical fibers equipped with metallic coatings into solid aluminum matrices. They also characterized the inter-laminar and fiber/matrix interfaces and examined their bonding strength. In another paper [22], they embedded three dielectric materials into aluminum metal-matrices produced by the UC process and investigated the effect of the dielectric material hardness on the final metal matrix mechanical strength. Kousiatza and Karalekas [23] embedded FGBs in thermoplastic parts during their fabrication process in a fused deposition modeling system for in-situ and real-time monitoring of strain fields and temperature profiles as the parts were being built.

Because of their high melting point and excellent resistance to oxidation, chemical attack and erosion, advanced ceramics are the best candidates for host materials in harsh and corrosive environments of energy production systems. Several AM techniques have been developed or modified to fabricate three-dimensional ceramic components, including 3D printing, ink-jet printing, selective laser sintering, stereolithography, laminated object manufacturing, and extrusion-based techniques (mainly fused deposition of ceramics, robocasting, and freeze-form extrusion fabrication). All of these techniques involve adding ceramic materials layer by layer. A comprehensive review on additive manufacturing of ceramic-based materials was recently published by Travitzky et al. [24]. However, these processes are either incapable of producing a mechanically strong part, or embedding a sensor in the part during fabrication is infeasible. Thus, development of a process for manufacturing high-strength advanced ceramics with embedded sensors could be very beneficial to this field.

Due to their small size, light weight, immunity to electromagnetic interference, multiplexing and distributed sensing capability, resistance to chemical corrosion, and remote operation capability, optical fiber sensors are by far the best candidates to be embedded in parts. FBG is the most successful fiber optic sensor and has shown great advantages for integrating with AM techniques. FBGs consist of periodic refractive index variations written by an intense ultraviolet (UV) laser. These periodic variations, also

called Bragg grating, have a certain period that can be encoded by an optical resonant wavelength, and by tracking the resonant wavelength shift, one can detect the strain applied on the FBG, making it a good candidate for strain measurement. However, it has been found that the UV laser induced material variations could be easily erased if the ambient temperature is higher than 450 °C, making it inapplicable for strain sensing under high temperature (up to 1000 °C) [25]. In some particular applications, such as high temperature material characterization, coal gasifier health monitoring, turbine crack detection, or structural health monitoring of the leading edge of a wing, strain sensors that can survive in extreme temperatures are needed. Most of the optical fiber sensors are made of silica glass and their long-term reliability above 1000 °C has been a concern due to the degradation of optical properties and mechanical strength. To further increase the operating temperatures, researchers have turned to sapphire fibers which have a melting point of 2050 °C, low optical loss in a large spectrum window, superior mechanical strength, and excellent resistance to chemical corrosion [26]. Very recently, constructing a sensor on an optical sapphire fiber for use in temperatures up to 1400 °C has been successfully demonstrated by Huang et al. [27]. As a result, technologies for the embedment of sapphire fiber sensors for high temperature applications are highly needed.

In this paper, a freeform extrusion fabrication process for the fabrication of solid ceramic components, called Ceramic On-Demand Extrusion (CODE), is employed to embed sapphire optical fiber sensors in alumina parts for high-temperature sensing. Micrographs of embedded fibers are examined, optical attenuation is measured, and the effect of embedded fiber on parts density, shrinkage, strength, and hardness is examined.

2. METHODOLOGY

2.1. MATERIALS AND PASTE PREPARATION

Unjacketed sapphire fibers of 5 cm length and 125/250 μm diameter (SF125-5 and SF250-5, MicroMaterials Inc., Tampa, FL, USA) produced by a laser heated pedestal growth system were purchased to be embedded into the parts. Both ends of all the fibers were polished by the manufacturer to minimize transmission losses. The fiber properties are listed in Table 1.

Table 1. Fiber characteristics.

Name	Fiber orientation	Tensile strength	Attenuation[*]
SF125-5, SF250-5	C-axis	2.2 GPa	0.5-1.0 dB

[*] In near-infrared (for a fiber of 1 m length and 300 μm dia.)

The paste is composed of a commercially available alumina powder (A-16SG, Almatis Inc., Leetsdale, PA, USA), deionized water, ammonium polymethacrylate (DARVAN® C-N, Vanderbilt Minerals, Norwalk, CT, USA), and cold-water-dispersible methylcellulose (Methocel J5M S, Dow Chemical Company, Midland, MI, USA). The powder properties are listed in Table 2.

Table 2. Powder characteristics.

Name	Particle size	Surface area	Purity	Max. fired density
A-16SG	0.34 μm	9.44 m^2/g	99.8%	3.95 g/cm^3

The alumina powder was dispersed in water using 1 mg Darvan C per square meter of surface area of power and then ball-milled for about 15 hours to break up agglomerates and to produce a uniform mixture. Methylcellulose was dissolved in water (<1 vol%) and was used as a binder to increase paste viscosity and to assist in forming a stronger green body after drying. A vacuum mixer (Model F, Whip Mix, Louisville, KY, USA) was employed to mix the paste homogeneously without introducing air for 12 minutes. Finally, a vibratory table (Syntron Material Handling, Saltillo, MS, USA) was used to remove the remaining air bubbles.

2.2. PROCESSING

The Ceramic On-Demand Extrusion process [28] was used to fabricate the parts. In this AM process, ceramic paste is extruded at controlled flowrates through a circular nozzle. The nozzle is attached to a motion system, which is capable of moving in X, Y and Z directions through G & M code commands provided by an indigenously developed tool-path planning software. The extrudate is deposited on a substrate located in a tank designed to hold a fluid medium. Once the deposition of each layer is completed, a liquid

feeding subsystem pumps a mineral oil into the tank surrounding the layer to preclude undesirable evaporation from the sides of the deposited layers.

The oil level is monitored and controlled by LabVIEW (National Instruments Corp., Austin, TX, USA) using a closed loop system so that it reaches just below the top surface of the part being fabricated. The subsystem begins with an input from the G & M code signaling a desired oil level. The desired oil level is compared to the actual level, given by a level sensor, to produce an error. This error is sent to a PID controller to send a command voltage to a micro gear pump to control the oil flow rate. For parts with internal structures, a sparse sacrificial layer with a serpentine pattern is printed before building the part. This layer allows flow of oil into the internal structures.

Infrared radiation is then used to uniformly dry the deposited layer so that the part being fabricated can maintain its shape when the next layers are being deposited on top of it. The part is fabricated in a layer-by-layer fashion by repeating the layered deposition followed by layered radiation drying with a liquid surrounding the already deposited layers. If a sensor is to be embedded, the fabrication process is halted after a certain number of layers have been deposited. The sensors are placed in their predetermined locations, and the remaining layers are deposited. Once the fabrication process is completed, the remaining water in the fabricated part is removed further by bulk drying to obtain green parts. The post-processing includes removing the binder content at elevated temperatures and sintering the part.

Six alumina blocks were fabricated and five sapphire fibers of the same diameter were embedded in each block. The as-printed size of the blocks was $32 \times 28 \times 4.4$ mm^3 (length, width, and height, respectively). A fixture was employed to place the fibers accurately in their predetermined locations in the longitudinal direction of the blocks as shown in Figure 1. Three of the blocks had fibers of 125 μm diameter embedded in them while the other three contained 250 μm fibers. A nozzle (Gauge 20 Precision Needle, Integrated Dispensing Solutions Inc., Agoura Hills, CA, USA) with a length of 6.3 mm and an internal diameter of 0.61 mm was used to deposit the paste. Nozzle travel speed, layer thickness, and line spacing were 30 mm/s, 0.4 mm, and 0.6 mm, respectively.
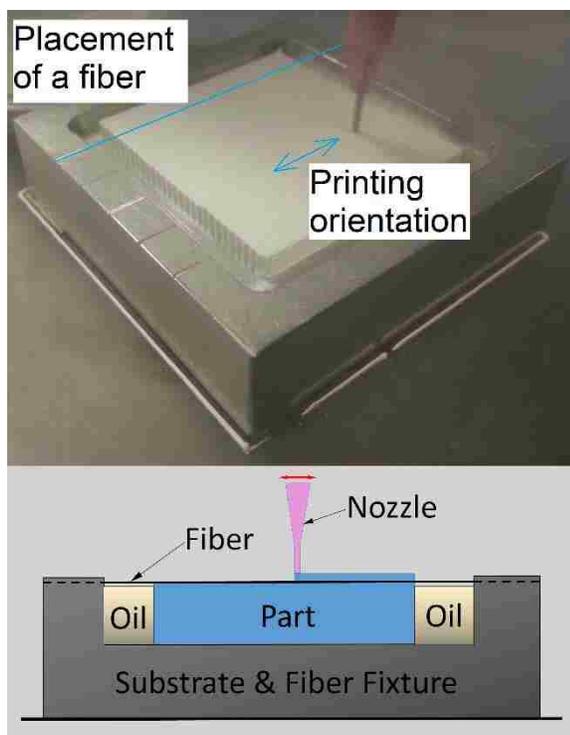
Figure 1. An alumina block with embedded sensors during the fabrication process.

2.3. POST PROCESSING

Two different methods were used to remove the remaining water in the parts. In the first approach, water in the parts was first frozen and then removed through sublimation by using a freeze dryer (Genesis 25L, VirTis, Stone Ridge, NY, USA). The temperature was set at -10 °C and pressure at 2.0 Pa (15 mTorr) for three days. This drying method was used for one block with 125 μm fibers and one block with 250 μm fibers. Humid drying was used as an alternative approach for the other parts. An environmental chamber (LH-1.5, Associated Environmental Systems, Ayer, MA, USA) was used to set the temperature and humidity during the drying process at 75% relative humidity and 25 °C for the first 4-6 hours of drying. This condition guarantees successful drying (i.e. no cracks or warpage). After the first stage of drying, the shrinkage ends and higher drying rates could be achieved, without introducing flaws, by increasing the temperature. This drying method was used for the remaining four blocks.

A heating rate of 1 °C/min was chosen for the binder burnout process to avoid large weight reduction rates. The parts were maintained at 450 °C for two hours. The samples were then sintered with a heating rate of 5 °C/min in an electric furnace (Deltech

Inc., Denver, CO, USA). They were sintered at 1550 °C for 1.5 h and cooled down to room temperature at 10 °C/min rate.

2.4. MEASURING ATTENUATION

Attenuation of the fibers before and after embedment was measured using a tunable Fabry-Perot InGaAsP laser source (8168F, Hewlett-Packard, Palo Alto, CA, USA) and a lightwave multimeter (8163A, Santa Clara, CA, USA). The laser source specifications are listed in Table 3. Multimode silica fibers with a diameter of 62.5 μm were connected to the source and the multimeter, and the sapphire fibers were placed between those fibers as shown in Figure 2 and Figure 3. Micrometer-driven three-axis stages were employed to align the sapphire fibers and silica fibers. An index matching liquid was also used at the junction of sapphire fibers and lead-in/lead-out fibers to reduce the losses. The attenuation spectrum was obtained at an input power of 0 dBm in 1500-1590 nm range with 1 nm steps. A picture of a signal in the visible spectrum (from another laser source) passing through an embedded fiber is shown in Figure 4 for demonstrative purpose.

Table 3. Tunable laser source specifications.

Maximum power	Beam diameter	Numerical aperture	Wavelength
10 dBm	9 μm	0.1	1450-1590 nm

2.5. MECHANICAL TESTS

The size of the blocks before and after sintering was measured to calculate the amount of shrinkage during the sintering processes. Archimedes' test was performed to measure the density of the printed parts after sintering. After the dry mass was recorded, samples were saturated by submersion in distilled water under vacuum for ~12 h. The saturated and suspended masses were then measured to calculate the final density.

Four-point flexural tests were performed at room temperature according to ASTM C1161 [29] to examine the effect of embedded sensors on the strength of the parts. A fully automated surface grinder (FSG-3A818, Chevalier, Santa Fe Springs, CA, USA) was used to machine the parts to standard "A" bars ($1.5 \times 2 \times 25$ mm^3). The bars were

machined with a 600-grit diamond abrasive wheel. Each bar was ground to have a fiber close (typically, tens of micrometers) to its tensile surface so that the effect of fibers on strength would be more prominent. Flexural strengths were measured using a semi-articulating A-bar fixture with an outer span of 20 mm and an inner span of 10 mm in a screw-driven instrumented load frame (5881, Instron, Norwood, MA, USA). The crosshead speed was 0.2 mm/min.

Vickers indentation test was carried out near the embedded fibers according to ASTM C1327 [30] using a microhardness tester (Duramin 5, Struers, Cleveland, OH, USA) to examine the local effect of fibers on the hardness. Samples were polished to a 0.25 μm diamond finish. The indenter was pressed against the parts with a force of 4.91 or 9.81 N for 10 s. The indentation size was measured using an optical microscope with a 40X lens.

Micrographs of cross-sections of fibers and parts as well as fracture surface of broken samples were obtained using optical (KH-3000, Hirox, Hackensack, NJ, USA) and scanning electron (Helios Nanolab 600, FEI, Hillsboro, OR, USA) microscopy.
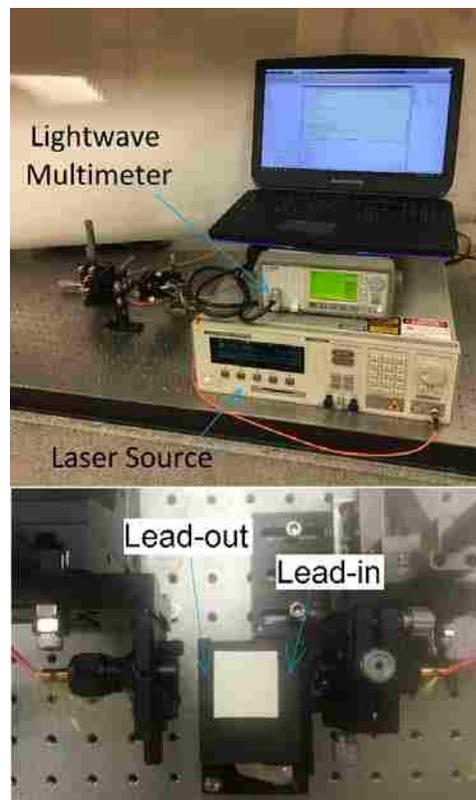
Figure 2. The experimental setup for measuring optical attenuation.
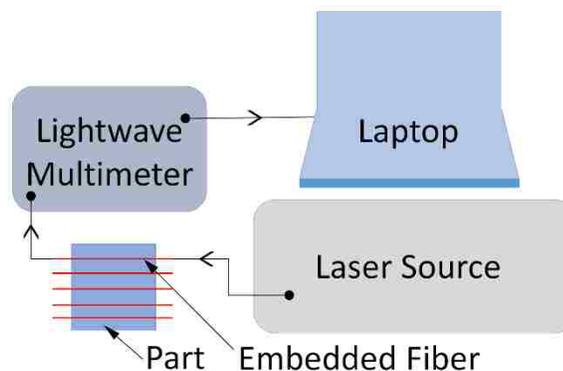
Figure 3. A schematic of the experimental setup for measuring optical attenuation.
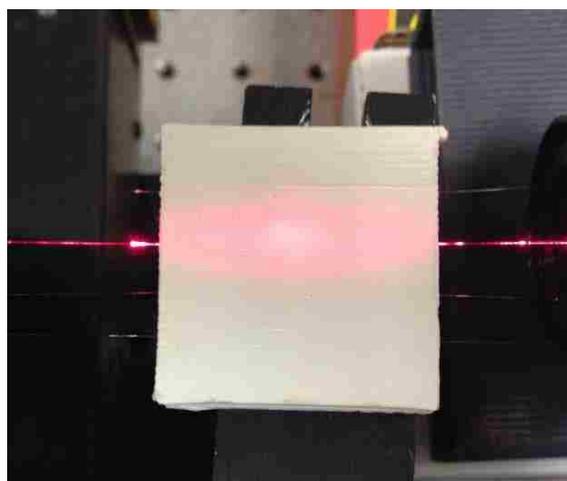
Figure 4. A signal in the visible spectrum passing through an embedded fiber (for demonstrative purpose).

3. RESULTS AND DISCUSSION

A total number of six blocks with embedded fibers were fabricated, out of which two were freeze dried (one with five fibers of 125 μm and the other with five fibers of 250 μm) and four were humid dried (two with five 125 μm fibers and two with five 250 μm fibers). After sintering, parts with 125 μm fibers did not have any observable flaws but were slightly warped as shown in Figure 5 (a) and Figure 6 (a). However, the freeze dried part with 250 μm fibers was considerably warped and some cracks around the fibers were visible (Figure 5 (b)). Both humid dried parts with 250 μm fibers were nearly broken in half (one of them is shown in Figure 6 (b)).
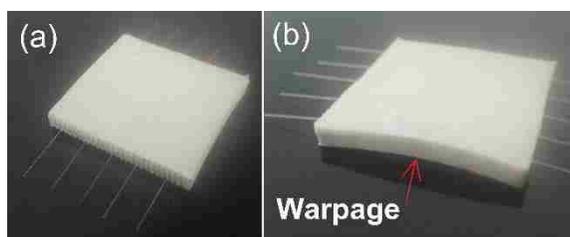
Figure 5. Freeze dried parts with 125 μm fibers (a) and 250 μm fibers (b).
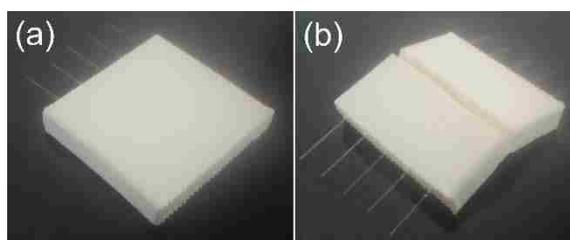
Figure 6. Humid dried parts with 125 μm fibers (a) and 250 μm fibers (b).

The amount of shrinkage and relative densities of the samples after sintering are given in Table 4. More shrinkage was observed in the vertical direction (height) than in the horizontal directions. However, there was no meaningful difference between the amount of shrinkage in length and width. The densities of freeze dried samples were considerably lower than those of the humid dried samples. This is partly due to voids caused by ice crystal formation during freezing of samples as discussed in [31]. In addition to that, expansion of water during freezing (~9 vol%) results in lower green body density. Furthermore, unlike humid drying where ceramic particles are dispersed in a liquid medium and can easily move during drying (causing shrinkage), in freeze drying, particles are not free to move during the drying process. Accordingly, the relative green density of freeze dried parts are considerably lower than the humid dried parts (61% vs. 52%) and a higher sintering temperature/time is required to densify the freeze dried samples.

The failure of humid dried parts could also be explained considering their density. Since they were denser than freeze dried parts they had a higher Young's modulus, thus the same amount of strain caused by shrinkage of the part and its slippage on the fibers during sintering resulted in higher stresses in them. In the case of 250 μm fibers, the contact area between part and fiber was twice as much as that for 125 μm fibers and the force became big enough to cause fracture (in humid dried parts) or warpage/cracks (in freeze dried parts). Fortunately, for smaller fibers (whether humid dried or freeze dried)

the stresses were not large enough to warp/fracture the part or the fiber. However, further evidence is required to confirm this hypothesis.

Table 4. Amount of shrinkage and relative densities of parts with embedded sapphire fibers.

	125 µm, freeze dried	125 µm, humid dried	250 µm, freeze dried	250 µm, humid dried
Shrinkage in length	14%	15%	14%	14%
Shrinkage in width	15%	17%	14%	16%
Shrinkage in height	17%	18%	16%	18%
Volumetric shrinkage	39%	42%	38%	41%
Relative density	93%	98%	92%	98%

Several micrographs of embedded fibers are shown in Figures 7-10. Figure 7 shows a typical micrograph of embedded 125 μm fibers. There is a good bonding between fiber and part and no severe damage to part/fiber is observed. However, for humid dried parts, a slight damage to the surface of fibers is revealed at higher magnifications as seen in Figure 8.

As mentioned earlier, cracks formed in freeze dried parts near some of the 250 μm fibers as could be seen in Figure 9. However, the micrographs of fractured parts (i.e. humid dried with 250 μm fibers) were free of flaws even at high magnifications (Figure 10).
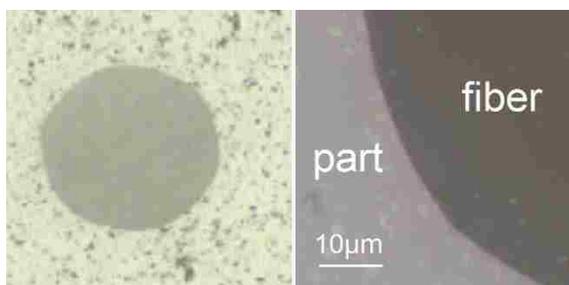
Figure 7. Typical micrographs of embedded 125 μm fibers.
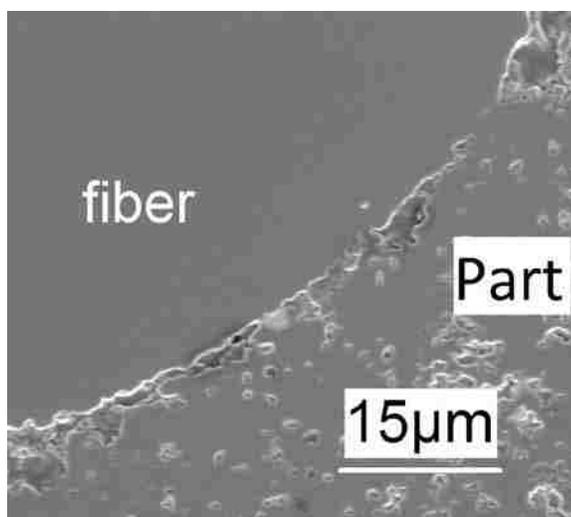
Figure 8. Slight damage to the surface of 125 μm fibers when humid dried parts are sintered.
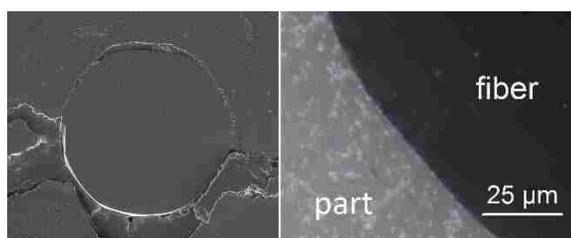
Figure 9. Typical micrographs of freeze dried parts with embedded 250 μm fibers.
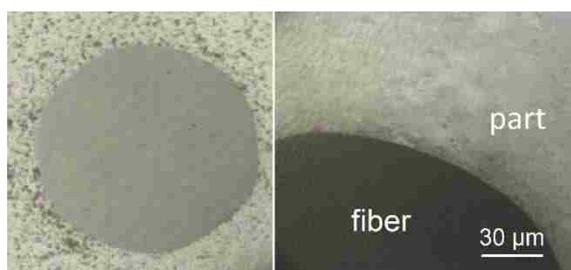
Figure 10. Typical micrographs of humid dried parts with embedded 250 μm fibers.

3.1. ATTENUATION

The typical attenuation spectra of optical signals passing through as-received (not embedded) sapphire fibers of 125 and 250 μm diameter in the range of 1500-1590 nm for a 0 dBm input are plotted in Figure 11. The amount of attenuation is clearly much larger than specified by the manufacturer (Table 1) mainly due to large mismatch between the diameter of sapphire fibers and silica input/output fibers, the gap between fibers, and the numerical aperture of the lead-in fiber. These effects are schematically shown in Figure

12. There are also other reasons with a smaller contribution; the fibers have an approximately rounded hexagonal cross-section, their surface and ends (although polished) are not perfectly smooth, and the sapphire crystal is uniaxial. The attenuation of the signal is considerably higher for 250 μm fiber due to larger mismatch in diameter.
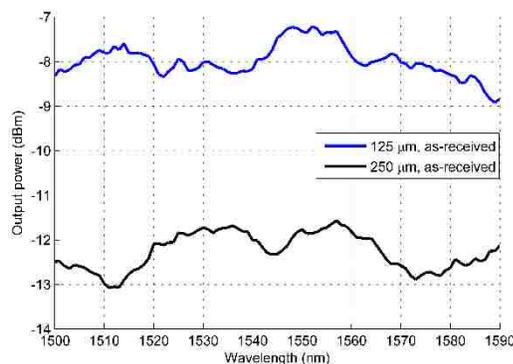
Figure 11. Output power from as-received fibers at different wavelengths for an input power of 0 dBm.

Figure 12. A schematic of losses in transmitted power as a result of input numerical aperture and diameter mismatch.

These losses could be greatly reduced, however. Since the objective was to compare the attenuation before and after embedment, no action was taken to reduce these losses. It should also be noted that the dependency of attenuation on signal wavelength, i.e. fluctuations in Figure 11, was random and not repeatable (even if the same fiber was tested after being slightly repositioned). This is due to a well-known optical fiber concept referred to as multimodal interferences based on a singlemode-multimode-singlemode (SMS) fiber structure [32]. SMS spectrum is very sensitive to position. Even 50 nm position change alters the spectrum considerably. Although multimode fibers are used as lean in/out fibers, they have a limited number of optical modes which can be considered as nearly singlemode in comparison with highly multimode sapphire fibers.

The relative transmission of embedded fibers compared to as-received fibers are plotted in Figure 13. The average values are also reported in Table 5. As expected, 125

µm fibers embedded in freeze dried parts had the lowest loss (transmitting an average of 79% of power compared to as-received fibers) and 250 µm fibers embedded in humid dried parts had the highest loss (passing only 0.0008% of power relative to as-received 250 µm fibers due to severe bending).
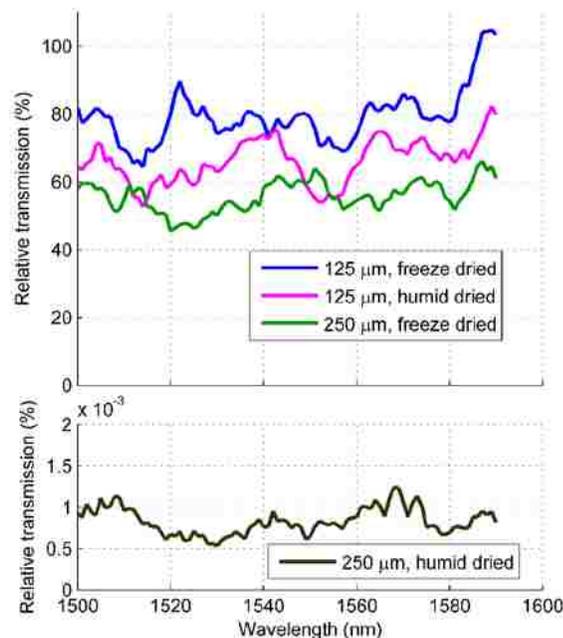
Figure 13. Transmission of fibers after embedment and post-processing, relative to as-received fibers.

Table 5. Average transmission of fibers, relative to as-received fibers.

	125 µm, freeze dried	125 µm, humid dried	250 µm, freeze dried	250 µm, humid dried
Average relative transmission	79%	66%	56%	0.0008%

The most important factor for these losses is believed to be warpage of parts causing losses inside the fibers as well as at the input/output. Another reason is damage to the surface of fibers during the sintering process as shown in Figure 8. This damage is more severe for humid dried parts experiencing more shrinkage than freeze dried parts. Furthermore, residual stresses might also contribute to losses. This has been verified for silica optical fibers (e.g. in [33]) and could also be true for sapphire fibers. Nevertheless, the amount of losses is acceptable for the first three cases and they could potentially be

used as sensors to measure the strains in the parts resulted from thermal or mechanical loads.

In the future, the feasibility of successful embedment of large fibers will be studied by "constrained" sintering of parts. A mechanical load will be applied during sintering to preclude shrinkage in the longitudinal direction and reduce slippage of the part on the fibers. This could also reduce the losses for smaller fibers by preventing bending during sintering. Another potential solution to reduce losses is coating the fibers with protective layers before embedding them.

3.2. MECHANICAL PROPERTIES

The average flexural strengths of test bars were 208, 391, and 152 MPa for freeze dried bars with 125 μm fibers, humid dried bars with 125 μm fibers, and freeze dried bars with 250 μm fibers, respectively (as mentioned before, humid dried parts with 250 μm fibers fractured during sintering). There were 10 samples for measuring flexural strength of humid dried parts with 125 μm fibers and 5 samples for measuring flexural strength of freeze dried parts with 125 μm fibers. The actual strength of freeze dried bars with 250 μm fibers was probably lower than the measured value since three of the bars fractured during grinding, which indicates a very low strength. Furthermore, the data for this group is not reliable because it is based on only two samples. Table 6 lists the flexural strengths of bars with embedded fibers as well as bars without fibers fabricated using the same procedure in another study by Ghazanfari et al. [34]. The average hardness values near the fibers were 14.9, 17.1, and 13.8 GPa for freeze dried bars with 125 μm fibers, humid dried bars with 125 μm fibers, and freeze dried bars with 250 μm fibers, respectively. These values are also listed in Table 6 along with obtained values for parts without fibers from the same study by Ghazanfari et al. [34]. Figure 14 shows an example of indented surface for hardness measurements near a fiber.

Table 6. Flexural strength and hardness of samples.

	125 μm, freeze dried	125 μm, humid dried	250 μm, freeze dried	No fiber, freeze dried	No fiber, humid dried
Strength (MPa)	208±37	391±42	152±54	330±57	404±41
Hardness (GPa)	14.9±0.4	17.1±0.2	13.8±0.8	14.5±0.4	18.7±0.3
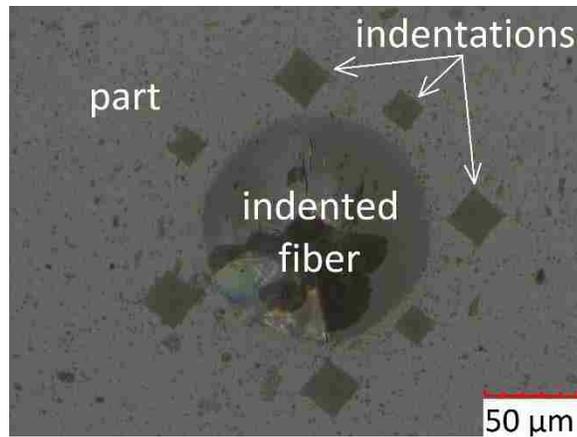
Figure 14. Indentations near a 125 μm fiber used to measure hardness.

The inferior properties of freeze dried bars with 250 μm fibers were expected due to presence of cracks and residual stresses. For humid dried bars with 125 μm fibers, properties are only slightly lower than parts with no fibers which is another evidence of aptness of the proposed method of fabricating smart parts. However, the considerable decrease in flexural strength of freeze dried bars with 125 μm fibers was unforeseen and further study is needed to confirm and explain this degradation.

Figure 15 provides typical 2D and 3D views of fracture surfaces near the fibers. Except freeze dried bars with 250 μm fibers, no fracture origins could be observed near the fibers.
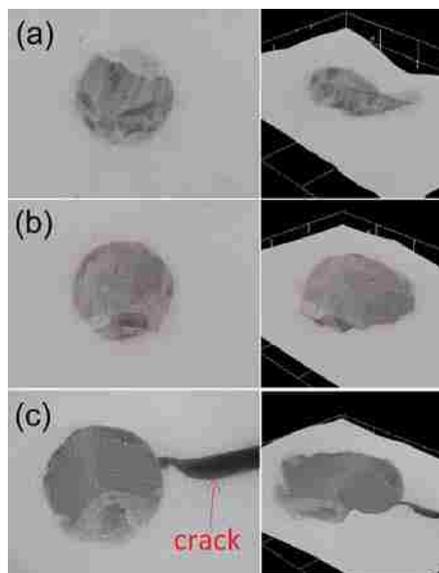
Figure 15. Fracture surface of a freeze dried bar with 125 μm fibers (a), a humid dried bar with 125 μm fibers (b), and a freeze dried bar with 250 μm fibers (c).

4. CONCLUSIONS

An additive manufacturing process using ceramic on-demand extrusion has been employed to study embedding sapphire optical fiber sensors in alumina components during the fabrication process. Two groups of fibers were used: 15 fibers of 125 μm diameter and 15 fibers of 250 μm diameter. Two different methods were investigated for drying parts after fabrication, and they resulted in two different final relative densities (~92% and ~98%). The results of microscopy, attenuation tests, and mechanical tests indicate that as the diameter of the fibers and relative density of the parts increase, it becomes more challenging to successfully embed the fibers. Nevertheless, for smaller fibers (125 μm diameter) the parts and the embedded fibers are functional. Thus, they could potentially be used to measure the strains in the parts generated by thermal and/or mechanical loads.

ACKNOWLEDGEMENTS

REFERENCES

[1]   A. Raghavan, C.E.S. Cesnik, Review of guided-wave structural health monitoring, Shock Vib. Dig. 39 (2007) 91–114. doi:10.1177/0583102406075428.

[2]   M. Majumder, T.K. Gangopadhyay, A.K. Chakraborty, K. Dasgupta, D.K. Bhattacharya, Fibre Bragg gratings in structural health monitoring-Present status and applications, Sensors Actuators, A Phys. 147 (2008) 150–164. doi:10.1016/j.sna.2008.04.008.

[3]   M.R. Werner, W.R. Fahrner, Review on materials, microsensors, systems, and devices for high-temperature and harsh-environment applications, IEEE Trans. Ind. Electron. 48 (2001) 249–257.

[4]   W.L. Schulz, J.P. Conte, E. Udd, Long gage fibre optic Bragg grating strain sensors to monitor civil structures, in: Proc. SPIE 4330, Smart Struct. Mater. 2001 Smart Syst. Bridg. Struct. Highw., Newport Beach, CA, USA, 2001: p. 56. doi:10.1117/12.434156.

[5]   Z. Zhou, T.W. Graver, L. Hsu, J.P. Ou, Techniques of advanced FBG sensors: fabrication, demodulation, encapsulation and their applications in the structural health monitoring of bridges, Pac. Sci. Rev. 5 (2003) 116–121.

[6]   B.K.A. Ngoi, J. Paul, L.P. Zhao, Z.P. Fang, Enhanced lateral pressure tuning of fiber Bragg gratings by polymer packaging, Opt. Commun. 242 (2004) 425– 430.

[7]   J.S. Leng, G.C. Mays, G.F. Fernando, Structural NDE of concrete structures using protected EFPI and FBG sensors, Sens. Actuators A. 126 (2006) 340–347.

[8]   T.A. Dawood, R.A. Shenoi, M. Sahin, A procedure to embed fibre Bragg grating strain sensors into GFRP sandwich structures, Compos. A. 38 (2007) 217–226.

[9]   S. Lu, H. Xia, Strengthen and real-time monitoring of RC beam using "intelligent" CFRP with embedded FBG sensors, J. Constr. Build. Mater. 21 (2007) 1839–1845.

[10]   W. Chung, D. Kang, Full-scale test of a concrete box girder using FBG sensing system, Eng. Struct. 30 (2008) 643–652.

[11]   K. Kesavan, K. Ravisankar, S. Parivallal, P. Sreeshylam, S. Sridhar, Experimental studies on fiber optic sensors embedded in concrete, Meas. J. Int. Meas. Confed. 43 (2010) 157–163. doi:10.1016/j.measurement.2009.08.010.

[12]   M. Raymond, Structural monitoring with fiber optic technology, Academic Press, California, 2001.

[13]   G. Pereira, C. Frias, H. Faria, O. Frazao, A.T. Marques, Study of strain-transfer of FBG sensors embedded in unidirectional composites, Polym. Test. 32 (2013) 1006–1010. doi:10.1016/j.polymertesting.2013.05.006.

[14]   J. Chilles, A. Croxford, I.P. Bond, Design, application, and validation of embedded ultrasonic sensors within composite materials, in: P.J. Shull (Ed.), Proc. SPIE 9437, Struct. Heal. Monit. Insp. Adv. Mater. Aerospace, Civ. Infrastruct., Sad Diego, CA, USA, 2015. doi:10.1117/12.2083944.

[15]   J.S. Chilles, A. Croxford, I.P. Bond, Design of an embedded sensor, for improved structural performance, Smart Mater. Struct. 24 (2015). doi:http://dx.doi.org/10.1088/0964-1726/24/11/115014.

[16]   X. Li, X. Zhang, D. Werschmoeller, H. Choi, X. Cheng, Embedded micro/nano sensors for harsh engineering environments, in: Proc. IEEE Sensors Conf., 2008: pp. 1273–1276. doi:10.1109/ICSENS.2008.4716676.

[17]   G.D. Janaki Ram, C. Robinson, Y. Yang, B.E. Stucker, Use of ultrasonic consolidation for fabrication of multi-material structures, Rapid Prototyp. J. 13 (2007) 226–235. doi:10.1108/13552540710776179.

[18] Y. Li, W. Liu, Y. Feng, H. Zhang, Ultrasonic embedding of nickel-coated fiber Bragg grating in aluminum and associated sensing characteristics, Opt. Fiber Technol. 18 (2012) 7–13. doi:10.1016/j.yofte.2011.09.004.

[19] R.R.J. Maier, W.N. Macpherson, J.S. Barton, M. Carne, M. Swan, J.N. Sharma, S.K. Futter, D.A. Knox, B.J.S. Jones, S. McCulloch, Embedded fiber optic sensors within additive layer manufactured components, IEEE Sens. J. 13 (2013) 969–979.

[20] M.J. Dapino, Smart structure integration through ultrasonic additive manufacturing, in: ASME 2014 Conf. Smart Mater. Adapt. Struct. Intell. Syst., Newport, Rhode Island, USA, 2014: pp. 1–8.

[21] T. Monaghan, A.J. Capel, S.D. Christie, R.A. Harris, R.J. Friel, Solid-state additive manufacturing for metallized optical fiber integration, Compos. Part A Appl. Sci. Manuf. 76 (2015) 181–193. doi:10.1016/j.compositesa.2015.05.032.

[22] J. Li, T. Monaghan, S. Masurtschak, A. Bournias-Varotsis, R.J. Friel, R.A. Harris, Exploring the mechanical strength of additively manufactured metal structures with embedded electrical materials, Mater. Sci. Eng. A. 639 (2015) 474–481. doi:10.1016/j.msea.2015.05.019.

[23] C. Kousiatza, D. Karalekas, In-situ monitoring of strain and temperature distributions during fused deposition modeling process, Mater. Des. 97 (2016) 400–406. doi:10.1016/j.matdes.2016.02.099.

[24] N. Travitzky, A. Bonet, B. Dermeik, T. Fey, I. Filbert-Demut, L. Schlier, T. Schlordt, P. Greil, Additive manufacturing of ceramic-based materials, Adv. Eng. Mater. 16 (2014) 729–754. doi:10.1002/adem.201400097.

[25] K.O. Hill, G. Meltz, Fiber Bragg grating technology fundamentals and overview, J. Light. Technol. 15 (1997) 1263–1276. doi:10.1109/50.618320.

[26] G.N. Merberg, J.A. Harrington, Optical properties of single-crystal sapphire fibers, Appl. Opt. 32 (1993) 3201–3209. doi:10.1364/AO.36.005934.

[27] J. Huang, X. Lan, Y. Song, Y. Li, L. Hua, H. Xiao, Microwave interrogated sapphire fiber michelson interferometer for high temperature sensing, IEEE Photonics Technol. Lett. 27 (2015) 1398–1401. doi:10.1109/LPT.2015.2422136.

[28] A. Ghazanfari, W. Li, M.C. Leu, G.E. Hilmas, A novel extrusion-based additive manufacturing process for ceramic parts, in: D. Bourell, J. Beaman, R. Crawford, S. Fish, H. Marcus, C. Seepersad (Eds.), Solid Free. Fabr. Symp., Austin, TX, USA, 2016.

[29] ASTM C1161, Standard test method for flexural strength of advanced ceramics at ambient temperatures, West Conshohocken, PA, USA, 2013. doi:10.1520/C1161-13.

[30] ASTM C1327, Standard test method for Vickers indentation hardness of advanced ceramics, West Conshohocken, PA, USA, 2015. doi:10.1520/C1327-15.

[31] J. Li, M.C. Leu, G.E. Hilmas, Effects of temperature on aqueous freeform extrusion fabrication, in: D. Bourell, J. Beaman, R. Crawford, S. Fish, H. Marcus, C. Seepersad (Eds.), Solid Free. Fabr. Symp., Austin, TX, USA, 2015: pp. 319–331.

[32] Q.W.Q. Wang, G. Farrell, W.Y.W. Yan, Investigation on single-mode-multimode-single-mode fiber structure, J. Light. Technol. 26 (2008) 512–519. doi:10.1109/JLT.2007.915205.

[33] Y. Namihira, M. Kudo, Y. Mushiake, Effect of mechanical stress on the transmission characteristics of optical fiber, Electron. Commun. Japan. 60 (1977) 107–115.

[34] A. Ghazanfari, W. Li, J. Watts, M.C. Leu, Effect of process parameters on properties of parts produced by ceramic on-demand extrusion process, Under Prep. (n.d.).

SECTION

2. CONCLUSIONS

A freeform extrusion fabrication process for producing solid ceramic parts, called Ceramic On-Demand Extrusion (CODE), was introduced and investigated in this dissertation. The developed tool-path planning software, paste preparation steps, subsystems of the fabrication system, and post-processing were explained. To examine the capabilities of the process, several parts for various applications were built. The CODE process has been shown to be able to produce large complex parts (up to several centimeters of wall-thickness) with near theoretical density (>98%) and a uniform microstructure. The mechanical properties of parts were extensively studied. These properties surpass those produced by most other additive manufacturing processes and match those produced by conventional fabrication techniques. Other advantages include facile preparation of feedstock, low amount of binder content expediting the post-processing, feasibility of embedding sensors, and the capability of grinding products in the green state. This indicates the high potential of the CODE process to be employed in industrial applications, especially where one-of-a-kind parts or a small number of customizable products with good mechanical properties are needed.

An algorithm was developed to estimate the "horizontal" staircase effect and a technique was proposed to reduce this type of geometrical error and/or to increase the productivity for freeform extrusion fabrication processes. It was shown that the adaptive rastering technique proposed in this dissertation can considerably improve the dimensional accuracy and/or fabrication time for freeform extrusion fabrication methods.

A derivative-free optimization method was utilized to determine the optimum orientation of rasters for each layer of a part to minimize the fabrication error. It was demonstrated that the proposed approach is effective in reducing the horizontal staircase errors without altering any other performance factors such as the vertical errors, fabrication time, amount of support material, and number of layers

To exploit the capabilities of additive manufacturing technologies in producing functionally graded materials with complex material distribution, a methodology was

developed in this study to optimize the distribution of material composition for functionally graded parts. The advantages of the proposed methodology include:

- Providing flexibility in incorporating any material model for predicting the behavior of functionally graded parts (a realistic model was used in this study, but it could be replaced with any other simple or complex model),

- Capability of handling complex material distributions and three-dimensional geometries,

- Analysis of multi-physics problems (e.g., dynamic, thermo-mechanical, thermo-fluid, electromagnetic, and thermal-electrical-structural problems),

- Feasibility of considering any objective function for optimization, and

- Capability of handling constraints including manufacturing constraints and desired material at any location.

The additive manufacturing process using ceramic on-demand extrusion was employed to study embedding sapphire optical fiber sensors in alumina components during the fabrication process. The results of microscopy, attenuation tests, and mechanical tests indicated that as the diameter of the fibers and relative density of the parts increase, it becomes more challenging to successfully embed the fibers. Nevertheless, for smaller fibers (125 μm diameter) the parts and the embedded fibers are functional. Thus, they could potentially be used to measure the strains in the parts generated by thermal and/or mechanical loads.

3. RECOMMENDATIONS FOR FUTURE WORK

Although the mechanical properties of parts produced by the Ceramic On-Demand Extrusion (CODE) process made of several materials have been extensively studied, there are many other materials which need to be studied. For example, CODE can be used to make parts from boron carbide, zirconium diboride, zirconium carbide, etc. and examine their properties. In fact, CODE is still in its fledgling stage and many more studies need to be done to fully establish the process.

The theoretical studies presented in Papers IV, V, VI and VII need to be implemented in the CODE system to increase its productivity, reduce the geometrical errors, and produce functionally graded parts with optimal distribution of material composition. For instance, the CODE system may be improved to mix two or three different materials homogeneously and the lining block designed in Paper VII may be fabricated and examined. This capability opens doors for numerous aerospace and medical applications, some of which are mentioned below.

Prosthetic hip joint: Alumina is the most widely used structural ceramic for femoral heads of prosthetic hip joints. Despite its excellent hardness and biocompatibility, alumina is prone to fracture due to its low fracture toughness. To solve this problem, the methodology proposed in Paper VII may be used to design a femoral head with an optimal grading from a tough material (e.g. zirconia) at the core to alumina at the surface. This material composition gradient increases the durability against dynamic loads without sacrificing the wear-resistivity, and can considerably extend the lifespan. Next, these parts may be fabricated and their bio-stability and in vitro performance may be evaluated.

Smart structures: although Paper VIII shows feasibility of producing smart structures using CODE, real sensors have yet to be embedded in parts and their performance in advanced energy systems is to be examined. Most important challenge will be increasing the accuracy of the embedded sensors.

REFERENCES

[1]   J. Grau, J. Moon, S. Uhland, M.J. Cima, E. Sachs, High green density ceramic components fabricated by the slurry-based 3DP process, in: Solid Free. Fabr. Symp., Austin, TX, USA, 1997: pp. 371–378.

[2]   R. Noguera, M. Lejeune, T. Chartier, 3D fine scale ceramic components formed by ink-jet prototyping process, J. Eur. Ceram. Soc. 25 (2005) 2055–2059. doi:10.1016/j.jeurceramsoc.2005.03.223.

[3]   E.A. Griffin, S. McMillin, Selective laser sintering and fused deposition modeling processes for functional ceramic parts, in: Solid Free. Fabr. Symp., Austin, TX, USA, 1995: pp. 25–30.

[4]   M.L. Griffith, J.W. Halloran, Freeform fabrication of ceramics via stereolithography, J. Am. Ceram. Soc. 79 (1996) 2601–2608. doi:10.1111/j.1151-2916.1996.tb09022.x.

[5]   C. Griffin, J. Daufenbach, S. McMillin, Desktop manufacturing: LOM vs pressing, Am. Ceram. Soc. Bull. 73 (1994) 109–113.

[6]   N. Travitzky, A. Bonet, B. Dermeik, T. Fey, I. Filbert-Demut, L. Schlier, T. Schlordt, P. Greil, Additive manufacturing of ceramic-based materials, Adv. Eng. Mater. 16 (2014) 729–754. doi:10.1002/adem.201400097.

[7]   M.A. Jafari, W. Han, F. Mohammadi, A. Safari, S.C. Danforth, N. Langrana, A novel system for fused deposition of advanced multiple ceramics, Rapid Prototyp. J. 6 (2000) 161–175.

[8]   G.E. Hilmas, J.L. Lombardi, R.A. Hoffman, Advances in the fabrication of functionally graded materials using extrusion freeform fabrication, Funct. Graded Mater. (1997) 319–324. doi:10.1016/B978-044482548-3/50053-6.

[9]   M.C. Leu, B.K. Deuser, L. Tang, R.G. Landers, G.E. Hilmas, J.L. Watts, Freeze-form extrusion fabrication of functionally graded materials, CIRP Ann. - Manuf. Technol. 61 (2012) 223–226. doi:10.1016/j.cirp.2012.03.050.

[10]   K. Stuffle, A. Mulligan, P. Calvert, J. Lombardi, Solid freebody forming of ceramics from polymerizable slurry, in: Solid Free. Fabr. Symp., Austin, TX, USA, 1993: pp. 60–63.

[11]   R. Vaidyanathan, J. Walish, J.L. Lombardi, S. Kasichainula, P. Calvert, K.C. Cooper, The extrusion freeforming of functional ceramic prototypes, J. Miner. Met. Mater. Soc. (2000) 34–37. doi:10.1007/s11837-000-0066-4.

[12]   S.C. Danforth, Fused deposition of ceramics: a new technique for the rapid fabrication of ceramic components, Mater. Technol. 10 (1995) 144–146.

[13] M.K. Agarwala, V.R. Jamalabad, N.A. Langrana, A. Safari, P.J. Whalen, S.C. Danforth, Structural quality of parts processed by fused deposition, Rapid Prototyp. J. 2 (1996) 4–19. doi:10.1108/13552549610732034.

[14] G.M. Lous, I.A. Cornejo, T.F. McNulty, A. Safari, S.C. Danforth, Fabrication of piezoelectric ceramic/polymer composite transducers using fused deposition of ceramics, J. Am. Ceram. Soc. 83 (2000) 124–128. doi:10.1111/j.1151-2916.2000.tb01159.x.

[15] A. Bandyopadhyay, P.K. Panda, M.K. Agarwala, S.C. Danforth, A. Safari, Processing of piezocomposites by fused deposition technique, J. Am. Ceram. Soc. 80 (1997) 1366–72. doi:10.1111/j.1151-2916.1997.tb02993.x.

[16] A. Safari, M. Allahverdi, E.K. Akdogan, Solid freeform fabrication of piezoelectric sensors and actuators, J. Mater. Sci. 41 (2006) 177–198. doi:10.1007/s10853-005-6062-x.

[17] S. Iyer, J. McIntosh, A. Bandyopadhyay, N. Langrana, A. Safari, S.C. Danforth, R.B. Clancy, C. Gasdaska, P.J. Whalen, Microstructural characterization and mechanical properties of Si3N4 formed by fused deposition of ceramics, Int. J. Appl. Ceram. Technol. 5 (2008) 127–137. doi:10.1111/j.1744-7402.2008.02193.x.

[18] J. Cesarano III, R. Segalmen, P. Calvert, Robocasting provides moldless fabrication from slurry deposition, Ceram. Ind. 148 (1998) 94–102.

[19] H.B. Denham, J. Cesarano III, B.H. King, P. Calvert, Mechanical behavior of robocast alumina, in: Solid Free. Fabr. Symp., Austin, TX, USA, 1998: pp. 589–596.

[20] S. Michna, W. Wu, J.A. Lewis, Concentrated hydroxyapatite inks for direct-write assembly of 3-D periodic scaffolds, Biomaterials. 26 (2005) 5632–5639. doi:10.1016/j.biomaterials.2005.02.040.

[21] J. Lewis, J. Smay, J. Stuecker, J. Cesarano, Direct ink writing of three-dimensional ceramic structures, J. Am. Ceram. Soc. 89 (2006) 3599–3609. doi:10.1111/j.1551-2916.2006.01382.x.

[22] K. Cai, B. Román-Manso, J.E. Smay, J. Zhou, M.I. Osendi, M. Belmonte, P. Miranzo, Geometrically complex silicon carbide structures fabricated by robocasting, J. Am. Ceram. Soc. 95 (2012) 2660–66. doi:10.1111/j.1551-2916.2012.05276.x.

[23] M. Houmard, Q. Fu, M. Genet, E. Saiz, A.P. Tomsia, On the structural, mechanical, and biodegradation properties of HA/β-TCP robocast scaffolds., J. Biomed. Mater. Res. B. Appl. Biomater. 101 (2013) 1233–42. doi:10.1002/jbm.b.32935.

[24] T. Schlordt, S. Schwanke, F. Keppner, T. Fey, N. Travitzky, P. Greil, Robocasting of alumina hollow filament lattice structures, J. Eur. Ceram. Soc. 33 (2013) 3243–48. doi:10.1016/j.jeurceramsoc.2013.06.001.

[25] T. Huang, M.S. Mason, G.E. Hilmas, M.C. Leu, Freeze-form extrusion fabrication of ceramics, in: Solid Free. Fabr. Symp., Austin, TX, USA, 2005: pp. 73–85.

[26] T. Huang, G.E. Hilmas, W.G. Fahrenholtz, M.C. Leu, Dispersion of zirconium diboride in an aqueous, high-solids paste, Int. J. Appl. Ceram. Technol. 4 (2007) 470–79.

[27] T. Huang, M.N. Rahaman, N.D. Doiphode, M.C. Leu, B.S. Bal, D.E. Day, Freeze extrusion fabrication of 13-93 bioactive glass scaffolds for repair and regeneration of load-bearing bones, Ceram. Trans. 228 (2011) 45–55. doi:10.1007/s10856-011-4236-4.

[28] A. Li, A.S. Thornton, B. Deuser, J.L. Watts, M.C. Leu, G.E. Hilmas, R.G. Landers, Freeze-form extrusion fabrication of functionally graded material composites using zirconium carbide and tungsten, in: Solid Free. Fabr. Symp., Austin, TX, USA, 2012: pp. 467–79.

[29] A.S. Thornton, Freeze-form extrusion fabrication of boron carbide, Missouri University of Science and Technology, 2014.

[30] M.S. Mason, T. Huang, R.G. Landers, M.C. Leu, G.E. Hilmas, Aqueous-based extrusion of high solids loading ceramic pastes: Process modeling and control, J. Mater. Process. Technol. 209 (2009) 2946–2957. doi:10.1016/j.jmatprotec.2008.07.004.

[31] X. Zhao, R.G. Landers, M.C. Leu, Adaptive extrusion force control of freeze-form extrusion fabrication processes, J. Manuf. Sci. Eng. 132 (2010) 1–9. doi:10.1115/1.4003009.

[32] B.K. Deuser, L. Tang, R.G. Landers, M.C. Leu, G.E. Hilmas, Hybrid extrusion force-velocity control using freeze-form extrusion fabrication for functionally graded material parts, J. Manuf. Sci. Eng. 135 (2013). doi:10.1115/1.4024534.

[33] H. Zomorodi, R.G. Landers, Extrusion based additive manufacturing using explicit model predictive control, in: Am. Control Conf., Boston, MA, USA, 2016: pp. 1747–1752.

[34] Gibson I, Rosen DW, Stucker B 2010. Additive Manufacturing Technologies. Springer.

[35] Go J, Hart AJ 2015. Rate Limiting Tradeoffs in Machine Design for Extrusion-based Additive Manufacturing. Austin, Texas. 26th Annual International Solid Freeform Fabrication Symposium.

[36]   Dolenc A, Makela I 1994. Slicing procedures for layered manufacturing techniques. Computer-Aided Design 26: 119–126.

[37]   Pande SS, Kumar S 2008. A generative process planning system for parts produced by rapid prototyping. International Journal of Production Research 46: 6431–6460.

[38]   Zhao ZW, Laperriere L 2000. Adaptive direct slicing of the solid model for rapid prototyping. International Journal of Production Research 38: 69–83.

[39]   Kumar C, Choudhury AR 2005. Volume deviation in direct slicing. Rapid Prototyping Journal 11: 174–184.

[40]   Singhal SK, Prashant KJ, Pulak MP 2008. Adaptive slicing for SLS prototyping. Computer-Aided Design and Appli- cations 5: 421–3.

[41]   Hayasi MT, Asiabanpour B 2013. A new adaptive slicing approach for the fully dense freeform fabrication (FDFF) process. Journal of Intelligent Manufacturing 24: 683–694.

[42]   Chen JS, Feng H 2011. Optimal layer setup generation in layered manufacturing with a given error constraint. The Society of Manufacturing Engineers. Journal of Manufacturing Systems 30: 165–174.

[43]   Wang S, Wang Y, Chen C, Zhu X 2013. An adaptive slicing algorithm and data format for functionally graded material objects. International Journal of Advanced Manufacturing Technology 65: 251–258.

[44]   Birman, V. and L.W. Byrd, Modeling and Analysis of Functionally Graded Materials and Structures. Applied Mechanics Reviews, 2007. 60: p. 195-216.

[45]   M.Y. Wang, X. Wang, A level-set based variational method for design and optimization of heterogeneous objects, Comput. Des. 37 (2005) 321–337.

[46]   A.J. Goupee, S.S. Vel, Two-dimensional optimization of material composition of functionally graded materials using meshless analyses and a genetic algorithm, Comput. Methods Appl. Mech. Engrg. 195 (2006) 5926–5948.

[47]   D. Lin, Q. Li, W. Li, S. Zhoua, M. V Swain, Design optimization of functionally graded dental implant for bone remodeling, Compos. Part B. 40 (2009) 668–675.

[48]   K.S. Na, J.H. Kim, Volume fraction optimization of functionally graded composite panels for stress reduction and critical temperature, Finite Elem. Anal. Des. 45 (2009) 845–851.

[49]   A. Xu, Y. Qu, Y. Yang, N.E. Mastorakis, Topological Customization for Materials Composition of 3D Heterogeneous Multi-Functional Components, in: 8th WSEAS Int. Conf. Appl. Comput. Appl. Comput. Sci., 2009.

[50]   R. Chiba, Y. Sugano, Optimisation of material composition of functionally graded materials based on multiscale thermoelastic analysis, Acta Mech. 223, (2012) 891–909.

[51]   X.Y. Kou, G.T. Parks, S.T. Tan, Optimal design of functionally graded materials using a procedural model and particle swarm optimization, Comput. Des. 44 (2012) 300–310.

[52]   A. Ghazanfari, M.C. Leu, Composition optimization for functionally gradient parts considering manufacturing constraints, in: ASME 2014 Int. Manuf. Sci. Eng. Conf., Detroit, Michigan, USA, 2014: pp. 1–6.

[53]   F. Zhang, C. Zhou, S. Das, An efficient design optimization method for functional gradient material objects based on finite element analysis, in: Proc. ASME 2015 Int. Des. Eng. Tech. Conf. Comput. Inf. Eng. Conf. (IDETC/CIE 2015), ASME, Boston, MA, USA, 2015.

[54]   A. Raghavan, C.E.S. Cesnik, Review of guided-wave structural health monitoring, Shock Vib. Dig. 39 (2007) 91–114. doi:10.1177/0583102406075428.

[55]   M. Majumder, T.K. Gangopadhyay, A.K. Chakraborty, K. Dasgupta, D.K. Bhattacharya, Fibre Bragg gratings in structural health monitoring-Present status and applications, Sensors Actuators, A Phys. 147 (2008) 150–164. doi:10.1016/j.sna.2008.04.008.

[56]   M.R. Werner, W.R. Fahrner, Review on materials, microsensors, systems, and devices for high-temperature and harsh-environment applications, IEEE Trans. Ind. Electron. 48 (2001) 249–257.

[57]   W.L. Schulz, J.P. Conte, E. Udd, Long gage fibre optic Bragg grating strain sensors to monitor civil structures, in: Proc. SPIE 4330, Smart Struct. Mater. 2001 Smart Syst. Bridg. Struct. Highw., Newport Beach, CA, USA, 2001: p. 56. doi:10.1117/12.434156.

[58]   Z. Zhou, T.W. Graver, L. Hsu, J.P. Ou, Techniques of advanced FBG sensors: fabrication, demodulation, encapsulation and their applications in the structural health monitoring of bridges, Pac. Sci. Rev. 5 (2003) 116–121.

[59]   B.K.A. Ngoi, J. Paul, L.P. Zhao, Z.P. Fang, Enhanced lateral pressure tuning of fiber Bragg gratings by polymer packaging, Opt. Commun. 242 (2004) 425– 430.

[60]   J.S. Leng, G.C. Mays, G.F. Fernando, Structural NDE of concrete structures using protected EFPI and FBG sensors, Sens. Actuators A. 126 (2006) 340–347.

[61]   T.A. Dawood, R.A. Shenoi, M. Sahin, A procedure to embed fibre Bragg grating strain sensors into GFRP sandwich structures, Compos. A. 38 (2007) 217–226.

[62]   S. Lu, H. Xia, Strengthen and real-time monitoring of RC beam using "intelligent" CFRP with embedded FBG sensors, J. Constr. Build. Mater. 21 (2007) 1839–1845.

[63]   W. Chung, D. Kang, Full-scale test of a concrete box girder using FBG sensing system, Eng. Struct. 30 (2008) 643–652.

[64]   K. Kesavan, K. Ravisankar, S. Parivallal, P. Sreeshylam, S. Sridhar, Experimental studies on fiber optic sensors embedded in concrete, Meas. J. Int. Meas. Confed. 43 (2010) 157–163. doi:10.1016/j.measurement.2009.08.010.

[65]   M. Raymond, Structural monitoring with fiber optic technology, Academic Press, California, 2001.

[66]   G. Pereira, C. Frias, H. Faria, O. Frazao, A.T. Marques, Study of strain-transfer of FBG sensors embedded in unidirectional composites, Polym. Test. 32 (2013) 1006–1010. doi:10.1016/j.polymertesting.2013.05.006.

[67]   J. Chilles, A. Croxford, I.P. Bond, Design, application, and validation of embedded ultrasonic sensors within composite materials, in: P.J. Shull (Ed.), Proc. SPIE 9437, Struct. Heal. Monit. Insp. Adv. Mater. Aerospace, Civ. Infrastruct., Sad Diego, CA, USA, 2015. doi:10.1117/12.2083944.

[68]   J.S. Chilles, A. Croxford, I.P. Bond, Design of an embedded sensor, for improved structural performance, Smart Mater. Struct. 24 (2015). doi:http://dx.doi.org/10.1088/0964-1726/24/11/115014.

[69]   X. Li, X. Zhang, D. Werschmoeller, H. Choi, X. Cheng, Embedded micro/nano sensors for harsh engineering environments, in: Proc. IEEE Sensors Conf., 2008: pp. 1273–1276. doi:10.1109/ICSENS.2008.4716676.

[70]   G.D. Janaki Ram, C. Robinson, Y. Yang, B.E. Stucker, Use of ultrasonic consolidation for fabrication of multi-material structures, Rapid Prototyp. J. 13 (2007) 226–235. doi:10.1108/13552540710776179.

[71]   Y. Li, W. Liu, Y. Feng, H. Zhang, Ultrasonic embedding of nickel-coated fiber Bragg grating in aluminum and associated sensing characteristics, Opt. Fiber Technol. 18 (2012) 7–13. doi:10.1016/j.yofte.2011.09.004.

[72]   R.R.J. Maier, W.N. Macpherson, J.S. Barton, M. Carne, M. Swan, J.N. Sharma, S.K. Futter, D.A. Knox, B.J.S. Jones, S. McCulloch, Embedded fiber optic sensors within additive layer manufactured components, IEEE Sens. J. 13 (2013) 969–979.

[73]   M.J. Dapino, Smart structure integration through ultrasonic additive manufacturing, in: ASME 2014 Conf. Smart Mater. Adapt. Struct. Intell. Syst., Newport, Rhode Island, USA, 2014: pp. 1–8.

[74] T. Monaghan, A.J. Capel, S.D. Christie, R.A. Harris, R.J. Friel, Solid-state additive manufacturing for metallized optical fiber integration, Compos. Part A Appl. Sci. Manuf. 76 (2015) 181–193. doi:10.1016/j.compositesa.2015.05.032.

[75] J. Li, T. Monaghan, S. Masurtschak, A. Bournias-Varotsis, R.J. Friel, R.A. Harris, Exploring the mechanical strength of additively manufactured metal structures with embedded electrical materials, Mater. Sci. Eng. A. 639 (2015) 474–481. doi:10.1016/j.msea.2015.05.019.

[76] C. Kousiatza, D. Karalekas, In-situ monitoring of strain and temperature distributions during fused deposition modeling process, Mater. Des. 97 (2016) 400–406. doi:10.1016/j.matdes.2016.02.099.

[77] N. Travitzky, A. Bonet, B. Dermeik, T. Fey, I. Filbert-Demut, L. Schlier, T. Schlordt, P. Greil, Additive manufacturing of ceramic-based materials, Adv. Eng. Mater. 16 (2014) 729–754. doi:10.1002/adem.201400097.

[78] K.O. Hill, G. Meltz, Fiber Bragg grating technology fundamentals and overview, J. Light. Technol. 15 (1997) 1263–1276. doi:10.1109/50.618320.

[79] G.N. Merberg, J.A. Harrington, Optical properties of single-crystal sapphire fibers, Appl. Opt. 32 (1993) 3201–3209. doi:10.1364/AO.36.005934.

[80] J. Huang, X. Lan, Y. Song, Y. Li, L. Hua, H. Xiao, Microwave interrogated sapphire fiber michelson interferometer for high temperature sensing, IEEE Photonics Technol. Lett. 27 (2015) 1398–1401. doi:10.1109/LPT.2015.2422136.

VITA

Amir Ghazanfari was born on August 14, 1987 in Tehran, Iran. He received his B.S. and M.S. degrees in Mechanical Engineering from Sharif University of Technology in 2009 and 2012, respectively. Amir joined the Innovative Additive Manufacturing (IAM) laboratory (formerly known as Virtual Reality and Additive Manufacturing laboratory) in Fall 2012, and started working on design, development, modeling, and application of Additive Manufacturing processes with a focus on structural ceramics, smart structures and functionally graded materials.

During his Ph.D. studies, Amir Ghazanfari won the Inaugural CEC Dean's Ph.D. Scholar Award (2017), Best Student Paper Award at the ASME Symposium on Integrated Systems Design and Implementation (2016), 2nd Best Paper Award at Intelligent Systems Center Research Symposium (2015), and 2nd Best Poster Award at Tenth Annual Intelligent Systems Center Poster Presentation (2014).

In July 2017, he received his Ph.D. under the direction of Dr. Ming C. Leu in Mechanical Engineering from Missouri University of Science and Technology, Rolla, Missouri, USA.